Experimental and Numerical Evaluation of Diesel-Hydrogen Dual-Fuel Combustion in a HD Single Cylinder Engine

By:

Emadoddin Monemian Esfahani

Submitted in accordance with the requirements

for the degree of Doctor of Philosophy.

University of Nottingham

Faculty of Engineering

June 2018

Abstract

Climate changes emerging in the last few decades have resulted in accelerated efforts to guarantee a viable global ecosystem. Despite the aim of low-carbon economies to integrate all aspects for the minimal GHG outputs, the transport sector is under severe obligation to abide due to the related substantial contribution of CO2 emissions.

Although, in the last few years the electrification of powertrain systems has gained significant attention in the media, it is widely acknowledged by the industry that the internal combustion engine will remain a dominant source of propulsion for decades to come. In recent years, conventional fossil fuels (gasoline and diesel) have been partially replaced with the alternative fuels such as biodiesel, natural gas, ethanol, hydrogen, etc. These substitutions were beneficial in diverse perspectives making significant reductions in exhaust pollutants with maintained performance.

The currently reported work was concerned with experimental and numerical evaluation of the potential to partially replace diesel with hydrogen fuel, which continues to attract attention as a potential longer term alternative fuel solution, whether produced on-board or remotely via sustainable methods. The test engine adopted was of a single cylinder HD diesel with typical common rail diesel fuel injection and EGR of a production HGV's engine.

The experimental work was involved with the fumigation of hydrogen and intake air enrichment with oxygen at two particular engine loads (6 and 12 bar net indicated mean effective pressure - IMEPn-) typically visited under real world HGV driving conditions. Highest practical hydrogen substitution ratios could increase indicated efficiency by up to 4.6% and 2.4% while reducing CO2 emissions by 58% and 32% at 6 and 12 bar IMEPn respectively. Soot and CO emissions were reduced as more hydrogen was supplied, particularly at 6bar IMEP. Furthermore, intake air enrichment with oxygen resulted in a faster combustion process. This could restraint soot and minimised CO emissions at the expense of considerably higher NOx emissions.

The numerical study was made using the commercial engine simulation package, GT-Power. Initially a reverse-run calculation known as Three Pressure Analysis (TPA) was applied for determining the cylinder trapped conditions in addition to the measured burn rate. Two distinct phenomenological models were used in parallel with aim of modelling the dual-fuel combustion. By comparing the optimised calibration factors in different operating points, in-depth evaluation of the unique dual-fuel combustion phenomenon was possible, including evaluation of burning velocities and the knock-on effects on performance under varied mixture compositions. It was concluded that

hydrogen substitution provides a viable method of displacing diesel and the associated carbon emissions with favourable accompanying reductions in soot. The phenomenological “DualFuel” model performed well under ‘conventional’ dual-fuel conditions but was less reliable when a proportion of the diesel was premixed. The arising error was largely associated with lack of dual-fuel burning velocity data, which will remain a key barrier to dual-fuel simulation as the premixing is largely acknowledged to improve the combustion efficiency.

List of contents

Publications related to this research VII

List of figures VIII

List of tables XIII

Acknowledgements XIV

List of acronyms XV

Chapter 1: Introduction 1

1.1 Preface 1

1.2 Research Objectives 1

1.3 Thesis Outline 2

Chapter 2: Literature Review 3

2.1 Overview of IC engine thermodynamics 3

2.2 Alternative gaseous fuels 5

2.2.1 Natural gas and biogas 5

2.2.2 Hydrogen usage in ICEs 7

2.2.3 Hydrogen combustive properties 10

2.3 Engine exhaust emissions 11

2.3.1 Emission regulations and statistics 11

2.3.2 Emission regulations for heavy-duty engines 13

2.4 Diesel combustion fundamentals 15

2.4.1 Dec diesel combustion model 16

2.4.2 Diffusion versus premixed combustion 19

2.4.3 Theoretical analysis of the soot-NOx trade-off 20

2.5 Dual-fuel diesel combustion 22

2.6 Hydrogen enrichment of diesel combustion 25

2.7 Numerical modelling 28

2.7.1 Numerical models classification 28

2.7.2 Wiebe combustion model 30

2.7.3 Phenomenological models 31

2.7.4 A discussion on premixed combustion modelling 35
2.8 Summary 39
Chapter 3: Experimental and Numerical Methodologies 40
3.1 Introduction 40
3.2 HD diesel engine specifications 40
3.3 Diesel fuel injection unit and its injector calibration 42
3.4 Hydrogen and oxygen enrichment setup 45
3.5 Data acquisition system 49
3.5.1 DAQ hardware and exhaust gas analyser 49
3.5.2 Post-processing of acquired data 54
3.6 Numerical methodology 56
3.6.1 Flow computations in GT-Power 56
3.6.2 In-cylinder flow and heat transfer modelling in GT-Power 58
3.6.3 Fuel injection modelling in GT-Power 60
3.6.4 Combustion processing in GT-Power 62
3.6.5 Three Pressure Analysis (TPA) 63
3.6.6 GT "DIPulse" combustion model 67
3.6.7 GT "SITurb" combustion model 70
3.6.8 GT "DualFuel" combustion model 71
3.7 Summary 73
Chapter 4: Experimental Evaluation of hydrogen enrichment of diesel test engine **74**
4.1 Testing conditions for hydrogen enrichment 74
4.2 H2-Diesel combustion analysis 75
4.2.1 H2-Diesel combustion: low load operation (A25) 77
4.2.2 H2-Diesel combustion: medium load operation (A50) 79
4.3 Exhaust emissions and performance of H2-Diesel combustion 81
4.4 Oxygen enrichment of H2-Diesel combustion 83
4.5 Summary 86
Chapter 5: Numerical Study of H2-Diesel Combustion **88**

5.1 Introduction 88
5.2 Optimisation solution 88
5.2.1 Design of Experiments (DOE) 88
5.2.2 Advanced Direct Optimiser (ADO) 91
5.3 DIPulse genetic optimisation results 98
5.4 Dual-fuel modelling results 99
5.4.1 Calibrating the dual-fuel combustion by GT “DI-Wiebe” model 99
5.4.2 DIPulse multipliers characterisation 101
5.4.3 SITurb multipliers characterisation 105
5.4.4 H2-Diesel “dual-fuel” modelling results 113
6.5 Summary 120
Chapter 6: Conclusions and Recommendations 123
6.1 Introduction 123
6.2 Conclusions 123
6.2.1 Experimental tests conclusions 123
6.2.2 Numerical study conclusions 124
6.3 Recommendations 128
Chapter 7: References 130
Appendix A: Technical specifications of measurement devices 138
Appendix B: Supplementary Simulation Results 139

Publications related to this research

1. Monemian, E., Cairns, A., Gilmore, M., et al., Evaluation of intake charge hydrogen enrichment in a heavy-duty diesel engine, published at Procedding of IMechE Part D: Journal of Automobile Engineering, Nov 2017 DOI: 10.1177/0954407017738375
2. Monemian, E., Cairns, A., Pedrozo, V., Hydrogen and Oxygen Fuel Enrichment Effects on a HD Diesel Engine, published at The journal of engine research, Vol. 47, pp. 13-20, Feb 2018, http://www.engineresearch.ir/article-1-608-en.html
3. Monemian, E., Simulating Diesel-Hydrogen Combustion by GT-Power, FISITA 2018 World Automotive Congress, Oct 2018, India.

List of figures

Figure 2.1: Idealised diesel cycle 3
Figure 2.2: Typical CI engine heat-release-rate diagram identifying different diesel combustion phases 4
Figure 2.3: Engine Fuel Consumption Map (BSFC in g/kW.h, 1.9l TDI diesel engine) 5
Figure 2.4: NG units: (a) spark ignited (b) CI dual-fuel (c) HPDI dual-fuel 6
Figure 2.5: Fuel economy standards for light-duty vehicles: US vs. EU 12
Figure 2.6: Commercial Vehicles Sales 12
Figure 2.7: EU greenhouse gases emissions (Index 1990 = 100) 13
Figure 2.8: European Stationary Cycle (ESC) 15
Figure 2.9: Temporal sequence of John Dec's diesel combustion model 17
Figure 2.10: Diffusion flame combustion: John Dec's model 18
Figure 2.11: Combustion phases 19
Figure 2.12: Fuel jet diffusion flame 20
Figure 2.13: Fuel vapour and air concentration as well as temperature variation around diffusion flame 20
Figure 2.14: Phi-T diagram 21
Figure 2.15: Progress of conventional H2-diesel dual-fuel combustion 22
Figure 2.16: Main stages of fuel gas combustion in air 23
Figure 2.17: Ignition Delay vs. equivalence ratio 23
Figure 2.18: Heat release components of dual-fuel combustion (a) light load (b) heavy load 24
Figure 2.19: Hydrogen supply pathways: (a) off-board electrolysis (b) off-board methane steam reformation (c) on-board diesel fuel reformation 26
Figure 2.20: Hydrogen-diesel conceptual combustion model 28
Figure 2.21: Numerical modelling classification 29
Figure 2.22: Wiebe function for various parameters 31
Figure 2.23: Combustion model classification 32
Figure 2.24: Schematic of Packet Spray model 33

Figure 2.25: Schematic of mass system within each package 34
Figure 2.26: Flowchart of computations process in Packet Spray model 34
Figure 2.27: Laminar vs turbulent flame front 35
Figure 2.28: The turbulent structure of intake flow jet 36
Figure 2.29: The turbulent eddy structure 37
Figure 2.30: Measured (solid line) vs. extrapolated (dotted line) for uL, stoichiometric iso-octane/air mixture compressed from 1 bar and 298K to specified pressure. (dashed line represents the possible unstable uL) 38
Figure 3.1: 3D design of test engine 41
Figure 3.2: Schematic of intake and exhaust system 42
Figure 3.3: Components of diesel fuel system 43
Figure 3.4: Schematic of Zeuch's method 44
Figure 3.5: Hydrogen and oxygen fumigation setup 46
Figure 3.6: Hydrogen and oxygen supplying control panel 47
Figure 3.7: Test rig – Depicting gaseous pipelines jointing point: oxygen (blue circle), hydrogen (red circle) 49
Figure 3.8: Screenshot of combustion analyser program, YanTech® 50
Figure 3.9: Components of VVA system 51
Figure 3.10: Extreme intake valve profiles 52
Figure 3.11: exhaust and intake valve lift profiles 53
Figure 3.12: Schematic of staggered grid approach: scalars calculated at centroid, vector quantities at boundaries 57
Figure 3.13: Flowchart of flow calculations within "EngCylFlow" 59
Figure 3.14: Typical injection data: injection mass flow rate vs. time for different rail pressures and electrical energizing times 60
Figure 3.15: a) Injected mass contour b) Map of injection profiles 61
Figure 3.16: Injection rate map for the test engine 61
Figure 3.17: Flowchart of combustion process 62
Figure 3.18: Cut-off frequency sweep of low-pass filtration - HRR 64

Figure 3.19: Ringing effect: (left) on cylinder pressure (right) on normalised mass fraction burned 65
Figure 3.20: In-cylinder energy balance, HF = 15% 65
Figure 3.21: Normalised MFB: Test measured vs. TPA calculated 66
Figure 3.22: three zones of DIPulse model 67
Figure 3.23: Flowchart of DIPulse calculations process 68
Figure 3.24: Flowchart of SITurb calculations process 70
Figure 3.25: Flame propagation in GT DualFuel model [Walther (84)] 72
Figure 3.26: incremental flame growth in GT DualFuel model 73
Figure 4.1: The selected test points with ESC13 points over the HD engine operational map 75
Figure 4.2: Use of pre-injection to reduce engine noise_A25 (a) diesel-only (H0) (b) dual-fuel (H65) 76
Figure 4.3: H2-diesel: Combustion characteristics 77
Figure 4.4: Key attributes of the selected cases at A25 78
Figure 4.5: H2-diesel at A25: Cylinder pressure (left) and burn rate (right) 79
Figure 4.6: Key attributes of the selected cases at A50 80
Figure 4.7: H2-diesel at A50: Cylinder pressure (left) and burn rate (right) 81
Figure 4.8: Exhaust Emissions and Performance (A25 and A50) 82
Figure 4.9: Emissions alteration of highest HFs (H65 at A25 and H35 at A50) to the diesel baseline 83
Figure 4.10: O2 enrichment combustion effects: (a) 0% EGR (b) 30% EGR 84
Figure 4.11: O2 enrichment: In-cylinder conditions 85
Figure 4.12: O2 enrichment: Emissions and indicated efficiency 86
Figure 5.1: Residual plot for fitted model for DOE of baseline diesel-only single injection at A50 89
Figure 5.2: Coefficients plot of quadratic least squares fitting surface, diesel baseline single-injection at A50 90
Figure 5.3: DOE Latin Hypercube results, single injection diesel-only mode 90

Figure 5.4: Discrete-Grid Optimising of DIPulse, single injection diesel-only combustion in A50 91
Figure 5.5: Brent Optimising of DIPulse, single injection diesel-only combustion in A50 92
Figure 5.6: Burnrate RMS optimising and sensitivity analysis results:(a) Brent (b) Discrete-Grid, single injection diesel-only combustion in A50 93
Figure 5.7: Typical settings for NGSA-III optimiser 95
Figure 5.8: NSGA-III optimisation result of single injection diesel-only in A50 95
Figure 5.9: Cylinder pressure estimation by DIPulse optimised by NSGA-III (single injection, diesel-only in A50) 96
Figure 5.10: Sensitivity analysis: NSGA-III optimisation, single injection diesel-only in A50 97
Figure 5.11: Burnrate RMS contour in terms of entrainment and diffusion multipliers: (a) single-injection (b) pre-injection diesel-only at A50 97
Figure 5.12: Calibrated DIPulse RLTs: (a) H0 (b) H15 (c) H30 at A50, single-injection 99
Figure 5.13: DI-Wiebe vs measured burn rate, H0 at A50 (a) cumulative (b) normalised burn rate 100
Figure 5.14: DI-Wiebe vs measured burn rate, H15 at A50 100
Figure 5.15: DI-Wiebe vs measured burn rate, H30 at A50 100
Figure 5.16: Entrainment multiplier value sweep 102
Figure 5.17: Entrainment multiplier effect on combustion: (a) duration (b) timing 102
Figure 5.18: Cd_Nozzle effect on burnrate: H0 at A25, Cd_Nozzle = (a) 0.7 (b) 0.4 103
Figure 5.19: Ignition delay multiplier value sweep 103
Figure 5.20: Premixed rate multiplier value sweep 104
Figure 5.21: Diffusion rate multiplier value sweep 104
Figure 5.22: Max cylinder pressure vs diffusion rate multiplier 104
Figure 5.23: CTFS value sweep – gasoline SITurb model 106
Figure 5.24: CTFS effect on combustion: (a) duration (b) timing – gasoline SITurb model 106

Figure 5.25: CTFS value effect on turbulent parameters: (a) normalised turbulence intensity (b) normalised integral length scale (c) flame radius – gasoline SITurb model 107
Figure 5.26: CTLS value sweep – gasoline SITurb model 108
Figure 5.27: CDE value sweep – gasoline SITurb model 109
Figure 5.28: CFKG value sweep – gasoline SITurb model 109
Figure 5.29: SITurb calibration results for pivotal point (4 bar IMEPn, 2000 rpm) 110
Figure 5.30: In-cylinder energy balance (2000 rpm – 4 bar IMEPn) – gasoline SITurb model 110
Figure 5.31: Calculated flame speeds: (a) laminar (b) turbulent (4 bar IMEPn, 2000 rpm) 111
Figure 5.32: Flame speed ratio (4 bar IMEPn, 2000 rpm) 111
Figure 5.33: Flame speeds: 4 other swept loads – gasoline SITurb mode 112
Figure 5.34: Cylinder pressure prediction at A25 - DualFuel model 113
Figure 5.35: Burn rate prediction at A25 - DualFuel model 114
Figure 5.36: Mass burned fraction for selected cases at A25 – DualFuel model 115
Figure 5.37: Flame speeds of selected test cases at A25 – DualFuel model 116
Figure 5.38: Flame speed ratio at A25 – DualFuel model 117
Figure 5.39: In-cylinder temperature during (a) entire cycle (b) combustion process at A25 – DualFuel model 118
Figure 5.40: Flame radius for selected test cases at A25 – DualFuel model 118
Figure 5.41: Specific heat ratio at A25 – DualFuel model 119
Figure 5.42: In-cylinder Energy balance evaluation at A25 – DualFuel model 120

List of tables

Table 2.1: Physical properties: Hydrogen, Methane and Diesel 7

Table 2.2: EU Emission Standards for Heavy-Duty Diesel Engines: Steady-State Testing 14

Table 2.3: CO2 emissions of various hydrogen delivery pathways 28

Table 3.1: Technical specifications of test engine 40

Table 3.2: Technical specifications of diesel injector 43

Table 3.4: Installing location of thermocouples 51

Table 3.5: Intake and exhaust valve timings 52

Table 3.6: Combustion parameters comparison: Net. Heat release post-processed results vs. TPA results 66

Table 4.1. Engine Operating Conditions of H2 enrichment 74

Table 4.2: Operating Conditions: O2 enrichment of intake air 84

Table 5.1: Recommended range for DIPulse multipliers 88

Table 5.2: Recommended population size for NGSA-III optimiser 94

Table 5.3: Optimised DIPulse multipliers by NSGA-III (single injection diesel-only in A50) 96

Table 5.4: DI-Wiebe constants for three HFs: H0, H15 and H30 at A50 101

Table 5.5: Turbulent flame speed multiplier adjusted for all swept loads – gasoline SITurb model 112

Table 5.6: Fixed calibrating multipliers for all swept loads – gasoline SITurb model 112

Table 5.7: Calibration multipliers for prediction of selected test cases at A25 – DualFuel model 114

Acknowledgement

First and foremost, I'm thankful to the almighty God for all mercy and blessing I have always received in my life. Particularly, God was the main supporter of mine during my stay in the estrangement.

Indeed, studying PhD in UK was an unforgettable adventure of my life in recent 4 years. Being supported and motivated by my supervisor, Prof. Alasdair Cairns, I was able to succeed in the challenges encountered during this mission. He was not only giving me the academic and technical advices, but he was also very helpful by guiding me for better reconciliation with UK society.

I would like to thank the technicians: Chris, Andy and Eamon for their assistance in commissioning the test rig. I'm also grateful to my colleagues: Thompson, Mack, Ian, Vini, Wei, Akira, Yusof, Mike and Taufik. All these gentlemen contributed in different aspects of this work someway.

Finally, I want to appreciate my parents for all their sincere efforts in my life. Their love and motivations has been my momentum in achieving my goals. The emotional support of theirs and my brother, Foad has been heart-warming remotely during my PhD.

List of acronyms

1D: one dimension

3D: three dimensions

ACEA: European Automobile Manufacturers' Association

AFR: air fuel ratio

ASI: crank angle after start of injection

ATDC: after top dead centre

BSFC: brake specific fuel consumption

CA10: crank angle at 10% mass fraction burned

CA50: crank angle at 50% mass fraction burned

CA90: crank angle at 90% mass fraction burned

CAD: crank angle degrees

CAFE: corporate average fuel economy

CARB: California Air Resources Board

CFD: computational fluid dynamics

CI: compression ignition

CNG: compressed natural gas

CO: carbon monoxide

CO2: carbon dioxide

COV_IMEPn: coefficient of variation of IMEPn

DAQ: data acquisition

DI: direct injection

DOE: design of experiment

DPF: diesel particulate filter

ECR: effective compression ratio

ECU: engine control unit

EGR: exhaust gas recirculation

EHG: electro hydrogen generation

ELR: European Load Response

EOC: end of combustion

EPA: environmental protection agency

ESC: European stationary cycle

ETC: European transient cycle

EU: European Union

EVC: Exhaust valve closure

EVO: Exhaust valve opening

FAR: fuel air ratio

FCV: fuel cell vehicle

FID: flame ionisation detector

FSN: filter smoke number

FSR: flame speed ratio

FTP: federal test procedure

GHG: greenhouse gas

GT: Gamma Technologies®

HC: unburned hydrocarbon

HCCI: homogeneous charge compression ignition

HD: heavy duty

HF: hydrogen fraction

HPDI: high pressure direct injection

HRR: heat release rate

HSDI: high speed direct injection

ICE: Internal Combustion Engine

IEA: International Energy Agency

IMEPn: indicated mean effective pressure (net)

ISCO: indicated specific CO emission

ISCO2: indicated specific CO2 emission

ISHC: indicated specific HC emission

ISNOx: indicated specific Nox emission

ISSoot: indicated specific soot emission

IVC: Intake valve closure

IVO: Intake valve opening

LFL: lower flammability limit

LHV: lower heat value

LHV: lower heating value

LIVC: late intake valve closure

LNG: liquefied natural gas

LP: low pressure

LPG: liquefied petroleum gas

LTC: low temperature combustion

MFB: mass fraction burnt

MIT: Massachusetts Institute of Technology

mpg: miles per gallon

NDIR: non-dispersive infra-red

NEDC: new European drive cycle

NG: natural gas

NGV: natural gas vehicles

NNFCC: National Non-Food Crops Centre

NOx: nitrogen oxide

OFAT: one-factor-at-a-time

OICA: Organisation Internationale des Constructeurs d'Automobiles

OPEC: organisation of petroleum exporting countries

PC: personal computer

PCCI: premixed charge compression ignition

PFI: port fuel injection

PI: positive ignition

PM: particulate matter

Pmax: maximum cylinder pressure

Pmax_CA: crank angle of maximum cylinder pressure

PRR: pressure rise rate

RMS: root mean square

SCR: Selective catalytic reduction

SI: spark ignition

SOC: start of combustion

SOF: soluble organic fraction

SOI: start of injection

TDC: top dead centre

Tmax_CA: crank angle of maximum cylinder temperature

TPA: three-pressure analysis

TTL: transistor transistor logic

UCL: University College London

UK: United Kingdom

UNFCC: United Nations Framework Convention on Climate Change

US: United States

VVA: variable valve actuation

WHSC: world harmonized stationary cycle

Chapter 1: Introduction

1.1 Preface

There is no doubt that climate change is one of the most critical issues of the modern era. During recent decades, the treaties such as [Kyoto Protocol (1)] and [Paris Agreement (2)] have been adopted by the UNFCCC with the aim of stabilising the greenhouse gas (GHG) emissions at the levels which will impede the disastrous anthropogenic interference with the climate system [UN (3)]. Most recently, the Paris Agreement reached in December 2015, set the target of retaining the increase of earth average temperatures below 2 °C above pre-industrial record.

Hence, the promises to combat the climate change have become crucially binding worldwide on reducing the GHG, particularly the carbon dioxide (CO2) which is the prime culprit blamed for rising the global temperature. The transport sector in general and commercial vehicles in particular are the major contributors to the existing circumstances. Within UK, the heavy goods vehicles (HGVs) are responsible for 15.7% of CO2 emission in the transport sector [UK statistics (4)]. Thus, the manufacturers are obliged to abide with severe regulations, with more emphasis on improving the Heavy Duty (HD) engines as passenger cars shift to more electric solutions.

HD diesel engine can hardly take advantage of the conventional measures which are mostly applicable to the engines of passenger cars. Nevertheless, these engines can be dual-fuelled with various fuels like natural gas (NG), ethanol, hydrogen, etc. In fact, the dual-fuel combustion has opened a pathway in recent years to the sustainable operation of HD engines in the transport sector by significant reduction of CO2 emission.

1.2 Research objectives

The currently reported work was constituted of three main objectives:

- Substituting the diesel fuel with hydrogen in a HD diesel engine.
- Performance amelioration and decarbonisation of a freight vehicle engine.
- Numerical study of H2-Diesel combustion.

In addition to hydrogen, oxygen as another product of water electrolysis carried out in the electro hydrogen generation machine mentioned in Section 3.4 was introduced into the diesel engine and its effects was studied.

1.3 Thesis outline

This thesis is structured in 7 chapters as follow:

- **Chapter 1:** is the introduction and outline for the reported work.
- **Chapter 2:** reviews an inclusive literature of fundamentals of diesel engines with alternative gaseous fuels with relevant works and statistics. In addition numerical modelling classification as well as specific numerical models are discussed.
- **Chapter 3:** describes the experimental methodology with technical specifications of all measurement devices. Also, features of the simulation program as well as its optimisation capability as well as GT phenomenological models are explained.
- **Chapter 4:** presents the experimental evaluation of hydrogen and oxygen enrichment of the test engine.
- **Chapter 5:** the baseline diesel-only and dual-fuel modelling results are set out in this chapter with detailed discussion.
- **Chapter 6:** summarises the findings of experimental and numerical studies with recommendations for the future work.
- **Chapter 7:** sets out the list of references.

Chapter 2: Literature Review

2.1 Overview of IC engine thermodynamics

The IEA World Energy Outlook shows that hydrocarbon fuels will still carry on supplying 90% of transportation energy by 2040. Electric vehicles are emerging rapidly, but generating electricity is not capable of satisfying the whole needs of electrical transport sector without CO2 penalties. However, it is not completely emission-free. Hence, commercial vehicles will use ICEs as their powertrain for foreseeable future.

ICEs use various fossil or renewable fuels. Natural gas or fuel oils like gasoline and diesel are the conventional fuels which were used since petroleum exploitation in 19th century. Besides, renewable energy is seen as a sustainable source with less Greenhouse Gas (GHG) emission. Biofuel can be produced biologically like biodiesel derived from vegetable oils or it can be produced chemically using renewable energy sources such as steam reformation of methane for hydrogen production [ICE (5)].

As seen in Figure 2.1, the idealised diesel cycle follows 4 discrete processes: two isentropic compression (1-2) and expansion (3_b-4) processes comprising of work done on or by system. The constant-volume endothermic process (2-3_a) simulates the premixed combustion (process bc in Figure 2.2) followed by the constant-pressure (3_a-3_b) mixing-controlled diffusion combustion (process cd in Figure 2.2) which were triggered by diesel injection near the end of compression and entrained by compressed air. The exothermic constant-volume process (4-1) presumes the end of cycle for reaching the initial state [Diesel Cycle (6)].

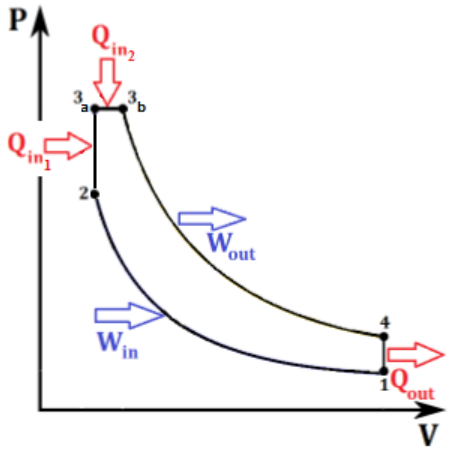


Figure 2.1: Idealised diesel cycle

As observed in Figure 2.2, the heat release diagram of a typical CI combustion can be specified in three distinct stages [Heywood (7)]:

1. Premixed combustion (bc): the rapid onset of premixed flame results in high heat release rates as it will be surcharged to the prepared fuel for burning. This stage resembles to a significant fast in-cylinder pressure rise and its released heat equates Q_{in_1} (Figure 2.1).

2. Mixing-controlled diffusion combustion (cd): Despite of various involved processes (fuel atomisation, vaporisation, pre-flame chemical reactions), the burn rate is regulated by the mixture availability rate for combustion. This is a descending heat release period equates Q_{in_2} (Figure 2.1) which lasts approx. 40 crank angle degrees (CAD). (NB. stage 1 and 2 ordinarily consume approx. 80% of the total fuel.)

3. Late Combustion phase (de): This 'tail' of heat release corresponds to burning of the remaining 20% of total fuel and the fuel-rich combustion products (soot). This final burning carries on slowly (lower heat release rate) as in-cylinder temperature drops during expansion.

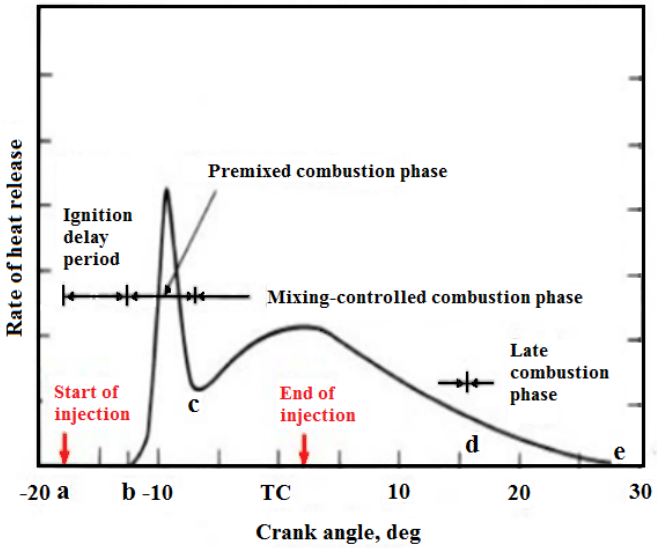


Figure 2.2: Typical CI engine heat-release-rate diagram identifying different diesel combustion phases [Heywood (7)]

The brake fuel consumption of a 1.9l TDI diesel engine is superimposed on a performance map in Figure 2.3. To retain lower exhaust particulates, diesel engines burn a lean combustion; hence engine power is smoke constrained. By moving from the optimum operating point that returns minimum fuel consumption in all four highlighted directions, the BSFC (brake specific fuel consumption) increases [Ferguson (8)]:

- Higher engine speed: this results in more friction losses.
- Lower engine speed: the heat losses would increase.
- Higher engine load: mixture needs to be enriched above the φ = 1.
- Lower engine load: the friction gets the substantial part of the indicated work.

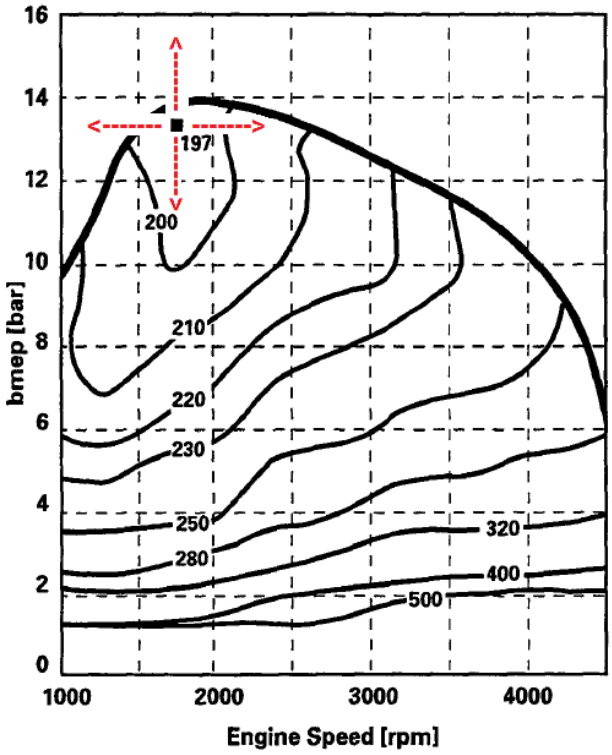


Figure 2.3: Engine Fuel Consumption Map (BSFC in g/kW.h, 1.9l TDI diesel engine) [Georgi et al. (9)]

2.2 Alternative gaseous fuels

2.2.1 Natural gas and biogas

Compressed Natural Gas (CNG) can be exploited from oil reserves naturally. Natural gas may be obtained from renewable sources such as water treatment or landfill which qualifies as advanced biofuel.

Despite of storage tank placement issues, Natural Gas Vehicles (NGVs) have less maintenance expenses. Due to gaseous state, better fuel-air mixing typically occurs. However, there is no fuel loss from evaporation due to sealing the fuel system. According to Table 2.1, CNG has a narrow flammability range (5 - 15% Vol) comparing with hydrogen, so it is less probable to ignite [CNG (10)]. Most importantly, CNG has less emissions and better performance. According to CARB, conventional ULSD emits 94.7 gCO2e/MJ while

CNG lifecycle GHG emissions is 67.7 gCO2e/MJ. It is worthwhile to mention that bio-methane emits much lower CO2, 11.26 gCO2e/MJ. The corresponding value for H2 from NG reforming (including liquefaction and re-gasification) is 142.2 gCO2e/MJ [arb.ca.gov (11)].

CNG differs from Liquefied NG (LNG) as it is a high pressure (supercritical) fluid at ambient temperature but LNG is a liquid stored at low temperature with almost ambient pressure. Natural gas is transported in LNG form over lengthy distances and is then transformed into CNG for end usage [CNG (10)]. As of 2013, there are more than 18 million NGVs worldwide. Iran, as the 1st ranked country with largest fleet of NGV (3.5 million), has 2335 CNG fuelling stations which supply approximately one quarter of Iran's transport fuel consumption [Financial Tribune (12)].

The current NG units can be divided to three main categories as depicted in Figure 2.4. The most conventional system comprises the stoichiometric spark-ignited type which NG can be added whether via PFI or DI system ignited by a spark plug. Although, it has less complexity, its efficiency is exacerbated due to high temperature combustion. Lean-burn gas engines have higher efficiency due to lower gas temperatures and no throttling pumping loss. Ignition source for the NG bulk mass burn is served by diesel injection. More recently, the High Pressure Direct Injection (HPDI) has been developed for introducing NG and diesel directly into the cylinder. Although, HPDI requires more expensive injector, but it benefits higher volumetric efficiency and power output cf. PFI designs [May (13)].

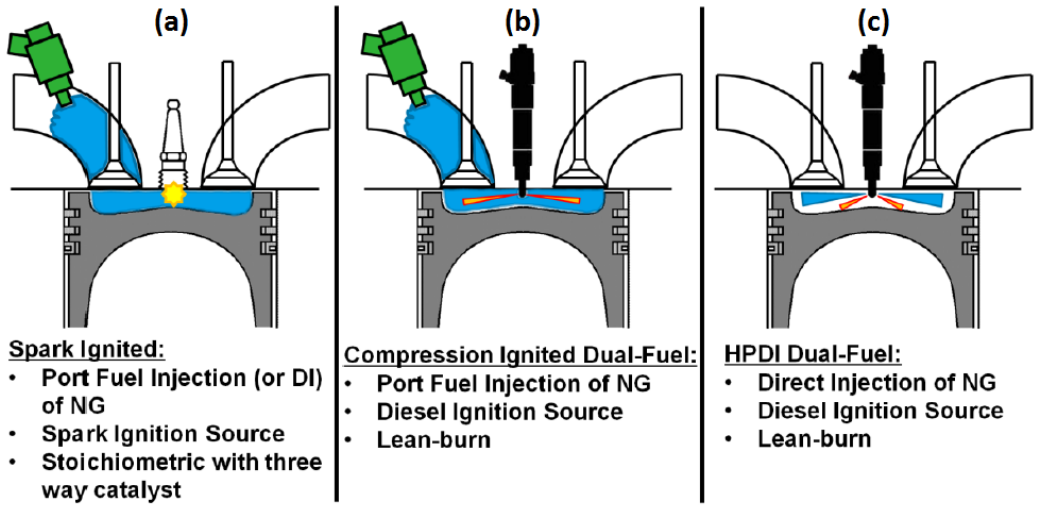


Figure 2.4: NG units: (a) spark ignited (b) CI dual-fuel (c) HPDI dual-fuel [May (13)]

As a renewable energy source, biogas is obtained from organic waste and contains predominantly methane (50-75%). This gas needs upgrading to acquire purified bio-methane which has the capability of running 17% of vehicles within UK [Biogas (14)]. Based on the NNFCC survey (map above), there are 401 anaerobic digestion plants in UK (April 2017) which have the capacity of 363 MW in total [NNFCC (15)]. As the pioneer of renewable energy producer in Europe, Germany has built 9,209 biogas power plants with capacity of 4,237 MW in total by end of 2016 [GBA (16)].

Table 2.1: Physical properties: Hydrogen, Methane and Diesel [Wimmer et al. (17)]

Parameter	Hydrogen	Methane	Diesel
Density at 0 ˚C [kg/m^3]	0.089	0.72	830
Stoichiometric air/fuel ratio	34.3	17.2	14.5
LHV [MJ/kg]	120	50	42.5
Mixture Calorific value at λ =1 [MJ/m^3]	3.2	3.4	3.83
Boiling Temperature [˚C]	-253	-162	180 - 360
Ignition Limits [Vol%, λ]	4 - 75%, 0.2 - 10	5.3-15%, 0.7 - 2.1	0.6 - 5.5%, 0.5 – 1.3
Min Ignition Energy at air (λ =1) [mJ]	0.02	0.29	0.24
Auto-ignition Temperature [˚C]	585	595	~250
Laminar Flame Speed at λ=1 [m/s]	2.0	0.4	0.4 - 0.8
Carbon Content (Mass %)	0	75	86

2.2.2 Hydrogen usage in ICEs

Historically, the hydrogen-filled Graf Zeppelin burning in 1937 is a reminder of the hazardous application of hydrogen. However, this catastrophe did not stop the attempts for applying hydrogen as the propellant fuel in different sorts of vehicles such as space rockets, ICE and fuel cell automobiles. Hydrogen is typically viewed as energy carrier rather than fuel itself. Most of the existing hydrogen fuel supply is produced from fossil fuels like natural gas, oil and coal via partial oxidation or steam reforming. One other method, electrolysis of water, is less popular due to high electricity consumption but provides high purity. Therefore it would be a sustainable fuel if its manufacturing problems can be solved.

Hydrogen storage and transportation is usually in compressed, liquefied in metal hybride form or absorbed by particular alloys [Karim (18)].

Approximately 95% of hydrogen is supplied from methane through a process known as 'steam reformation' which yields no overall benefit in CO2 per equivalent mass of diesel. Another method involves electrolysis by renewable energy, which is a zero carbon route but is very costly. Alternatively, a novel possibility for hydrogen acquirement is via on-board steam reformation of part of the liquid hydrocarbon fuel, which improves the overall system efficiency by about 5% via waste exhaust heat recovery [Morgan et al. (19)]. Nevertheless, the vision of a "hydrogen economy" is only foreseeable when its required production energy is totally supplied from green renewable sources. If so, transportation and electrical needs can be fulfilled using hydrogen fuel cells [Karim (18)].

Storage is among the main areas for development of hydrogen power due to the relevant safety issues and physical properties of hydrogen. Although distinct crystalline materials have been suggested for hydrogen storage, hydrides are used for storing significant quantities of hydrogen gas. In 2008, a hydrogen tank using an alloy found by Robin Gremaud could have 60% less weight than a battery pack [ScienceDaily (20)]. Besides, cryogenic tanks have other preferences which attempt to improve compatibility, expense and volumetric capacity. As an example of efforts in this area, BMW previously adopted cryogenic tanks for a 7 series mini-fleet to demonstrate improved driving range. The distribution of hydrogen for vehicles at filling stations needs remarkable infrastructure and huge investment. As of 2018, there are 41 public hydrogen stations in the US, with 36 of those located in California [DOE (21)].

Several automotive manufacturers including BMW, Ford and Mazda have attempted to utilise hydrogen as an alternative fuel for the IC engine. The BMW Hydrogen 7, powered by a hydrogen IC engine, was developed by BMW between 2005 and 2007. This demonstrator adopted the same 6L V12 engine as the gasoline production model but with modifications to allow for dual fuel operation. Overall, the combustion system matched the efficiency values of a baseline turbo-diesel engine at a maximum of 42% [BMW Hydrogen 7 (22)].

Elsewhere, Ford also developed the first vehicle in North America exclusively powered by a hydrogen fuelled IC engine (H2ICE). A Zetec based 2 litre H2ICE with a port fuel injection (PFI) system was integrated into a P2000 passenger sedan. Comparing with gasoline powered 2L Zetec, hydrogen powered CO2 emissions were reduced to 0.4% of that of the gasoline case with 18% higher metro cycle fuel economy [Szwabowski et al. (23)]. In later work, to achieve the stringent 2010 Phase II Heavy Duty emission standards, Ford re-designed a V10 Triton engine with the aim of running an E-450 bus with hydrogen. Following this, the Ford Focus fuel cell vehicle (FCV) was developed as an alternative hydrogen fuel cell vehicle. Such FCV vehicles are widely considered to offer considerable promise but only provided the current high costs of fuel cell technology can be reduced in the longer term. Hence, in the medium term (at least), the IC engine remains dominant [Natkin et al. (24)].

There have been numerous other attempts to adopt hydrogen in IC engines. Revolve UK modified the engine of a Ford Transit 2.2L Puma Diesel to operate with PFI of hydrogen as the main fuel. As the ignition source, diesel pilot injection was used to allow a permanent dual-fuel mode [LCVP (25)]. More recently, Alset developed a hybrid hydrogen-gasoline system that allowed the vehicle to use both fuels individually or at the same time. This technology was implemented on the Aston Martin Rapide S, which was the first vehicle completing the 24 hour Nürburgring race with hydrogen technology [Alset (26)].

The injection strategy has considerable influence on the hydrogen mixture's homogeneity and stratification at ignition. Hydrogen direct injection (DI) could have further benefits rather than PFI due to providing more volumetric efficiency and avoiding irregular combustion such as backfire [Monemian et al. (27)].

Lund university researchers have had the earliest attempt of hydrogen HCCI combustion [Stenlåås et al. (28)]. Although H2 HCCI operating range is much limited than SI hydrogen operation, but HCCI mode showed better efficiency. In an optical study by Aleiferis et al. at UCL, hydrogen HCCI combustion was characterised by sweeping various equivalent ratios and intake air temperatures [Rosati et al. (29)]. This combustion was initiated by PFI of n-heptane prior to the main DI of hydrogen in a low compression ratio combustion chamber. The intake air needed to be preheated as the auto-ignition temperature of hydrogen is too

high. Considering significant ability of hindering CO2 and NOX intensely, the ideal zero emission engine can be realised as a rival to the fuel cell.

2.2.3 Hydrogen combustive properties

The unique physical properties of hydrogen make it quite different from conventional fuels, as indicated in Table 2.1. Due to the very low density, hydrogen's volumetric energy density is small relative to that of diesel even in a compressed storage tank or in liquid state. Hence, a large volume is needed for storing sufficient hydrogen to perform a requisite driving range [Lanz et al. (30)]. This fact highlights the benefits of hydrogen production through on-board reformation. According to Table 2.1, vast ignition limits (4–75% volumetric concentration in air), enables combustion over a wide domain of fuel-air mixtures including high efficiency lean operation. Furthermore, hydrogen has a relatively high flame speed that leads to higher efficiency [Cassidy (31)].

Hydrogen's high diffusivity facilitates forming a uniform fuel-air mixture readily. This is also advantageous in the case of a hydrogen gas leakage, with rapid dispersion [Lanz (30)]. Low ignition energy of hydrogen and high burning speed makes the mixture of diesel/hydrogen easier to ignite, hence, mitigating misfire and improving performance and emissions. Besides, by increasing the H/C ratio, hydrogen enhances the mixture's energy density at lean mixtures. However, the full load must be supplemented by some means of volumetric efficiency compensation, such as compound boosting [Lanz (30)].

Comparing with diesel, hydrogen has meaningfully higher specific energy by mass, lower heating value (LHV), enabling a significant proportion of required diesel fuel be substituted by hydrogen in a more cost effective way. However, diverse challenges remained are including high in-cylinder pressure rise rates and the occurrence of pre-ignition and flashback within the intake system, particularly under heavy loads. The high flame speed of hydrogen is favourable in terms of knock [Lanz (30)]. However, in-cylinder hotspots exposed during the intake stroke can serve as ignition sources for causing pre-ignition and flashback due to hydrogen's very low ignition energy. In addition, lubricant deposits or the sparkplug electrodes are also thought to initiate flashback [Lanz (30)].

2.3 Engine exhaust emissions

2.3.1 Emission regulations and statistics

Currently, several emission standards have been regulated around the world with the aim of governing air pollutants released into the atmosphere. Emission standards set quantitative limits on the permissible amount of specific air pollutants that may be released from specific sources over specific timeframes. They are generally designed to achieve air quality standards and to protect human health [Emission Standard (32)].

Due to differences in testing procedures and compliance systems, emissions standard within various territories are not comparable. For instance, while EU follows New European Drive Cycle (NEDC), Federal Test Procedure (FTP) is followed by Environmental Protection Agency (EPA) as the US emissions regulatory body. These drive cycles are distinct in duration, distance and vehicle speed plus driving conditions [Canis et al. (33)].

As a consequence of oil embargo by OPEC members in 1973, US regulated the first fuel economy standards. The Corporate Average Fuel Economy (CAFE) is a harmonic fleet average calculated each year by EPA for every car manufacturers. Following Energy Independence and Security Act of 2007, national fuel economy of 35 miles per gallon (mpg) is targeted by 2020. This program follows some motivations [Canis et al. (33)]:

- Electric and hybrid vehicles promotion
- Incentives for Natural gas vehicles
- Technological developments in order to reduce GHG.

Although, EU has not set a particular standard for fuel economy, the limitation is enforced on fuel consumption indirectly by introducing GHG emissions standards in term of grams of CO2 emitted per 1 km mileage. The latest target has been defined of 95 gCO2/km by 2020. Figure 2.5 shows higher EU equivalent fuel economy normalised to CAFE testing procedure [Canis et al. (33)].

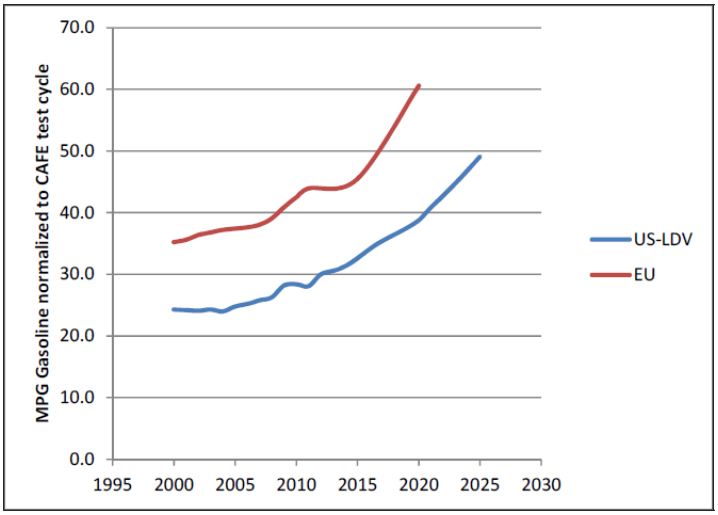


Figure 2.5: Fuel economy standards for light-duty vehicles: US vs. EU [Canis et al. (33)]

In addition to emission and fuel economy standards, several agreements and treaties had been agreed among countries to tackle the climate change issue. The latest agreement is obtained during the 2015 UN Climate Change Conference (COP 21) in Paris. The expected key result of these talks was an agreement to set a goal of limiting global warming to less than 2 degrees Celsius (°C) compared to pre-industrial levels [Paris Agreement (2)]. As global temperature rise is mostly a function of accumulated CO2 emissions over time, CO2 needs to be reduced to 'net zero' in order to stabilise temperature.

The OICA commercial vehicles sales statistics during a decade from 2005 to 2014 is presented in Figure 2.6. Although, the global sales were reduced significantly in 2008 due to global economic crisis for two years, it was monotonically increased afterwards. The consequence of financial crisis has been also reflected in the GHG emissions of the EU-28 by a drastic drop in 2008.

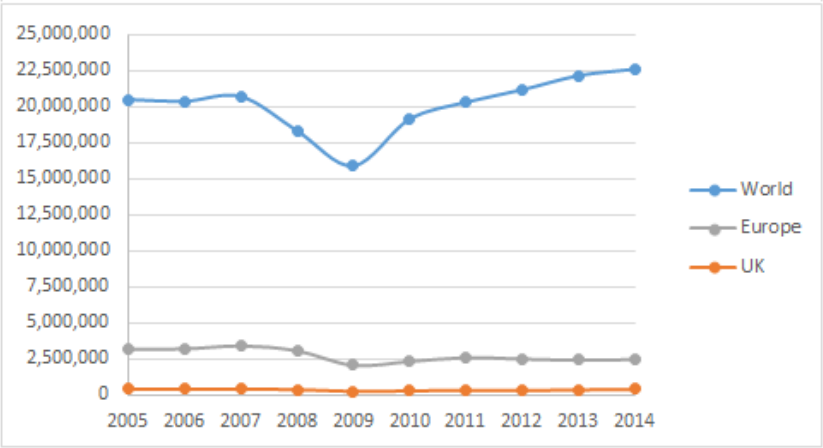


Figure 2.6: Commercial Vehicles Sales [OICA (34)]

As a determined contributor to the global efforts for confronting with climate change, EU could reduce its GHG emissions almost by a quarter since 1990, Figure 2.7. The main factors of this decrease are amelioration of energy efficiency and using less carbon intensive and more renewable fuels. This has resulted in dissociation of EU economic growth from its GHG emissions.

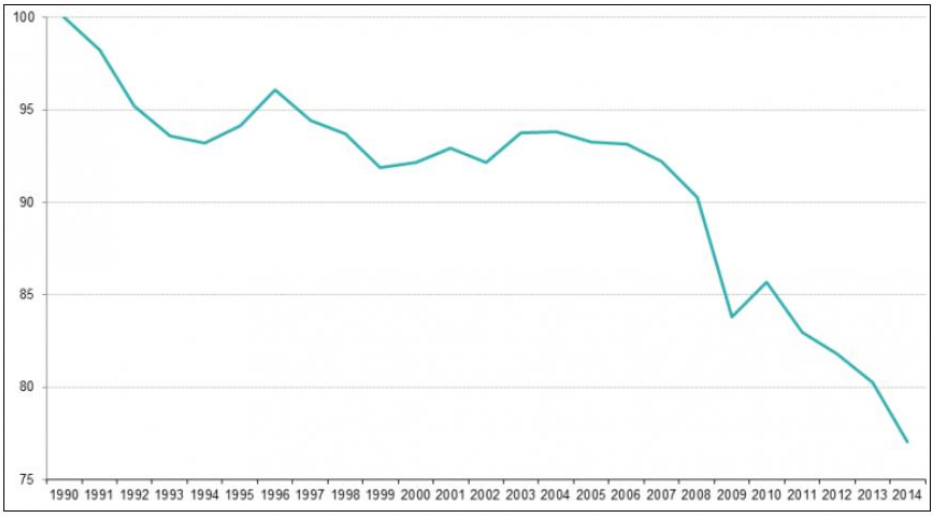


Figure 2.7: EU greenhouse gases emissions (Index 1990 = 100) [EU (35)]

As of 2008, it must be ensured that the net UK carbon account for the year 2050 is at least 80% lower than the 1990 baseline [UK (36)]. Within UK, while the total CO2 was reduced significantly (approx. 30%) since the baseline year 1990 until 2014, the CO2 emission in transport sector was almost unchanged representing 27.5% of total CO2 in 2014 [UK (4)]. In that year, CO2 emission of Heavy Goods Vehicles (HGVs) has experienced a 9% improvement compared with 1990. Despite of the fact that UK is on track to meet the second 'carbon budget' regarding the Climate Change Act 2008, transport sector has not contributed a major impact on CO2 emission due to increase of motor vehicles sales in recent years [OICA (34)]. As HGVs are accounted for 15.7% of UK transport sector's CO2 emission, the vehicle manufacturers have been required to additionally focus upon Heavy Duty (HD) vehicles [UK (4)].

2.3.2 Emission regulations for heavy-duty engines

The emission standards for heavy-duty engines apply to all motor vehicles with a technically permissible maximum laden mass over 3,500 kg, equipped with compression ignition (CI) engines or positive ignition (PI) natural gas (NG) or LPG engines. The Table 2.2 contains a

summary of the emission standards and their implementation dates for steady-state testing conditions [DieselNet (37)]:

Table 2.2: EU Emission Standards for Heavy-Duty Diesel Engines: Steady-State Testing [DieselNet (37)]

Stage	Date	Test	CO [g/kWh]	HC [g/kWh]	NOx [g/kWh]	PM [g/kWh]	Smoke 1/m
Euro I	1992, <= 85 kW	ECE R-49	4.5	1.1	8.0	0.612	
	1992, > 85 kW		4.5	1.1	8.0	0.36	
Euro II	1996.10		4.0	1.1	7.0	0.25	
	1998.10		4.0	1.1	7.0	0.15	
Euro III	1999.10 EEV only	ESC & ELR	1.5	0.25	2.0	0.02	0.15
	2000.10		2.1	0.66	5.0	0.10[a]	0.8
Euro IV	2005.10		1.5	0.46	3.5	0.02	0.5
Euro V	2008.10		1.5	0.46	2.0	0.02	0.5
Euro VI	2013.10	WHSC	1.5	0.13	0.4	0.01	

a – PM=0.13 g/kWh for engines < 0.75 dm^3 swept volume per cylinder and a rated power speed > 3000 rpm.

It is seen that regulatory emission test cycles have been changed several times; as the earlier ECE R-49 test cycle has been replaced by two cycles: the European Stationary Cycle (ESC) and the European Transient Cycle (ETC) since the Euro III stage (2000). Among these various test cycles, European Stationary Cycle (ESC) is the subjected to our focus of interest. The ESC test cycle was introduced together with the ETC (European Transient Cycle) and the ELR (European Load Response) tests by the Euro III emission regulation for emission measurement of heavy-duty diesel engines. The ESC is a 13-mode that was also referred to as OICA/ACEA cycle [DieselNet (38)]. The engine is tested on an engine dynamometer over a sequence of steady-state modes. The engine must be operated for the prescribed time in each mode, completing engine speed and load changes in the first 20 seconds. The specified speed shall be held to within ±50 rpm and the specified torque shall be held to within ±2% of the maximum torque at the test speed. Emissions are measured during each mode and averaged over the cycle using a set of weighting factors. Particulate matter emissions are sampled on one filter over the 13 modes. The final emission results are expressed in g/kWh [DieselNet (38)].

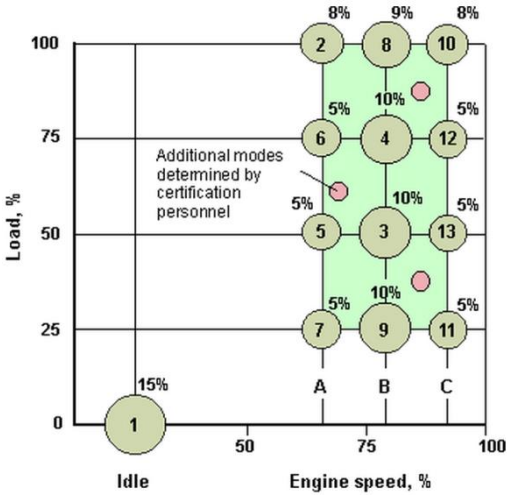


Figure 2.8: European Stationary Cycle (ESC) [DieselNet (38)]

The engine speeds are defined as follows [DieselNet (38)]:

1. The high speed (**nhi**) is determined by calculating 70% of the declared maximum net power. The highest engine speed where this power value occurs (i.e. above the rated speed) on the power curve is defined as **nhi**.
2. The low speed (**nlo**) is determined by calculating 50% of the declared maximum net power. The lowest engine speed where this power value occurs (i.e. below the rated speed) on the power curve is defined as **nlo**.
3. The engine speeds A, B, and C to be used during the test are then calculated from the following formulae:

$$A = nlo + 0.25(nhi - nlo)$$

$$B = nlo + 0.50(nhi - nlo)$$

$$C = nlo + 0.75(nhi - nlo)$$

During emission certification testing, the certification personnel may request additional random testing modes within the cycle control area (Figure 2.8). Maximum emissions at these extra modes are determined by interpolation between results from the neighbouring regular test modes. The ESC test is characterized by high average load factors and very high exhaust gas temperatures [DieselNet (38)].

2.4 Diesel combustion fundamentals

Understanding the performance ICEs requires a fundamental understanding of the combustion process which is affected by engine design, fuel injector operation, heat

transfer, turbulent flow and gas composition. Engine manufacturers need to design diesel engines which are compliant with severe emission standards while maintaining high thermal efficiency. Diesel combustion is a turbulent multi-modal phenomenon which occurs under rapidly varying high pressures and temperatures.

2.4.1 Dec diesel combustion model

As one of the most accepted models for diesel combustion, John Dec introduced a temporal-spatial phenomenological description of diesel jet ignition at Sandia National Laboratories (Figure 2.9). This model is based on several diverse optical studies done since 1992 until 1997 by Dec and Epsey:

- Liquid-phase fuel distribution [Dec and Epsey (41, 42)]
- Quantitative images of vapour-fuel/air [Dec and Epsey (42, 43)]
- Polycyclic Aromatic Hydrocarbons (PAHs) and soot distribution [Dec and Epsey (39, 44-47)]
- Soot particle size distribution [Dec and Epsey (45-47)]
- Diffusion flame structure [Dec and Epsey (40)]
- Auto-ignition chemiluminescence [Dec and Epsey (46)]

Diesel jet development is conceptualised from SOI until early mixing-controlled burn with ASI time scale which gives the crank angle after start of injection as explained in following steps. It's noteworthy that the jet interaction with cylinder wall and in-cylinder swirl was neglected in this model.

(a) Initial jet development (0.0^o - 4.5^o ASI): the initial three images (Figure 2.9) present liquid fuel evaporation. While this area only includes liquid fuel at injector vicinity, the entrained air evaporates the fuel liquid droplets. At 4.5^o ASI, the homogenous fuel/air mixture of equivalence ratio 2 to 4 has appeared [Dec (48)].

(b) Auto-ignition (3.0^o - 5.0^o ASI): while precise auto-ignition (AI) occurrence is not specified spatially and temporally, chemiluminescence is seen at 3.5^o ASI in downstream of jet by arrows under schematics. As fuel pyrolysis and PAHs formation are processed in volume between 4.5^o and 5.0^o ASI followed by soot formation from 5.0^o to 6.0^o ASI, it is probable that AI was happened by 4.5^o ASI [Dec (48)].

(c) First part of premixed burn spike (4.0^o - 6.5^o ASI): the PAHs which form homogeneously across jet's main portion, coincides with premixed burn spike in heat release curve [Dec (48)].

(d) Onset of the diffusion flame (5.5^o - 6.5^o ASI): at jet environs, diffusion flame forms between products of premixed fuel-rich burn and surrounding air. This slim diffusion flame entirely surrounds jet's downstream portion [Dec (48)].

(e) Last part of premixed burn spike (7.0^o - 9.0^o ASI): while, jet keeps penetrating by end part of premixed combustion, soot formation persists with maximum concentration at the head vortex near main edge at 8.0^o ASI. Due to turbulent mixing, larger soot particles are pulled inward the jet, making the diffusion reaction zone a thin surrounding layer. Nevertheless, the central jet is solely occupied by small soot particles [Dec (48)].

(f) First part of the mixing-controlled burn (9.0^o ASI to end of injection): early mixing-controlled emerges as minor changes to the jet since it was already formed when last part of premixed fuel was burnt. Diffusion flame's soot particles are larger than central jet's but smaller than head vortex [Dec (48)].

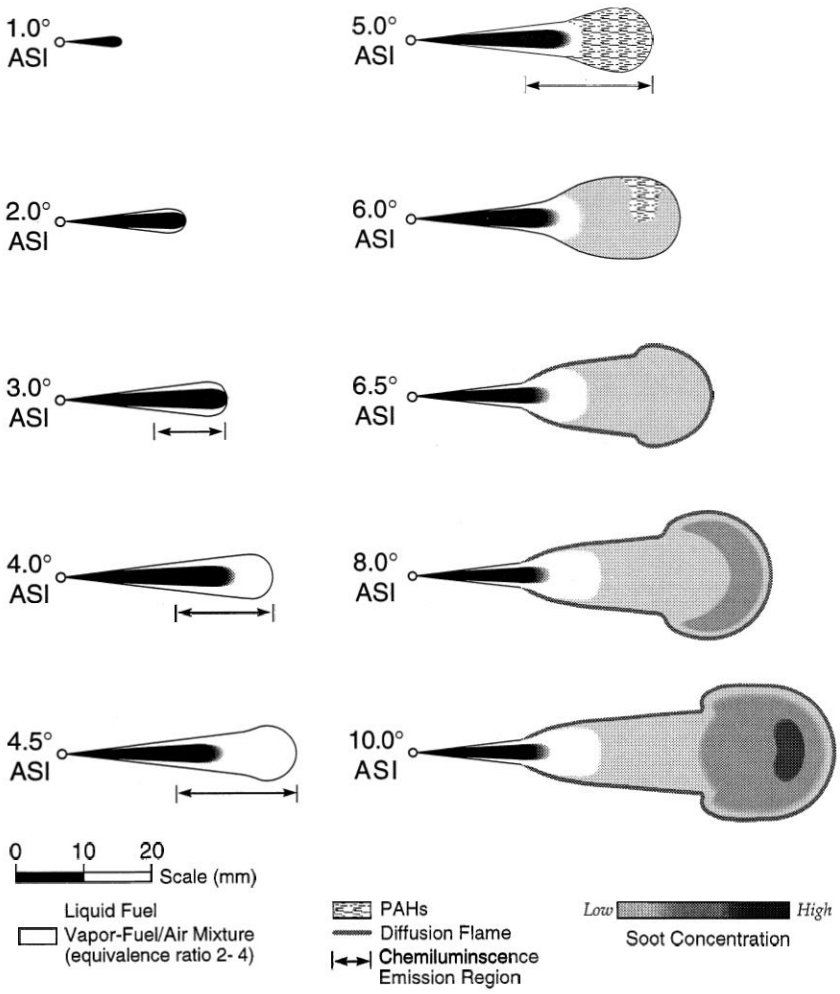


Figure 2.9: Temporal sequence of John Dec's diesel combustion model [Dec (48)]

Diffusion flame combustion with its corresponding emissions is shown in Figure 2.10 presenting thermal and chemical variations. Initially, the liquid fuel spray penetrates into high temperature air and gets heated up to 825K. This stage of diffusion flame unleashes 15% of total combustion heat. Inside the flame plume is now filled by rich combustion products (CO, HC and Particulates). While a slim layer of stoichiometric combustion has enclosed the flame plume, high temperatures of diffusion flame results in NOx formation. In addition, this diffusion cause fuel segments to be transformed into carbon dioxide and water vapour. Due to lack of sufficient oxygen inside the sheath of diffusion flame and the cold liquid fuel, diesel particulates form in significant volume [Flynn et al. (49)].

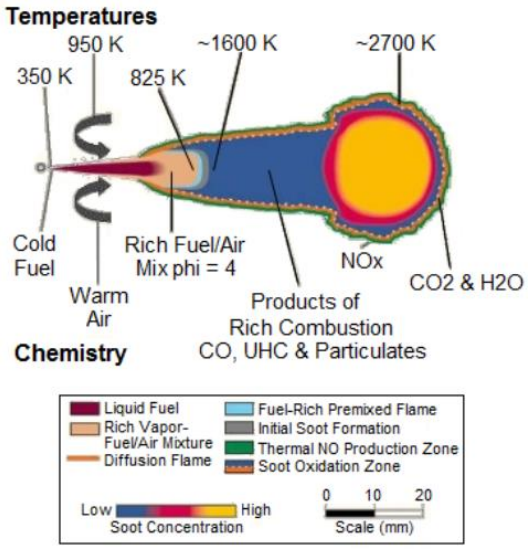


Figure 2.10: Diffusion flame combustion: John Dec's model [48]

According to [Sitkei (50)], the combustion process can be split into four distinct phases as depicted in Figure 2.11:

1. Ignition delay: defined as the interval between start of injection (SOI) and the first identifiable pressure increase.
2. Sudden pressure increase: covers the period from start of thermal ignition until when Pmax is reached.
3. Main combustion: refers to the interval between Pmax_CA and Tmax_CA.
4. Delayed post-combustion: In high-speed direct injection (HSDI) diesel engines, this phase lasts for approx. 50% of entire combustion duration.

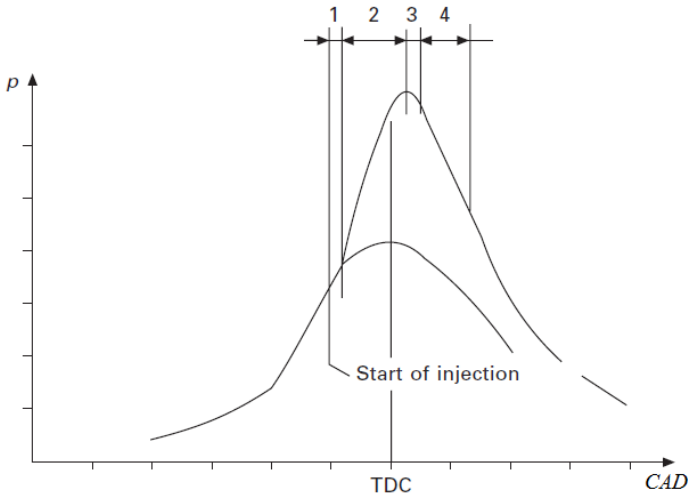


Figure 2.11: Combustion phases [Sitkei (50)]

2.4.2 Diffusion versus premixed combustion

Two main types of combustion flames include diffusion and premixed (fuel/air). In diffusion flame, fuel and oxidants are either separated or not fully premixed. Thus, reaction is controlled by fuel/air mixing rate. This physically controlled process is related linearly to local temperature while chemical reactions are dependent on temperature logarithmically and hence more rapid [Karim (18)].

Physical effectors such as liquid fuel atomization (breakup), penetration, air entrainment and vaporisation are controlling the spray development. Later, spray growth is depending on couple of factors: fuel-air reaction through momentum exchange, mixing process (improved by higher injection pressure) and swirl turbulence (dependent on intake port and combustion chamber geometrical design) [Karim (18)].

In comparison to premixed mode, diffusion flames have extended composition variability. Hence, they are more flexible to fuel quality and type than the premixed flame. Fuel jet entrainment and burning is shown in Figure 2.12. As fuel gets sprayed from orifice, it scatters and gets diluted by entrained air. A stoichiometric envelope is located at certain distance from discharge point. Prior to this place, fuel-rich mixture is existing while lean mixture envelopes are grown progressively further than this point. Therefore, a diffusion flame is appeared when fuel spray is ignited, while burning occurs easier around most reactant region which is available around stoichiometric envelope [Karim (18)].

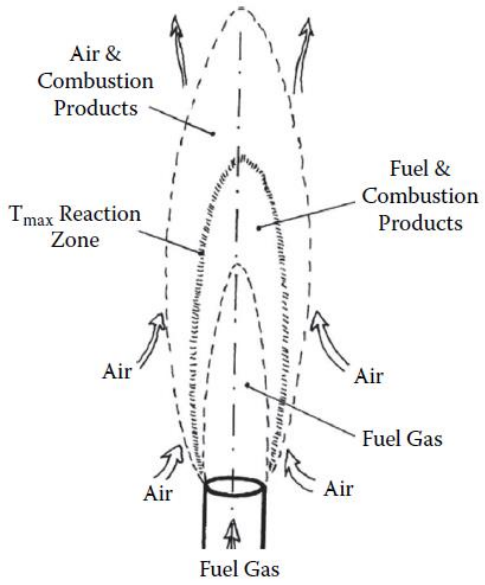


Figure 2.12: Fuel jet diffusion flame [Karim (18)]

The resultant temperature alters in axial and radial directions while the maximum values are surrounding stoichiometric region. Supposing a horizontal plane sectioned fuel spray, concentrations of fuel, oxygen and products are varying radially. In essence, comparable processes occur nearby fuel droplet burning (Figure 2.13). An extended region of fuel-air mixture is formed as fuel evaporates and spreads out to the entrained air [Karim (18)].

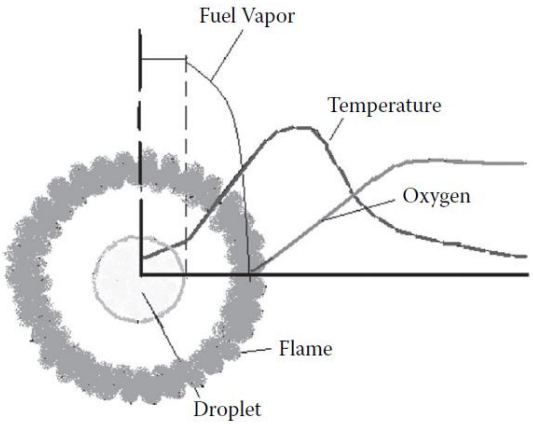


Figure 2.13: Fuel vapour and air concentration as well as temperature variation around diffusion flame [Karim (18)]

2.4.3 Theoretical analysis of the soot-NOx trade-off

The mechanism of PM formation needs to be clarified in order to plan for reducing this problematic emission. Soluble Organic Fraction (SOF) formation at low and medium load

operation relates well to HC formation (while this parameter reflects soot emission in high loads). Optical and gas sampling studies of diesel combustion have enabled both temporal and spatial resolved evaluations of soot concentration [Kamimoto et al. (51)].

Traditional trajectory of a HD diesel engine is superimposed on the equivalence ratio (phi) vs temperature map (Figure 2.14). This path begins with fuel injection. The phi reduces severely as fuel spray develops and gradual heating up is resulted by air entrainment and weak chemical reaction. However, some peripheral points of fuel spray set to high temperature reactions followed by auto-ignition of premixed mixture when reaching the end of ignition delay which results in a rising temperature quickly (90deg bend of arrows in Figure 2.14). In next process (diffusion combustion), the heat release and mixing rates determine the slope of combustion path while phi decreases and temperature increases. The combustion path travels firstly through soot formation zone followed by NOx zone [Zhao (52)].

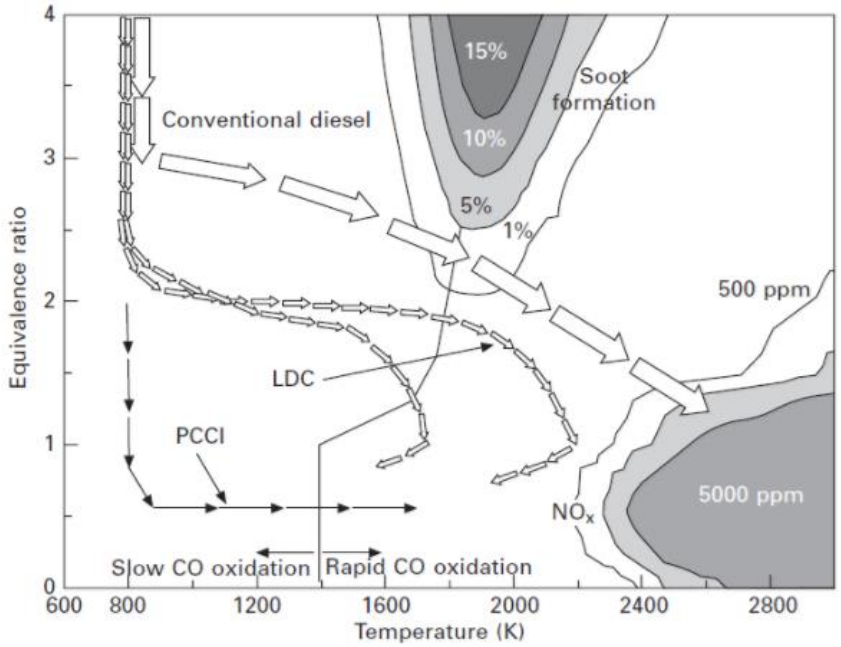


Figure 2.14: Phi-T diagram [Zhao (52)]

Studying various combustion modes, it is tried to avoid the soot and NOx formation zones as two paths presented in Figure 2.14. The PCCI track is formed by early DI in the compression stroke while P and T are pretty low which results in very low chemical reaction rate despite enough time for homogeneous mixing [Zhao (52)].

2.5 Dual-fuel diesel combustion

Dual-fuel engine operation relies on method of introducing gaseous fuel. The conventional approach is adding gaseous fuel into the intake air flow like SI engines. The enrichment can also be done at start of compression stroke allowing fuel gas be mixed with air before diesel injection. Both these ways can be named as premixed dual-fuel engines with fumigation mode of enrichment. Other method of enrichment includes direct injection of fuel gas both whether prior to or after liquid fuel injection. In all approaches, gaseous fuel does not auto-ignite on its own via compression ignition, but usually burns with the assistance of the injected liquid-fuelled ignition processes [Karim (18)]. In current work, fumigation of hydrogen into intake port of a heavy duty diesel engine was applied, allowing a premixed dual-fuel combustion. The progress of conventional dual-fuel combustion (with diesel injection at near TDC), is depicted in Figure 2.15.

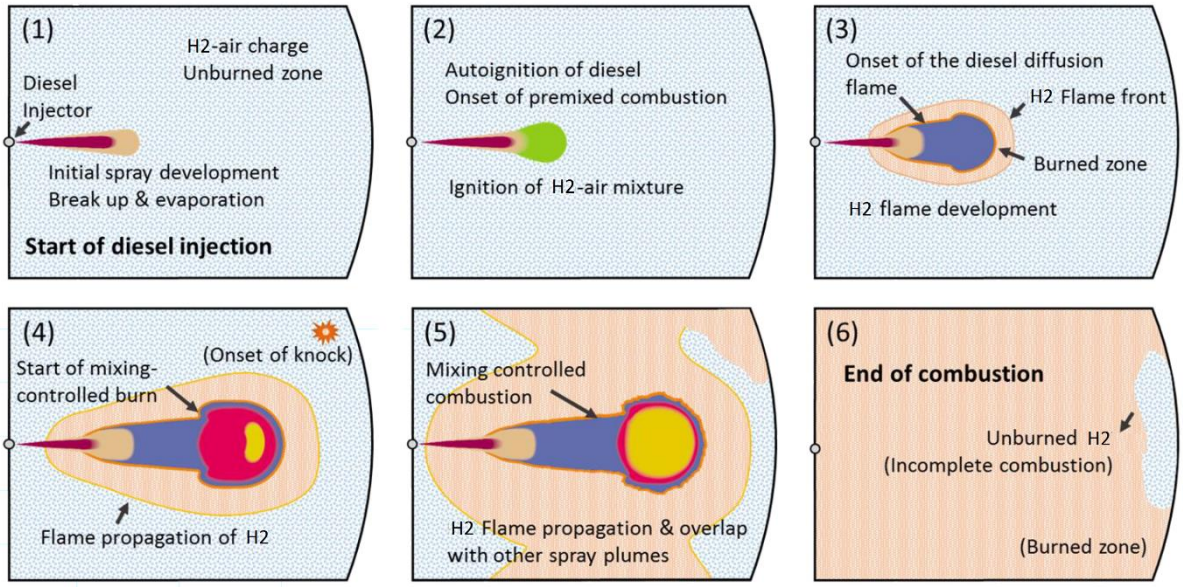


Figure 2.15: Progress of conventional H2-diesel dual-fuel combustion

The complicated interaction of liquid fuel spray and bulk premixed gaseous fuel - air is not only thermal but has chemical kinetic feature which tends to extend the ignition delay and emissions. Thus, very precise control on timing of both fuel gas introduction and liquid fuel injection is essential [Karim (18)].

Fuel type and concentration (in air) are important factors in premixed combustion as these parameters control chemical reaction rates. However, local flame velocity is affected heavily by mass and heat transfer. It is worthwhile to note that extra fuel or oxidant are

needed for initiating burn process in partially premixed regions. These instances present complicated interaction among many chemical and physical reactions which are expressed on burn process in ICEs generally and in dual-fuel engines specifically. Chemical processes are generally governing in conditions relatively slower than physical mixing processes such as at low temperatures. However, oxidation is altering exponentially on temperature which makes it happen more rapid than other physical processes. Sometimes for simplification, its effect on burn rate might be undermined or dismissed. Diffusion flame length requires to be regulated ensuring no extreme impingement and heat transfer would result in intolerable high temperature surfaces (Figure 2.16) [Karim (18)].

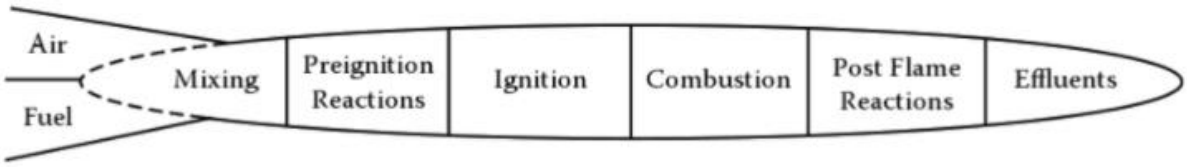


Figure 2.16: Main stages of fuel gas combustion in air [Karim (18)]

Fumigating gaseous fuel into intake air of a dual-fuel engine, makes alteration in mixture's physical and transport properties like gamma (specific heat ratio) and heat transfer features. In addition, varying partial oxygen pressure resulted from gaseous fuel displacement, affects pre-ignition activity and its associated heat release which can be altered by residual gas effects. Therefore, ignition delay trend in dual-fuel engine is distinguished from conventional diesel engine. This delay extends with higher gaseous fuel fumigation up to a specified peak and later reduces to a value (before the stoichiometric ratio of equivalent gas and liquid fuels with available air [Karim (18)].

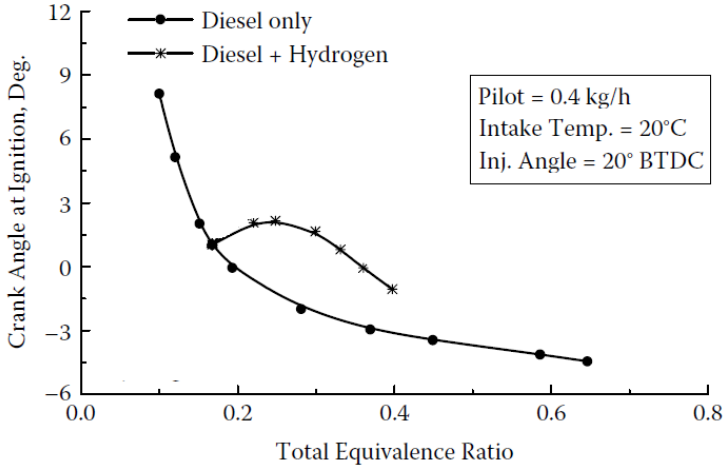


Figure 2.17: Ignition Delay vs. equivalence ratio [Karim (18)]

Some of the characteristics of dual-fuel combustion which make is more complicated than conventional SI and diesel combustion are as follow [Karim (18)]:

- The gaseous fuel has low tendency to get oxidised completely at low loads which results in higher fuel consumption, HC and CO emissions.
- Since significant pre-ignition occurs sporadically within gaseous fuel-air mixture, fast heat release and pressure rise is observed.
- The knock threshold at high loads is characterised by uncontrolled auto-ignition and very fast partial combustion subsequently.

Mixing process within CI engines is important for leading combustion process properly. For instance, injecting low-amount pilot makes ignition occur after end of injection allowing mixture of pilot injected fuel with premixed gas fuel-air. Earlier pilot injection if not too early (pre-ignition), might start lean mixture combustion permitting more time for mixing of pilot with gas fuel.

Achieving optimised combustion and performance, maximum pressure requires to be located 10-15 ATDC. Conventional dual-fuel combustion relies on diesel pilot spray and ignition properties as well as gaseous fuel type and concentration. While pre-ignition results in radicals and some products such as aldehydes and CO, their concentration is increasing during late part of compression stroke to affect subsequent combustion progress of diesel pilot [Karim (18)].

As seen in Figure 2.18, premixed dual-fuel combustion examined through heat release curve is divided to three major overlapping parts: 1) pilot combustion 2) gaseous fuel combustion in the environs of pilot combustion centres. 3) pre-ignition and resulting turbulent flame propagation within lean gas fuel-air mixture.

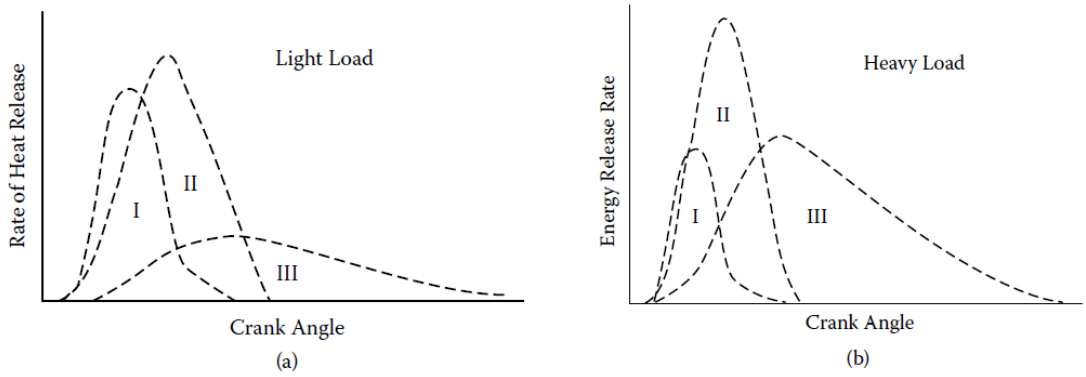


Figure 2.18: Heat release components of dual-fuel combustion (a) light load (b) heavy load [Karim (18)]

2.6 Hydrogen enrichment of diesel combustion

It is obvious that after reaching the Paris Agreement, the worldwide efforts for challenging the climate change has been made effective. Hence, a universal binding commitment for Green House Gases (GHG) reduction, particularly CO2, has been formed despite US exit of this treaty.

European Union (EU) has regulated severe laws and targets to force car manufacturers to control the exhaust emissions in their products. As commercial vehicles have been accounted for 25% of emissions of EU transport sector, the focus on their Heavy Duty (HD) engines matters seriously [EC (53)].

As heavy-duty engines benefit less from the conventional measures of passenger vehicles, alternative low carbon fuels like hydrogen become particularly attractive for reducing CO2 emissions. Although, HD diesel engines have high thermal efficiency, their high soot and NOx emissions cause serious problems. After-treatment controls such as Diesel Particulate Filter (DPF) for inhibiting soot or Selective Catalytic Reduction (SCR) for NOx reduction are expensive and of limited durability but are essential.

Effectual approaches classified in Low Temperature Combustion (LTC) category, with three specs: lower gas temperature, longer ignition delays and lower local equivalence ratios; can be proposed for curbing soot and NOx in diesel engines. Longer ignition delay allows adequate premixing, reducing in-cylinder rich regions and hindering soot formation [Reitz et al. (54)]. Nonetheless, lower combustion temperatures results in higher CO and HC emissions because of incomplete combustion. This issue may be solved by partial substitution of the diesel fuel with a low-carbon fuel like hydrogen. Indeed, lack of carbon content is beneficial within hydrogen burning in IC engines, leading to non-appearance of CO2, CO, HC and PM exhaust emissions (neglecting small levels via lubricant carbon).

As depicted in Figure 2.19, there are three pathways proposed for hydrogen supply to the IC engine [Morgan et al. (55)]:

1. Off-board water electrolysis
2. Off-board methane steam reformation
3. On-board diesel fuel reformation

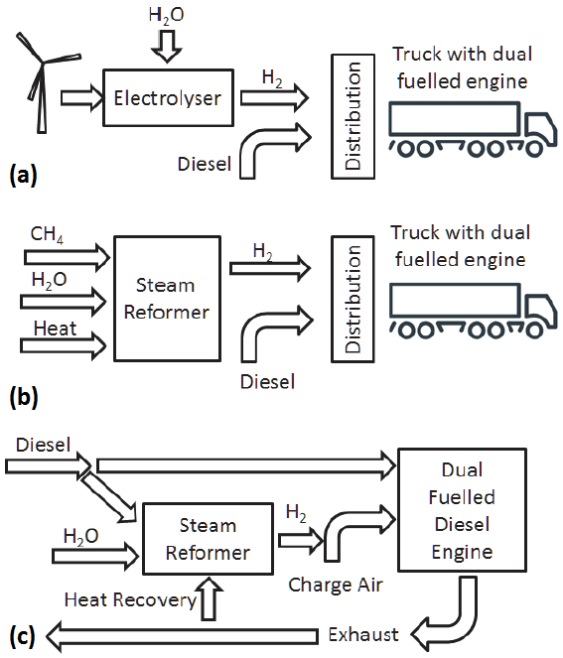


Figure 2.19: Hydrogen supply pathways: (a) off-board electrolysis (b) off-board methane steam reformation (c) on-board diesel fuel reformation [Morgan et al. (55)]

Approximately 95% of produced hydrogen is supplied from methane steam reformation which yields no overall benefit in CO2 per equivalent mass of diesel. The electrolysis method can be a zero-carbon route if the required electricity is supplied by renewable energy, but this would be very costly. Nevertheless, for both these off-board methods, the produced hydrogen should be pressurised to ease compact storage. Regarding a report by US Department of Energy [Wurster (57)], the compression work for pressurising the hydrogen from 20 bar (production pressure) up to 350 bar (storage pressure) is 0.15 kWh/kg_{H2}.

Although, basic electrolysis has 20% efficiency, the recently developed machines could achieve the efficiency of 50% to 80% [UK (58)]. Supposed the higher efficiency, 50-79 kWh electricity is required for 1 kg hydrogen production. If IC engine can burn hydrogen at same efficiency to diesel, each 1 kg diesel can be replaced with 358 g hydrogen. Considering the current UK grid emission of 0.59 kg_{CO2}/kWh [Strbac (59)], this replacement would result in emission of 12 kg of CO2. Given that the 1 kg diesel replacement with hydrogen, can only emit 3.19 kg_{CO2}, the merit of this approach is arguable unless the grid CO2 emission can be

reduced significantly. This agenda could be possible if renewable energy contribution takes more share of power generation in the future [Strbac [59)].

The third approach comprises the diesel fuel reformation on-board using the recovered exhaust energy. This energy generates superheated steam and will enhance the calorific value of the fuel by 25%. The resulting syngas which consists of 70% H2 and 30% CO and CO2, could displace a fraction of diesel fuel with 5% reduction in fuel consumption. Due to several issues engaged with direct application of hydrogen such as infrastructure, distribution and on-board storage, on-board reformation can be assumed as an interim solution.

The Table 2.3 summarises the CO2 emissions of the introduced pathways, compared to the baseline diesel fuel:

Table 2.3: CO2 emissions of various hydrogen delivery pathways [Morgan et al. (55)]

Pathway	**Assumption**	**CO2 per kg diesel equivalent**
Baseline Diesel	1 kg diesel	3.19 kg
Hydrogen (electrolysis)	80% efficient electrolysis (current UK grid)	12 kg
Hydrogen (electrolysis)	Zero-carbon electricity	0 kg
Hydrogen (reforming)	Methane feedstock	2.6 kg
Hydrogen (on-board fuel reformation)	5% improvement of overall system efficiency via waste exhaust heat recovery	2.47 kg

At the end of literature review, it is worthwhile to mention that lower flammability limit (LFL) plays as a turning point in dual-fuel combustion as the mechanism is affected depending on which side of LFL, the hydrogen concentration is. To clarify this point, a conceptual model proposed within a relevant work by [Morgan et al. (19)] including the following three modes was considered (Figure 2.20):

1. When hydrogen concentration is above its LFL, hydrogen is pre-ignited resulting in an auto-ignition like homogeneous charge compression ignition (HCCI) mode or knocking combustion type.

2. In case of lean hydrogen (below LFL), hydrogen just burns in existence of diesel diffusion flame in a mixing-controlled mode.

3. If hydrogen concentration is over the LFL and in-cylinder conditions are not providing the hydrogen burn prior to diesel fuel ignition, the premixed hydrogen - air combustion develops in laminar mode encircling the diesel diffusion flame.

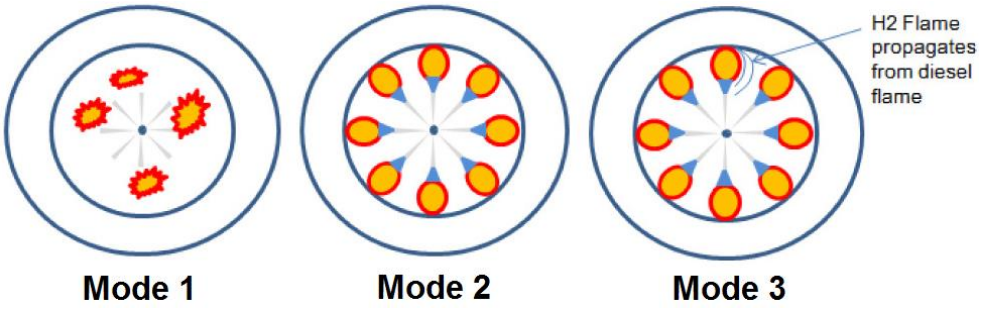


Figure 2.20: Hydrogen-diesel conceptual combustion model [Morgan et al. (19)]

2.7 Numerical modelling

2.7.1 Numerical models classification

Various models have been developed to describe the thermodynamic and fluid dynamic processes in IC engines (and associated complex interactions). In simple terms the different models can be classified by three criteria: computational cost, predictive capabilities and spatial resolution, as depicted in Figure 2.21. The main categories of numerical models in order of complexity and computational expense are as follows:

1. **Zero-dimensional thermodynamic:** based upon the first law of thermodynamics and mass conservation while neglecting (or dramatically simplifying) the conservation of momentum and spatial variation of composition and thermodynamic properties. As combustion products are a mixture of various components, the internal energy depends on the mixture composition as well as temperature. Mixture composition can be approximated by equivalence ratio (φ), hence the energy balance is solved for temperature. Consequently, the in-cylinder pressure is estimated using the ideal gas law. Despite high speed, such

thermodynamic models cannot accurately predict air/fuel mixing and emissions (with the latter often described via reduced chemical kinetic schemes).

2. **Quasi-dimensional (phenomenological):** while they are more sophisticated than thermodynamic models, the spatial discretisation of combustion chamber into multiple zones paves the way for modelling the various physical and chemical phenomena. The heat release is generally based upon turbulent burning velocity correlations, with the in-cylinder flow field defined in advance and prescribed.
3. **Multi-dimensional CFD (computational fluid dynamics):** taking turbulence into account, CFD codes compute the differential equations of mass, energy and momentum conservation on detailed meshes. Although they provide full details of mixing and combustion sub-process, they are computationally costly (especially where attempts are made to fully describe the flow field via large eddy and Direct Numerical Simulation)

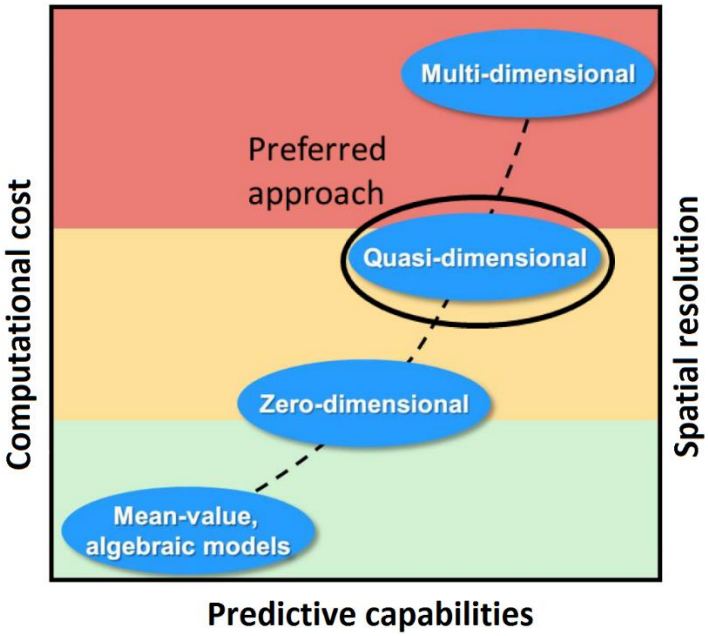


Figure 2.21: Numerical modelling classification

Specifically, thermodynamic models that only consider the first law of thermodynamics linked to simple chemical kinetic schemes cannot adequately predict the products of combustion. In addition, fuel spray and chemical reactions cannot be simulated without complex and expensive empirical input. Nevertheless, such models are commonly used in industry for extracting additional thermodynamic information from engine testing and or

prediction key performance parameters (when large data banks of historical heat release are available to estimate the variation in burning with changing engine operation). One of the most common expressions used in industry in the well-known Wiebe function [Wiebe (60)].

Nevertheless, in currently reported work, the commercial 1D gas dynamic simulation package, GT-Power (v2016) was selected to carry out the numerical modelling of H2-diesel combustion. The features of this computational program and its optimisation capability are explained in Chapter3.

2.7.2 Wiebe combustion model

Initially, the empirical Wiebe function was chosen for dual-fuel modelling. This function targets to reproduce the typical S-shaped profile of the integrated heat release rate of SI engines. The ratio of the heat released until crank angle θ to the total amount of heat released by the end of combustion can be estimated by:

$$\frac{Q_{ch}(\theta)}{Q_{ch,tot}} = 1 - exp\left[-a\left(\frac{\theta-\theta_{soc}}{\Delta\theta_c}\right)^{m+1}\right] \qquad (2.1)$$

while $Q_{ch,tot}$ (= m_{fuel} . LHV) represents the total fuel energy content, and θ_{soc} and $\Delta\theta_{soc}$ represent the start of combustion (SOC) and the combustion duration, respectively.

According to Figure 2.22, the constant **m** defines shape of the integrated heat release curve and factor **a** is derived from the perception that only a certain fraction of the injected fuel has been burned at the end of combustion (EOC). Introducing the conversion efficiency η_{conv} at the end of combustion $\theta = \theta_{eoc}$:

$$\eta_{conv} = \frac{Q_{ch}(\theta)}{Q_{ch,tot}}, \theta = \theta_{eoc} = 1 - e^{-a}$$

$$\Rightarrow \quad a = -\ln(1 - \eta_{conv}) \qquad (2.2)$$

Thus, for a typically assumed conversion efficiency of 99.9%, ***a*** becomes 6.908.

By differentiating Eq. (2.1) with respect to the crank angle, the instant heat release rate can be resulted:

$$\frac{dQ_{ch}}{d\theta} = a.Q_{ch,tot}.(m+1).\left(\frac{\theta-\theta_{soc}}{\Delta\theta_c}\right)^{m}.exp\left[-a\left(\frac{\theta-\theta_{soc}}{\Delta\theta_c}\right)^{m+1}\right] \quad (2.3)$$

In Figure 2.22, the instant and integrated heat release rates calculated by Eqs. 2.1 and 2.3, are plotted for different parameter **m** values.

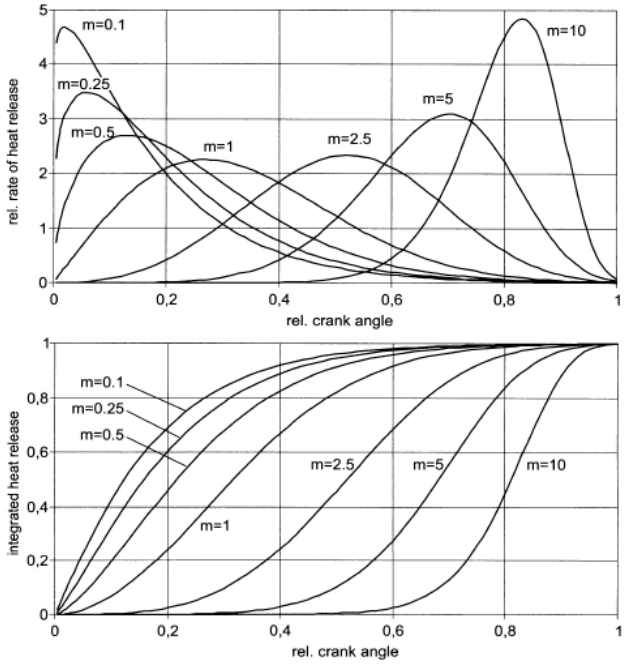


Figure 2.22: Wiebe function for various parameters [Stiesch (61)]

The reality is that such models are not predictive at all and merely prescribe the 'shape' of the heat release curve to match the user input. Although homogeneous charge SI combustion can be reproduced well by Wiebe function, the diesel combustion cannot due to its distinct premixed peak. Hence, a superposition of three normal Wiebe curves has been proposed by GT for approximating the standard single direct injection burn by modelling premixed and diffusion parts separately.

2.7.3 Phenomenological models

Thermodynamic models have insufficient capability of predicting the effects of important factors on combustion (prior measurements). Also, CFD models need detailed characteristics of the fuel spray and combustion which can be computationally expensive (or difficult in the case of simulating primary break up of a direct injected liquid fuel, for example). Hence, the phenomenological (quasi-dimensional) model as a category classified

between thermodynamic and multidimensional CFD is chosen to perform time-efficient pre-processing of HRR and emissions as the function of important engine parameters while relying on sophisticated empirical correlations obtained over a sufficiently wide set of operating conditions [Stiesch (61)].

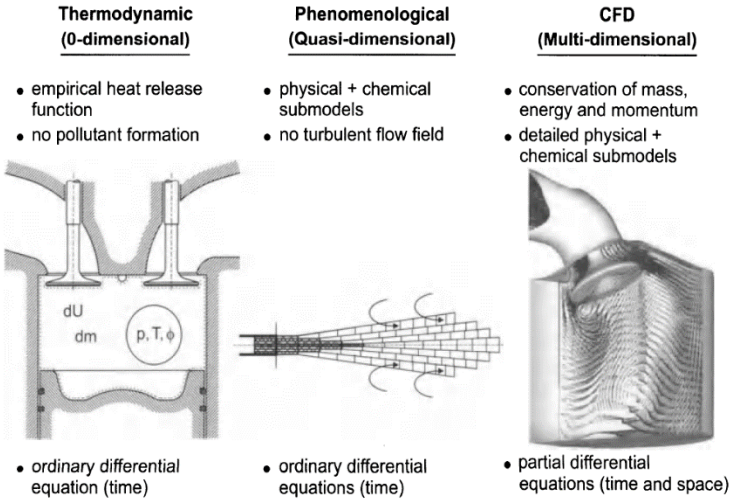


Figure 2.23: Combustion model classification [Stiesch (61)]

In the currently reported work the objective was to couple a diesel combustion phenomenological model to a turbulent premixed model to describe dual fuel combustion. Such an approach opens up numerous potential pitfalls, particularly in the event of any diesel fuel premixing. However, for 'conventional' dual fuel (where a single diesel injection is used as a form of liquid spark plug in effect) this approach was considered to be worthy of investigation, particularly in light that the commercial version of GT had recently incorporated this model for wide use. Inevitably, such an approach is still only as effective as the quality of the input and appropriateness of the empirical correlations adopted, as described in more detail below. The usual restraints remain in terms of predictions of emissions, where the simplified chemical kinetic schemes and assumptions of chemical equilibrium render the qualitative evaluation of pollutant emissions as unreliable. In the currently reported work such emissions data was recorded in the experiments, hence the main objective was to establish the sensitivities of the dual fuel model in predicting the heat release.

Among phenomenological models, the “Packet Spray” model proposed by Hiroyasu et al. [Yoshizaki et al. (62)] is well-known and has also been introduced in GT-Power entitled, “DIJet” model.

In the Hiroyasu model, fuel spray is discretised either axially or radially as illustrated in Figure 2.24. Such an approach represents the spray geometry and specified processes including fuel breakup and evaporation, air entrainment and combustion at the mercy of the resolution of the grid. Since axial parts of spray are formed equally in time, the fuel amount of each packet depends primarily on the injection rate. Conservation of mass and energy is considered for the air zone and all spray packets individually. Thus, each zone has its own T and AFR history. However, pressure is uniform and varies by time only [Yoshizaki et al. (62)].

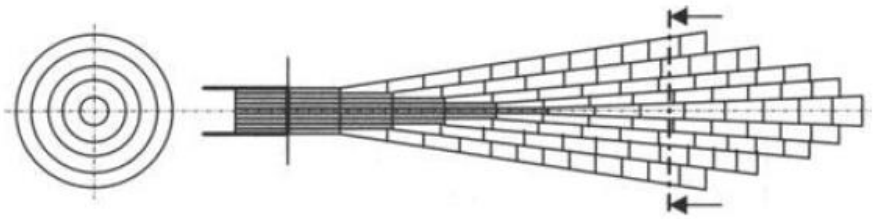


Figure 2.24: Schematic of Packet Spray model [Stiesch (61)]

Immediately after injection, there is only a liquid fuel zone. Penetrating into the cylinder, fuel atomisation starts and entrain air in order to evaporate the liquid fuel subsequently unburned vapour fuel will be formed. Air entrainment decelerates the fuel zone penetration due to momentum conservation. This issue is more severe at outer zones compared with inner zones due to quicker air entrainment, thus less distant penetration is seen in outer zones, Figure 2.24 [GT (63)].

Determined by cylinder pressure, zonal temperature and FAR, unburned zone starts to burn. Temperature of injected fuel and entrained air plus fuel evaporation effects help to specify the zonal temperature. In addition, the zonal FAR is determined from mass of fuel vapour and air within unburned zone.

Regarding Figure 2.25, there can be two possible modes of combustion within each package: evaporation-rate-controlled and air-entrainment-rate-controlled.

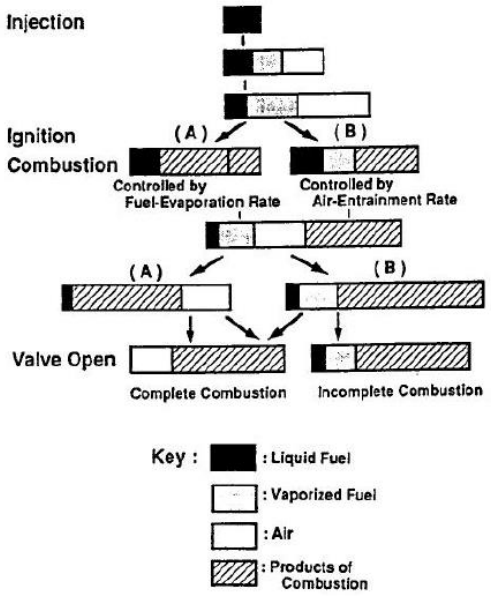


Figure 2.25: Schematic of mass system within each package [Yoshizaki (62)]

GT use proprietary equations within the DIJet model which describe specific sub-processes including: injection, time to breakup, spray tip penetration, air entrainment, droplet evaporation, ignition delay and heat release. However, these equations are based on those used in the initial model developed by Hiroyasu and his co-workers. The flowchart of the calculation process is presented in Figure 2.26:

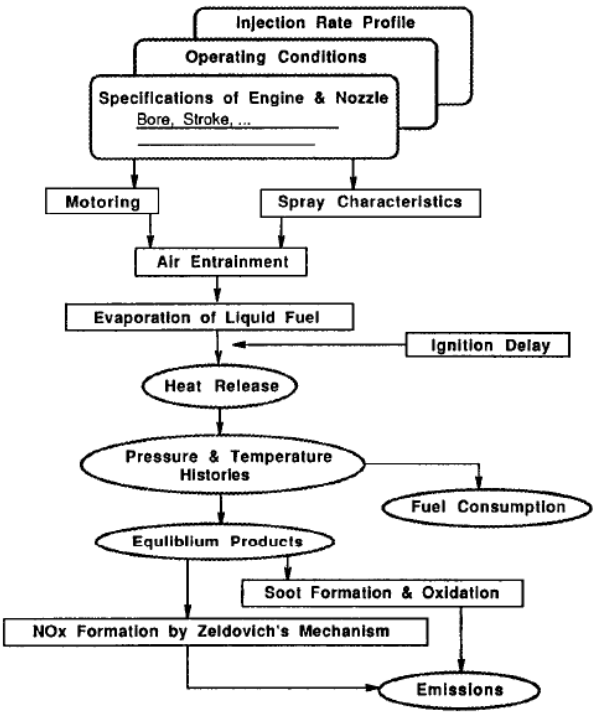


Figure 2.26: Flowchart of computations process in Packet Spray model [Yoshizaki et al. (62)]

Hiroyasu's model proves that injection rate profile has a significant impact on performance and emissions predictions done in its model and hence it can comply with emissions standards. Consequently, electronically-controlled fuel-injection system which has capable of altering injection amount, pressure, timing and rate separately can be used for emissions amelioration satisfactorily [Yoshizaki (62)].

2.7.4 A discussion on premixed combustion modelling

In spite of long term attempts and progress particularly since sixty years ago, the turbulence has remained a poorly understood concept. The reason is its unsuitability for simple mathematical analysis due to many time and length scales involved.

The combustion process in ICEs are influenced by the in-cylinder gas motion which is patterned initially by intake process and evolves during the compression stroke. The turbulent diffusion of in-cylinder flow is resulted from its local fluctuations which leads to enhancement of heat, momentum and mass transfer. Turbulence can assist on burn process acceleration by better charge mixing via wrinkling the flame front. The pockets of burned gas can be in the unburned side and vice versa, Figure 2.27. Since without turbulence, there would not be sufficient time for efficient combustion; the turbulent flow is essential for reasonable operation of the ICEs [Heywood (7)].

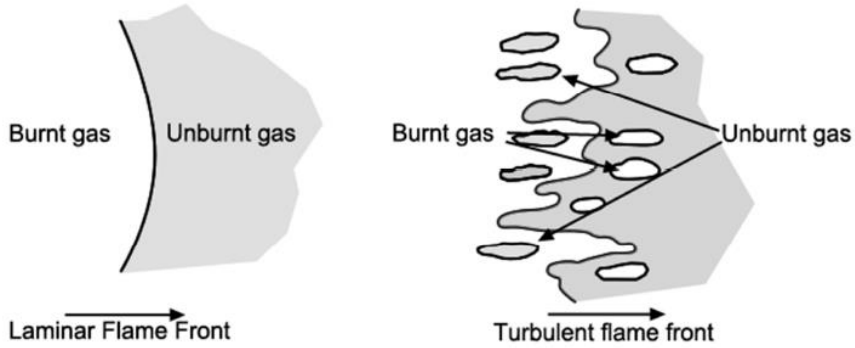


Figure 2.27: Laminar vs turbulent flame front [Stone (64)]

As turbulent flow has a random behaviour, it needs to be defined statistically. Turbulence can be introduced in form of diverse velocity and length (or time) scales. Steady local fluid speed (U) is defined as:

$$U(t) = \overline{U} + u(t) \qquad (2.4)$$

$\overline{U}$ is the mean flow velocity.

The instant velocity fluctuation, u(t) is defined by its root mean square, turbulence intensity (u'):

$$u' = \lim_{\tau \to \infty} \left[\frac{1}{\tau} \int_{t_0}^{t_0+\tau} (U^2 - \overline{U}^2) dt \right]^{1/2} \quad (2.5)$$

Although u' is known as the turbulence intensity but the correct definition is $\frac{\acute{u}}{\overline{U}}$.

The turbulence can be dimensioned via a spectrum of turbulent eddies. While the size of largest eddies are restricted by system boundaries, the smallest scales are governed by molecular diffusion. The characteristic length scales of an intake turbulent jet flow are depicted in Figure 2.28. The largest eddies which are responsible for producing the most of turbulence are scaled by the integral length scale, L as the integral of correlation coefficient of fluctuating velocity [Heywood (7)]:

$$L = \int_0^{\infty} R_x dx \text{ where } R_x = \frac{1}{N_m - 1} \sum_{i=1}^{N_m} \frac{u(x_0)u(x_0+x)}{u'(x_0)u\prime(x_0+x)} \quad (2.6)$$

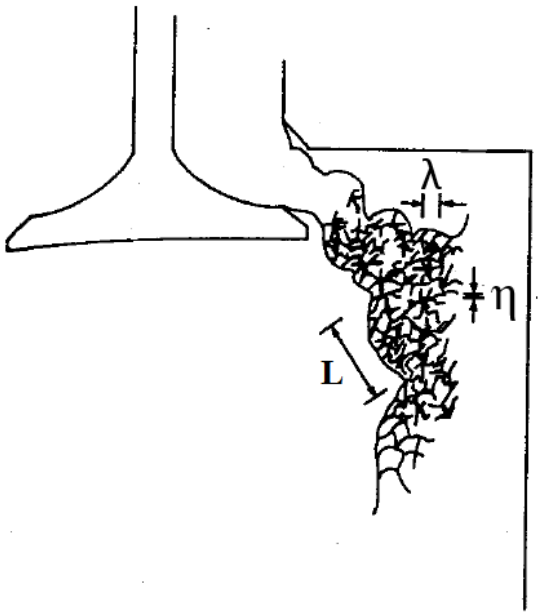


Figure 2.28: The turbulent structure of intake flow jet [Heywood (7)]

The intermediate length scale, so-called Taylor microscale relates the fluctuating strain rate to the turbulence intensity:

$$\frac{\partial u}{\partial x} \approx \frac{u\prime}{\lambda} \quad (2.7)$$

Ultimately, the smallest scale of turbulence, η, known as Kolmogorov length scale is where the turbulence dissipation occurs [Heywood (7)]. These characteristic lengths are depicted in Figure 2.29:

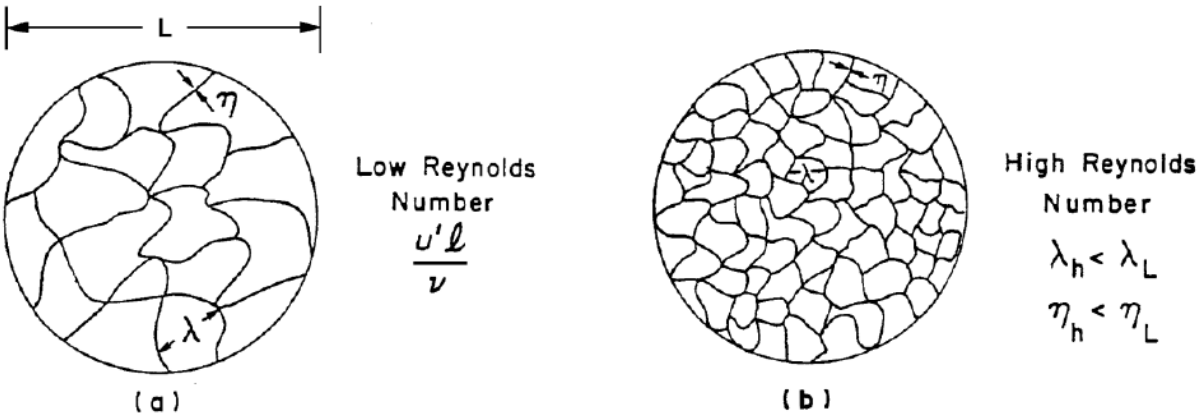


Figure 2.29: The turbulent eddy structure [Tabaczynski (65)]

The rate of transferring the unburned gas into the flame front and converting to combustion products under laminar conditions is specified by Laminar burning velocity (u_L). In laminar mode, the Taylor microscale (λ) is defined as the average distance of vortex sheets where the burn process takes place. Regarding the fact that at the beginning, the flame is in laminar mode and then through the transition process which takes the time order of τ_b, it evolves to the turbulent flame, the burning law is defined [GT (63)]:

$$\tau_b = \frac{\lambda}{u_L} \tag{2.8}$$

As the threshold velocity of combustion initiation, (unstretched) laminar burning velocity ($\mathbf{u_L}$) has a dominance over whole combustion due to persisted interaction of initial combustion and charge motion. The laminar burning velocity is calculated by empirical correlations derived from pressure rise measured within constant-volume bombs or burners. Various empirical correlations of laminar velocity ($\mathbf{u_L}$) for a stoichiometric iso-octane/air mixture compressed from 1 bar (and 298K) up to 60 bar are presented in Figure 2.30. While solid lines represent the measured data ranges, the dotted lines depict the extrapolations. Also, the dashed lines represent the possible unstable burning velocities.

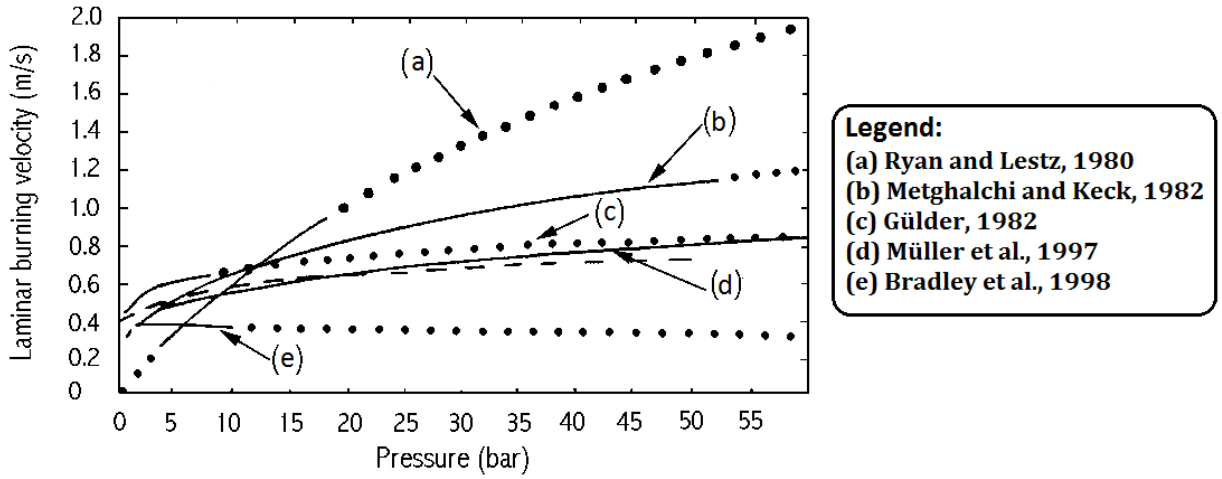


Figure 2.30: Measured (solid line) vs. extrapolated (dotted line) for u_L, stoichiometric iso-octane/air mixture compressed from 1 bar and 298K to specified pressure. (dashed line represents the possible unstable u_L) [Farr (66)]

The empirical correlations of "$\mathbf{u_L}$" by [Metghalchi and Keck (67)] is acknowledged to be the most comprehensive correlation incorporating the effects of unburned gas pressure, temperature, composition and residuals. However, the data is extrapolated up from 50 bar and also does not include the effects of flame stretch and instabilities as these measurements were taken in a constant-volume "bomb" without windows. It was found by researchers at Leeds University that stretch has harmful effect on burning velocity. Also, flame instability leads to flame cellularity and increase flame surface area and hence burning velocity and cylinder pressure.

The correlations were obtained for various hydrocarbons and methanol and those at high pressure and temperatures can be fitted in form of a power law [Heywood (7)]:

$$u_L = u_{L,o}\left(\frac{T_u}{T_o}\right)^{\alpha}\left(\frac{P}{P_o}\right)^{\beta} \qquad (2.9)$$

where To = 298 K and Po = 1 atm are the reference temperature and pressure, and $\mathbf{u_{L,o}}$, **α** and β are constants for a given fuel, equivalence ratio and burned gas diluent fraction. $\mathbf{T_u}$ is the temperature of unburned gas.

For laminar burning velocity of hydrogen, the GT solver uses a proprietary equation similar to the Eq. 2.9 with slight modification. Also, the effect of dilution is considered by multiplying by a function specified below:

$$f(Dilution) = 1 - 0.75 * C_{DE}(1 - (1 - 0.75 * C_{DE} * Dilution)^7) \qquad (2.10)$$

where the C_{DE} is the dilution effect multiplier.

As laminar burning velocity relates directly to the equivalence ratio, the lean combustion engines suffer from low flame propagation speed. Thus, it is attempted to increase the in-cylinder turbulence with aim of making up this insufficiency. As the result, the reaction zone (flame) enlarges due to wrinkliness and mass entrainment rate is ameliorated. However, partial or complete quenching might be caused by excessive turbulence.

2.8 Summary

This chapter started with a review on ideal diesel engine cycle and its different combustion phases. The properties of various alternative gaseous fuels such as NG, biogas and LNG were considered. Later, hydrogen was introduced in detail with the aim of applying in diesel engines. Some statistics of global vehicle production were followed by their emission regulations. The diesel combustion fundamentals were described including: Dec model, diffusion and premixed flame and dual-fuel combustion mode. Hydrogen enrichment pathways were explained and compared in terms of CO2 emission. Numerical modelling was classified and two models, Wiebe and Packet Spray were explained in detail. Ultimately, premixed combustion modelling was discussed with details about laminar and turbulent flames.

Chapter 3: Experimental and Numerical Methodologies

3.1 Introduction

This chapter contains the detailed description of the experimental methods for testing the effects of hydrogen enrichment in a HD diesel engine. The technical specifications of all equipment of the thermodynamic (full metal) single cylinder HD diesel engine rig along with hydrogen setup are explained. Furthermore, the data acquisition and post-processing of the acquired data is presented. At the end of this chapter, the numerical methodology of simulation program and its optimisation methods are described.

3.2 HD diesel engine specifications

The test engine was installed at Brunel University and was a boosted HD diesel single cylinder with a combustion system based upon an OEM multi-cylinder engine, namely the Yuchai "YC-6K" model. The mutli-cylinder base engine was manufactured by Guangxi Yuchai Machinery Group in China, and was similar in design to a modern Euro VI heavy duty platform (boosted common rail with EGR). The technical specifications of the test engine is presented in Table 3.1.

Table 3.1: Technical specifications of test engine

Parameter	Value
Bore	129 mm
Stroke	155 mm
Connecting rod length	256 mm
Swept volume	2.026 dm^3
Number of cylinder	1
Number of valves	4
Geometric Compression ratio	16.8 : 1
Max in-cylinder pressure	180 bar
Max brake power	~ 52 kW
Max brake torque	~ 275 Nm
Max continuous operating speed	1900 rpm
Diesel injection system	Bosch common rail, 2200 bar max injection pressure, 8 holes, 150° spray
Diesel fuel	Diesel – off-road "red" diesel (LHV = 42.9 MJ/kg)
Hydrogen fuel	BOC® CP grade hydrogen N5.0 (LHV = 120 MJ/kg)
Oxygen gas	BOC® Oxygen N2.6
Engine coolant	50% ethylene-glycol and 50% water
Engine oil	Comma TransFlow SD 15W-40

The combustion chamber had a re-entrant bowl piston which was fitted to an engine block originally designed by AVL, as shown in Figure 3.1. A 150 kW eddy current dynamometer

(Froude Hofmann® AG150) was used for absorbing the engine brake torque and hence controlling the engine load. Engine control unit (ECU) had the capability of governing engine speed by regulating the diesel flowrate at a given load.

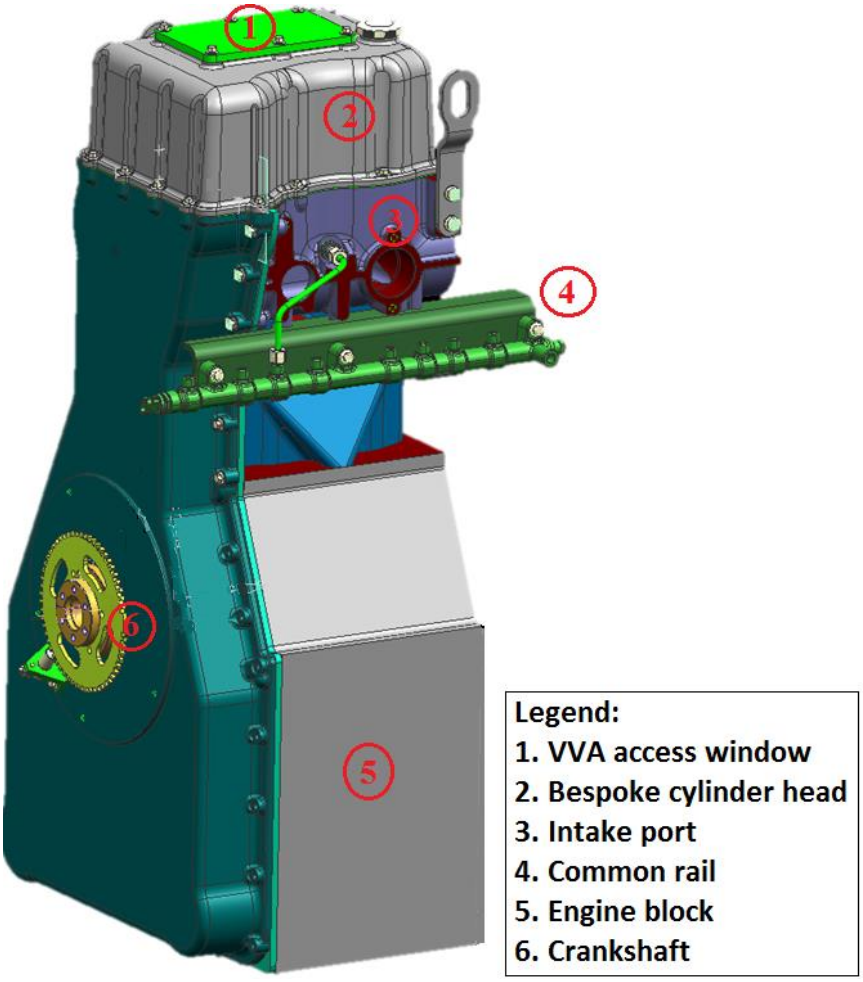


Figure 3.1: 3D design of test engine

While intake air pressure was boosted using an AVL 515 external supercharger, fine-tuning of the pressure was possible using a Bosch® intake throttle valve. The Endress+Hauser® (Proline t-mass 65F) was measuring the intake air flowrate. A 24 litre intake plenum located downstream of intake throttle and a 54 litre exhaust plenum located upstream of EGR circuit were used for damping the pressure fluctuations. An electrical backpressure valve (Foude Consine®) located downstream of exhaust plenum, allowed exhaust gas recirculation (EGR) in association with the EGR valve. The schematic of intake and exhaust system is depicted in Figure 3.2. Several water-cooled heat exchangers allowed

temperature controlling of oil, coolant, intake air and external EGR. The technical specifications of all measurement devices is presented in Appendix A.

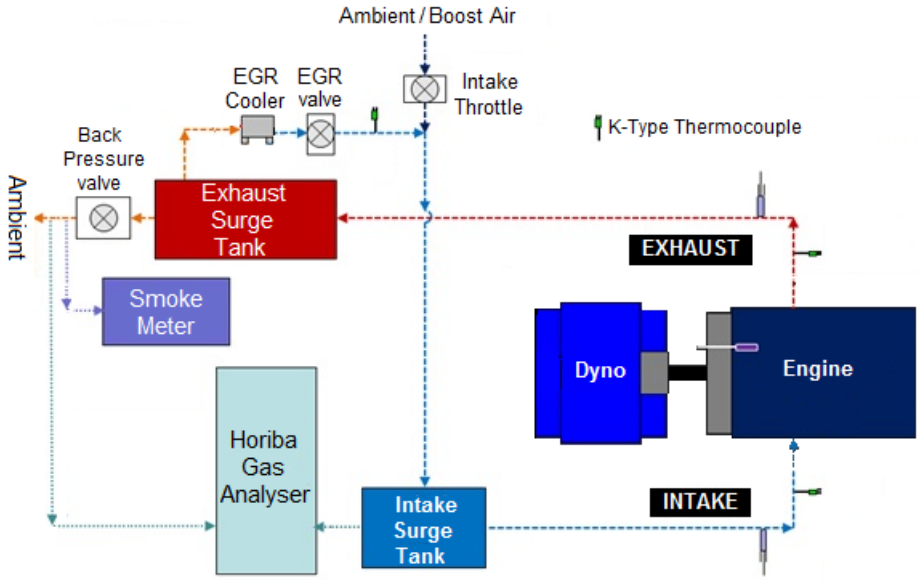


Figure 3.2: Schematic of intake and exhaust system

3.3 Diesel fuel injection unit and its injector calibration

The diesel fuel was delivered to the cylinder using the Bosch® common-rail high pressure injection unit. This unit was controlled by a dedicated CR.8 ECU (supplied by the ECE GmbH) via CAN interface. The mass flow rate of diesel fuel ($\dot{m}_{diesel}$) was specified via measuring the supply and return flow rates by two Endress+Hauser® (Promass 83A Coriolis) flow meters. The components of the diesel fuel system is depicted in Figure 3.3.

Injector actuator is the significant element of common-rail system which generally has two main types: solenoid and piezo. In a Solenoid, the applied current is proportional of derived force but this force is a non-linear function of actuator position (air-gap size). Therefore, the control of position and velocity in a solenoid is not simple and they are assumed as a shut/open valve. Otherwise, a piezo actuator's voltage is proportional to the derived force which has linear relationship with displacement. Thus, although piezo is more expensive and sophisticated than solenoid, it has more controllability [Zhao (52)].

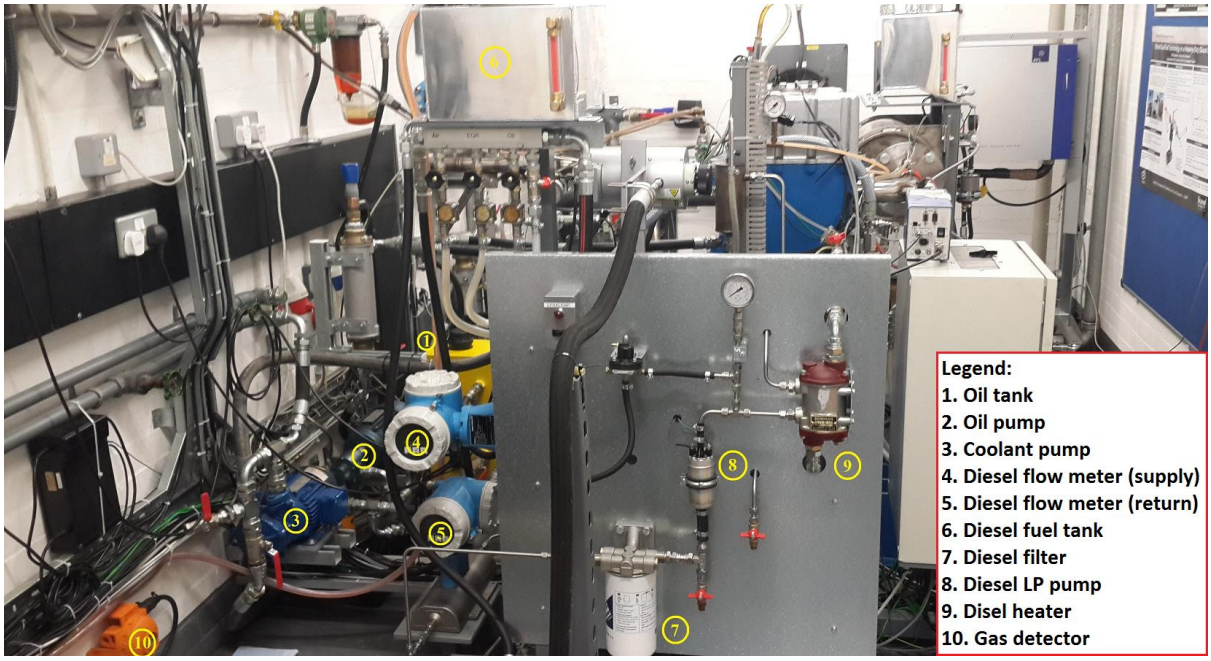


Figure 3.3: Components of diesel fuel system

The injector unit used in currently reported work was piezo-actuated. The advanced characteristics of this fuel injection unit was enabling multi injections per cycle paving the way for combustion noise control and performance improvement. It also allows flexible injection pressure and timing regardless of engine speed. The technical specifications of the diesel injector are presented at Table 3.2:

Table 3.2: Technical specifications of diesel injector

Parameter	Value
Injector	Bosch CRIN3-22 piezo-actuated
Type	Solenoid, semi-sac hole (1×1), ks
Number of holes	8
Hole diameter	176 µm
Spray angle	150 deg
Operating rail pressure	250 - 2200 bar
Static flow rate	1600 cc/min at 100 bar

In a detailed series of experiments undertaken by a prior Brunel PhD student, Ian May [May (13)], the exact amount of fuel injected and the injector delay were measured for various energizing times and rail pressures. The injector delay needs to be determined in order to specify the exact timing of injection.

With aim of minimising the hardware errors, the same fuel system arrangements of the experimental test was set up for the injector calibration procedure which was based on Zeuch's method, Figure 3.4. Following fuel injection into a constant-volume chamber which has been already filled with fuel, the inner pressure would rise in proportion of injected fuel volume [Ishikawa et al. (68)]:

$$\Delta P = k\frac{\Delta V}{V} \tag{3.1}$$

Thus, the fuel injection rate can be determined by differentiating the Equation (3.1) with respect to time (t):

$$\frac{dP}{dt} = \frac{k}{V} \times \frac{dV}{dt} \tag{3.2}$$

where:

ΔP is pressure rise measured by transducer.

V = volume of chamber (constant of 58 cm^3).

k is bulk modulus of fuel which varies linearly with pressure.

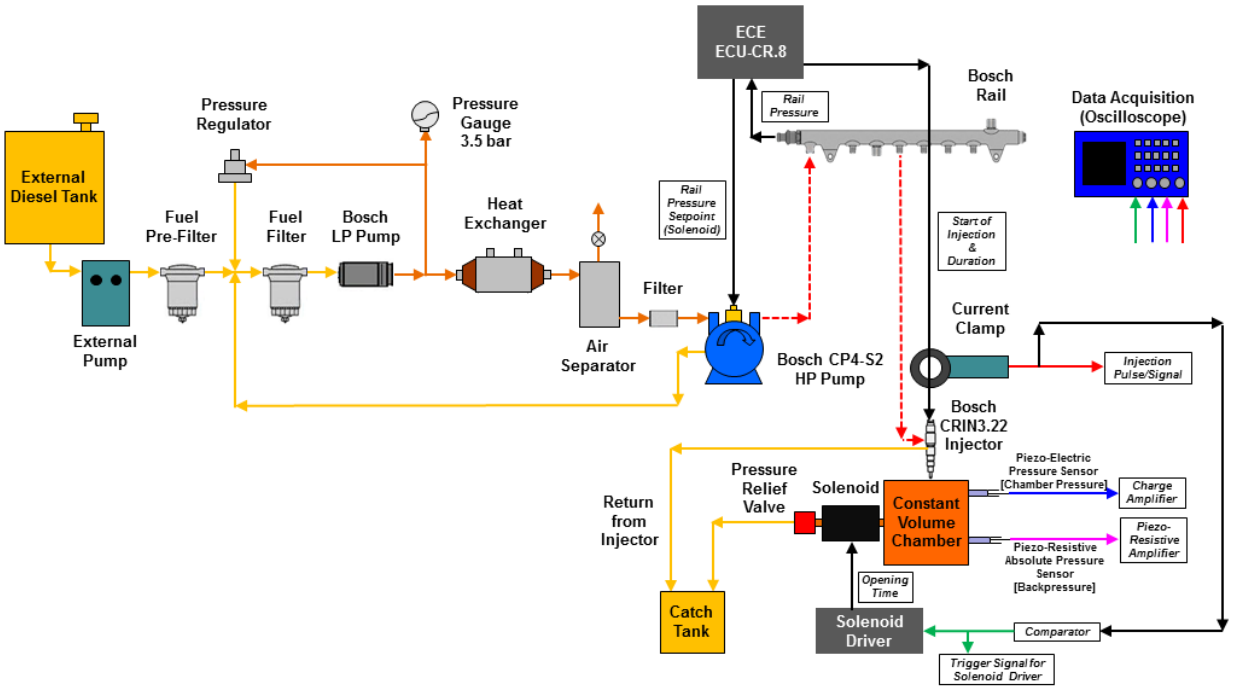


Figure 3.4: Schematic of Zeuch's method [May (13)]

Zeuch's method has the following features:

- Only a single injection event including starting and ending pressure in constant volume chamber is recorded.

- Injection rate can be calculated from change in pressure/time and then be integrated to get fuel mass injected.
- Bulk modulus of diesel fuel is considered.
- Energizing time of diesel solenoid (piezo electric) injector was measured.

After successful calibration process of injection unit, the findings are as follow:

- Necessary fuel pressures and energizing times have been tested to characterize the injector.
- The injection delay for the injector solenoid has been quantified, so precise SOI can be determined.
- Effect of pilot injection on amount of fuel delivered in the main injection was determined.
- Limits of dwell time were explored and limitation has been applied during engine mapping (effects up to 2000 µs, or 14.4 CAD at 1200 RPM).
- The interactions between pilot and main injection were preliminarily understood and it was found out that diesel injector calibration for fuelling amounts is not completely reliable.

3.4 Hydrogen and oxygen enrichment setup

The motivation for currently reported work was developing an on-demand electro hydrogen generation (EHG) machine for the automotive industry. This machine was invented originally at the Frumkin Institute in Russia and its first three generations were patented in that country. Brought to United Kingdom by a UK Trade Investment team, the 4th generation known as “EHG4-M” was built under the auspices of Prof. Keith Scott at Newcastle University and was tested extensively at the Intertek-Tickford [VNA (69)].

This machine produces hydrogen from an electrolyte and water mixture using a combination of centrifugal electrolytic and magnetic forces. The resultant hydrogen and oxygen can be used in conjunction with diesel in IC engines with aim of achieving efficient combustion and reduced emissions. Therefore, the feasibility of introducing hydrogen and oxygen into a single cylinder HD diesel engine was studied by the currently reporting author during a project for an industrial partner, VN-Automotive Ltd.

One most important issue about hydrogen fumigation is safety due to hydrogen combustible properties particularly its excessive flammability range (4 – 75 Vol%) and the odourless and colourless flame. Hence, a comprehensive risk assessment was done in consultancy with supervisors, technicians and suppliers. The schematic of the hydrogen and oxygen enrichment setup is presented in Figure 3.5.

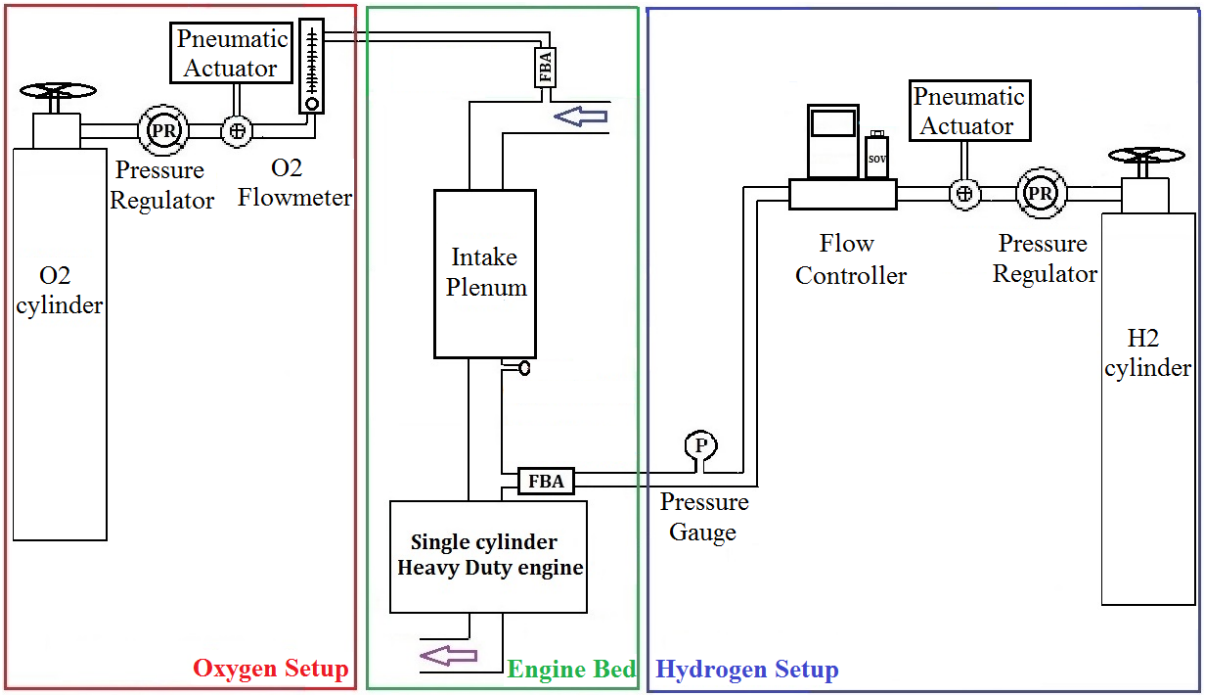


Figure 3.5: Hydrogen and oxygen fumigation setup

The first risk control measure includes embedding the gas detectors in the test cell. Two flameproof Crowcon® gas detectors of Xgard Type 5 were installed one on the ceiling and one near the engine bed. Their sensors which contain a pellistor (catalytic bead), have capability of sensing various flammable gases with particular calibration for hydrogen detection.

Lexically, a combination of “pellet” and “resistor”, the “pellistor” is made of tiny pellets which their resistance varies in presence of target gas. Since the measurement principle of detecting sensor is based on burning the detected gas, it requires to be heated gently using electrical connections. Therefore, the resistance of pellistor would vary to the target gas concentration proportionally [Pellistor (70)].

In addition, a dedicated electrochemical detector (Xgard Type 1) was mounted in the test cell for sensing oxygen gas. In case of detection exceeding the specific concentration, the gas detectors would trigger the fire alarm and shut-off the both gas flow immediately. Besides, a big fan which extracted the fuel vapours inside the cell to the outdoor resulted in reducing the flammable gas concentration and hence the probability of explosion.

As hydrogen reacts actively with oxygen, these gases must be stored far away from each other. Hence, hydrogen gas cylinder was kept in a protected cage outdoor. On other hand, oxygen gas cylinder was placed in an unoccupied cell next to the test cell. In case of gas leakage detection, an emergency button embedded at the user control room could rapidly shut off the hydrogen and oxygen supply via two solenoid actuated pneumatic valves (Figure 3.6). In addition, two flashback arrestors were appropriately mounted on the test rig to avoid any potential flame to be harmful to the equipment.

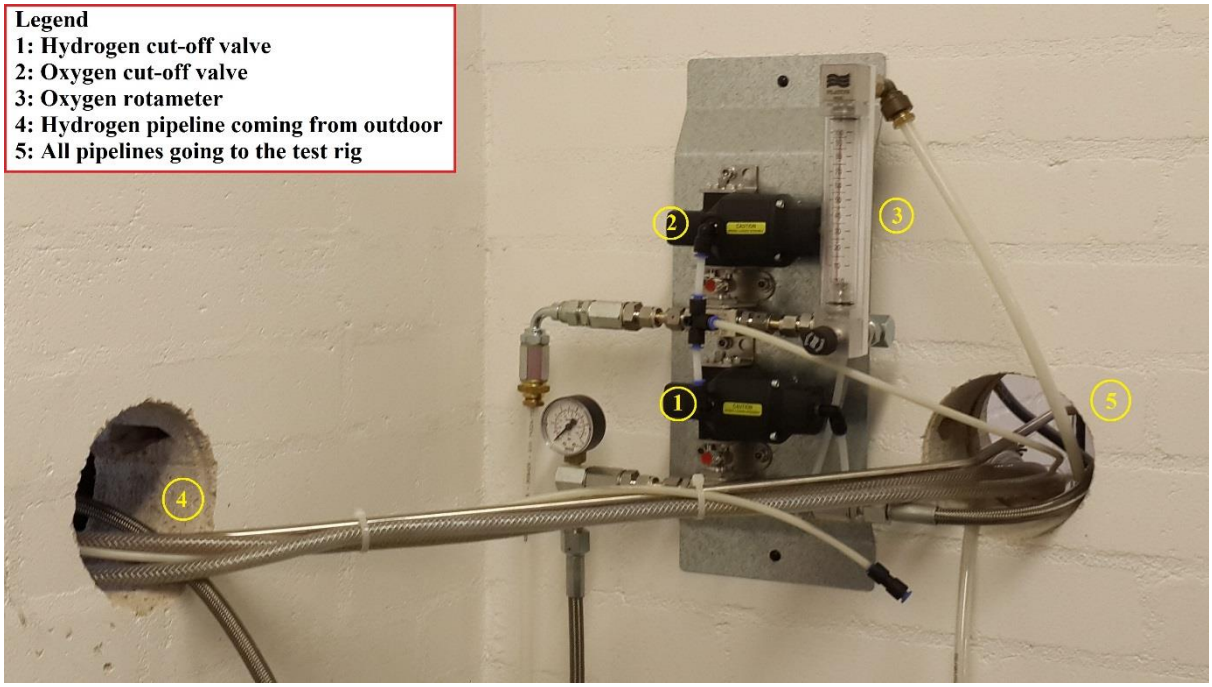


Figure 3.6: Hydrogen and oxygen supplying control panel

With the BOC® gas cylinder supplying gas at 200 bar, the hydrogen pressure was regulated down to 7 bar gauge. The required hydrogen mass was controlled using an OMEGA® mass flow controller before being fumigated into the intake port (downstream of the intake plenum).

The gas stream entering the OMEGA® mass flow transducer is split by shunting a small portion of the flow through a capillary stainless steel sensor tube while the remaining gas flows through the primary flow conduit. The geometry of the primary conduit and the sensor tube are designed to ensure laminar flow in each branch. This makes the flow rates of these conduits relevant to each other. Indeed, based on the principles of fluid dynamics, flow rate measured in the sensor tube is directly proportional to the total flow through the transducer. In order to sense the flow in the sensor tube, heat flux is introduced at two sections of the sensor tube by means of precision wound heater-sensor coils. Heat is transferred through the thin wall of the sensor tube to the gas flowing inside. As gas flow takes place, heat is carried by the gas stream from the upstream coil to the downstream coil windings. Thus, the differential in the resulting temperature-dependent resistance is detected electronically. The measured gradient at the sensor windings is linearly proportional to the instantaneous rate of flow taking place. Ultimately, an output signal is generated that is a function of the amount of heat carried by the gases to indicate mass-molecular based flow rates [OMEGA (71)].

The OMEGA® mass flow controller also incorporates a proportionating solenoid valve. The closed-loop control circuit of the controller continuously compares the mass flow output with the selected flow rate. Deviations from the set-point are corrected by compensating valve adjustments, thus maintaining the desired flow parameters. The set point can be controlled either locally (via a potentiometer) or remotely (via an analogue signal). The control process can be made without needing to compensate for variations in gas temperature or pressure (within stated limits) [OMEGA (71)].

Considering 3.5 bar pressure drop inside the flow controller, the ultimate hydrogen line pressure would be sufficient (approx. 3.5 bar) for fumigating at the junction with intake port. To avoid any risk of ignition at the intake manifold, hydrogen was introduced after the intake plenum (into a mixture of boosted air and cooled EGR) and at the nearest feasible point to the combustion chamber in the intake runner

In next stage, pure oxygen gas which was used for intake air enrichment, was regulated down from 200 bar of gas cylinder to 3.5bar and its flow was controlled by a RM&C®

rotameter. Oxygen supply pipe through a specific flashback arrestor was joint at the beginning of intake air pipe (too far away from hydrogen junction). The jointing points of oxygen and hydrogen pipelines to test rig is depicted in Figure 3.7.

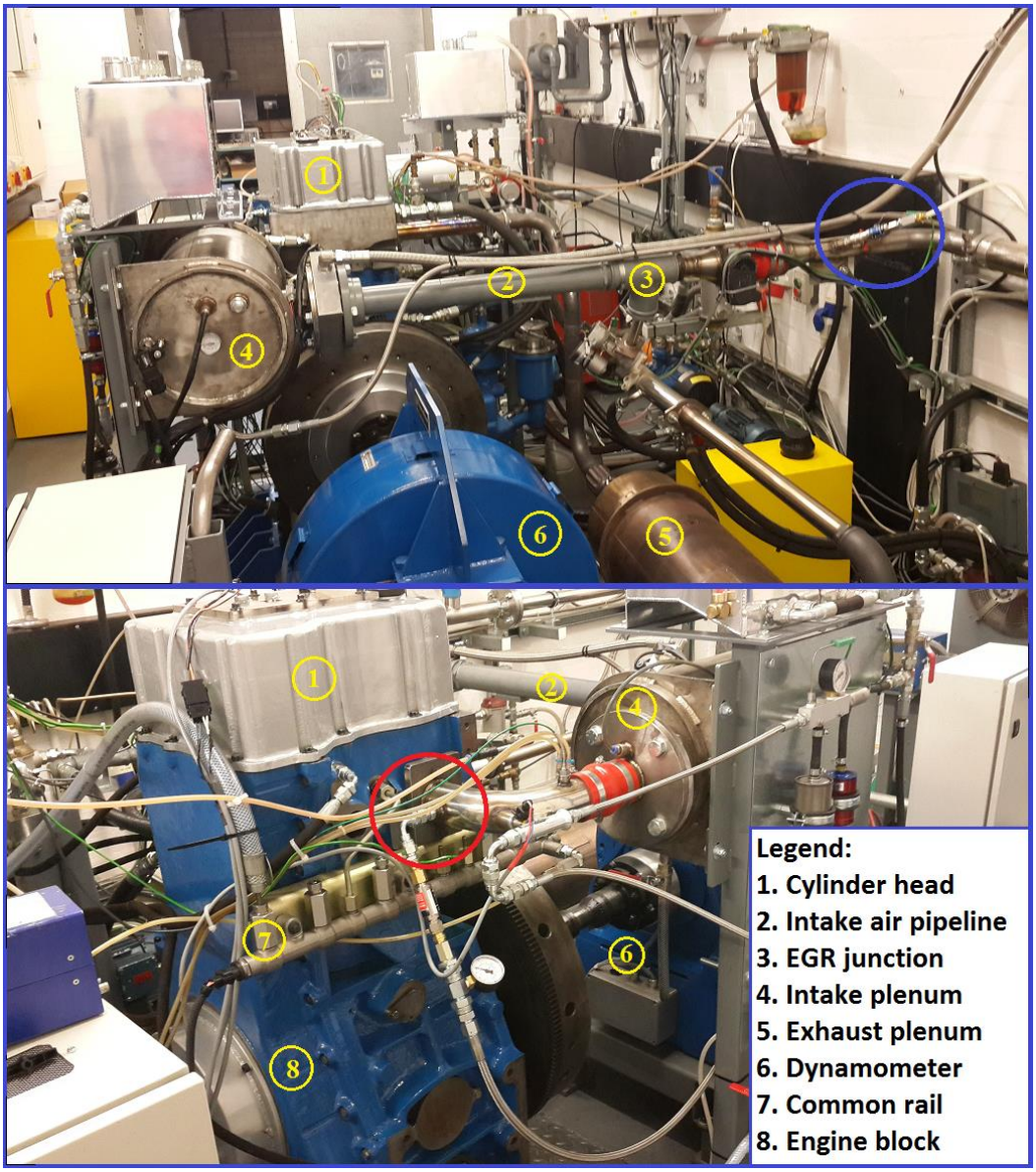


Figure 3.7: Test rig – Depicting gaseous pipelines jointing point: oxygen (blue circle), hydrogen (red circle)

3.5 Data acquisition system

3.5.1 DAQ hardware and exhaust gas analyser

An in-house combustion analyser programme named "YanTech" was developed by a previous post-doctorate at Brunel, Dr Yan Zhang [Zhang (72)], for monitoring and recording the data acquired by two National Instrument cards. Some of the instrumentation data

which were synchronised with the encoder (resolution = 0.25 CA degrees), were acquired by the high speed DAQ card (NI USB-6251). While the remaining low frequency operating signals were obtained by the low speed DAQ card (NI USB-6210). The screenshot of the combustion analyser program is presented in Figure 3.8 depicting the key factors. These factors can be classified into 4 categories:

1. Conventional settings: these are the input variables customised by the user regarding the aimed test settings. These are including: engine speed, injection and valves settings.
2. Conventional outputs: these are the ordinary outputs which consist the testing conditions such as: cylinder pressure trace, P-V diagram, heat release curve, combustion attributes.
3. Restricting outputs: these outputs are whether restricting the engine operation (Pmax and PRR) or may reduce the operational stability and repeatability of test outputs (COV_IMEPn).
4. Target outputs: these are the most important outputs which are monitored with scrutiny by the user during real-time testing. These are including engine load, indicated efficiency, emissions, etc.

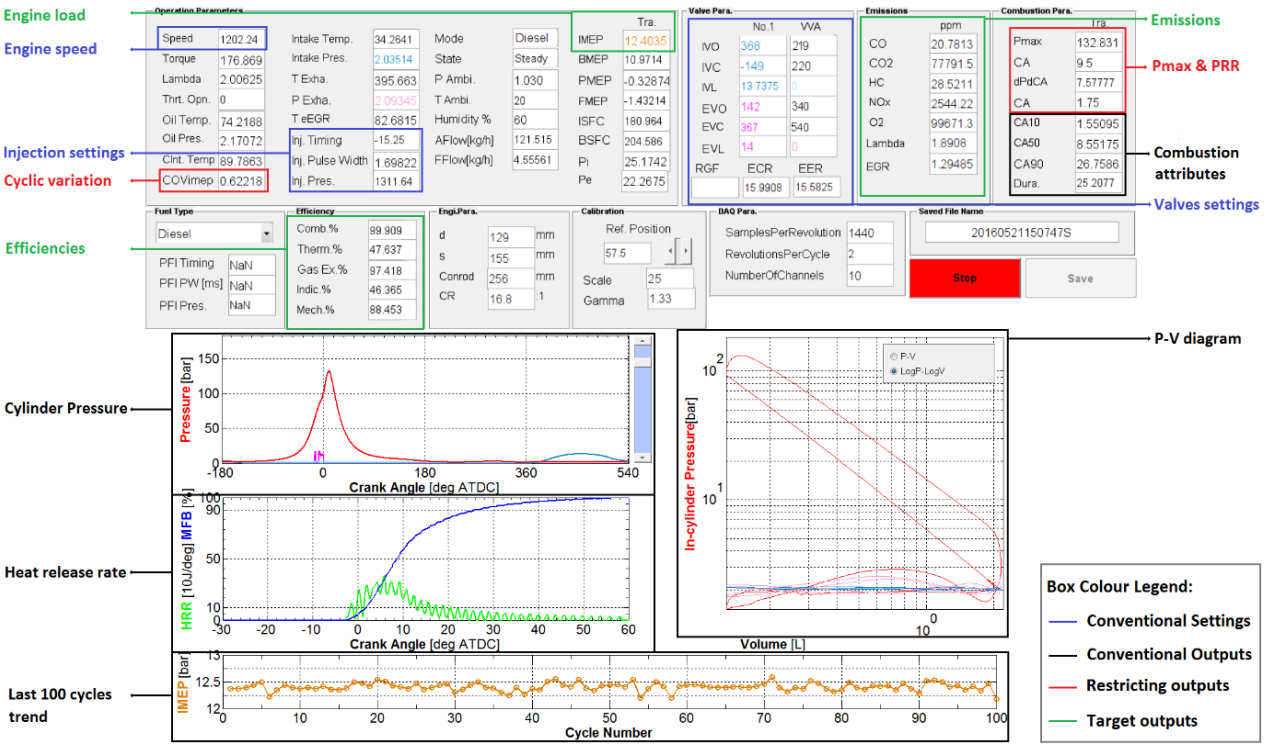


Figure 3.8: Screenshot of combustion analyser program, YanTech®

While a Kistler® piezoelectric pressure transducer sensed the in-cylinder pressure, intake and exhaust pressures were measured by piezo-resistive pressure sensors. In addition, a number of thermocouples were used to measuring the temperature at various points of the test rig. The installing location of these thermocouples are presented in Table 3.4.

Table 3.4: Installing location of thermocouples

Thermocouple label	Installing location
Coolant System #1	on inlet line at 10 mm before cylinder head
Coolant System #2	on the coolant heater (Bowman®)
Oil System #1	on the oil pressure regulator
Oil System #2	on the bottom of the Oil Balance Tank
Intake System #1	at 10 mm before cylinder head
Exhaust System #1	at 10 mm after cylinder head
EGR #1	at 10 mm after EGR valve

There was a VVA system installed on the intake camshaft developed by Jacobs Vehicle Systems. This system which is “lost-motion” based was consisting a solenoid control valve to selectively bleed oil from a HP hydraulic plenum to a LP circuit as a means for valve seating control, depicted in Figure 3.9. This solenoid valve is controlled by calibrated TTL signal sourced from an in-house MATLAB-based interface program.

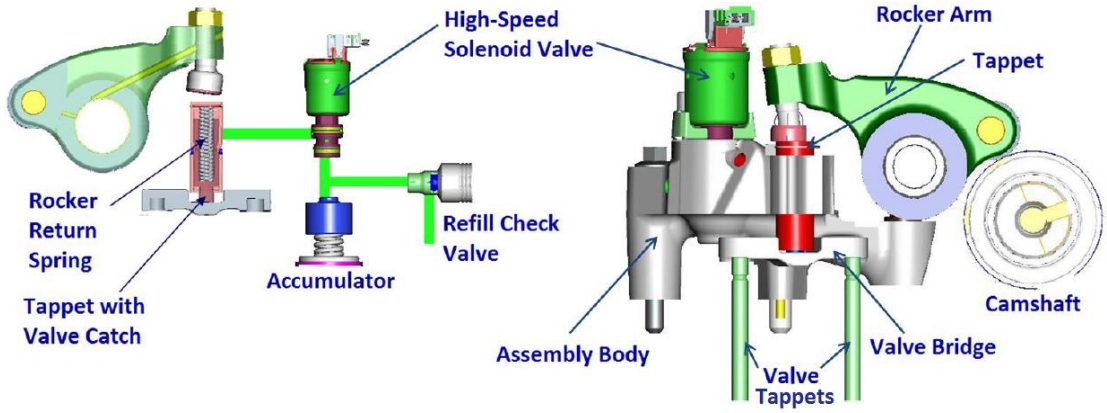


Figure 3.9: Components of VVA system [Schwoerer et al. (73)]

The maximum possible lift and duration for the intake camshaft (“Ideal Cam”) was approached 15.2 mm and 360 CAD. When the oil is free to go out while the tappet is bottomed out mechanically, the minimum valve lift is obtained (“Tappets Collapsed”). The fully collapsed tappets result in a lift approx. 60% of the maximum lift. Various conventional valve lift events can be achieved in term of duration between these two extremes by

varying the timing and amount of the oil is free to exit the tappet. As a result, LIVC could be achieved to vary global equivalence ratio (φ_{global}) and effective compression ratio (ECR) [Schwoerer et al. (73)].

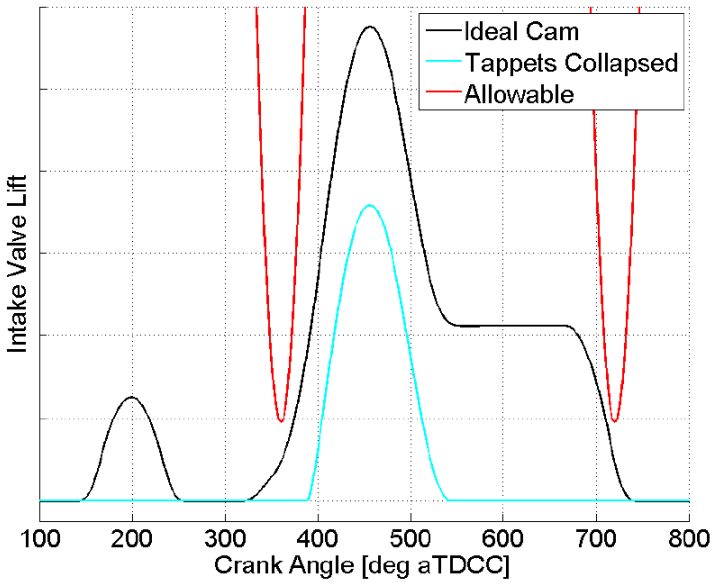


Figure 3.10: Extreme intake valve profiles [Schwoerer et al. (73)]

As variable valve actuation (VVA) control unit received the intake valve settings sent by high speed DAQ card, the intake valve lift was sensed by the S-DVRT-24 displacement sensor. Considering 4 CAD delay at 1200 rpm, the lift curve was post-processed with its start and end specified at 0.5 mm lift. Despite existing VVA system, the intake and exhaust valve lift profiles (Figure 3.11) were kept fixed during all test cases with details presented in Table 3.5.

Table 3.5: Intake and exhaust valve timings

Parameter	Value
Intake valve opening (IVO)	367 ATDC
Intake valve closure (IVC)	- 139 ATDC
Intake valve lift	13.8 mm
Exhaust valve opening (EVO)	144 ATDC
Exhaust valve closure (EVC)	360 ATDC
Exhaust valve lift	12.6 mm

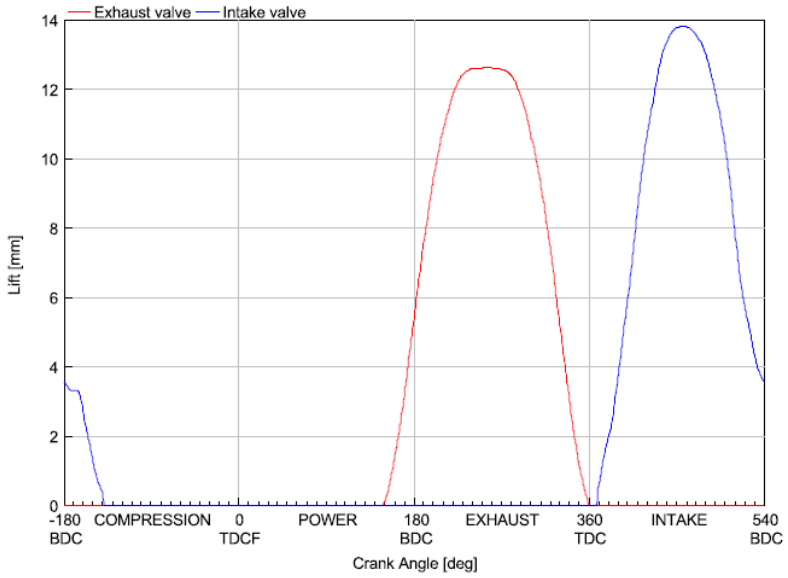


Figure 3.11: exhaust and intake valve lift profiles

The gas analyser, Horiba MEXA-7170 DEGR was utilised for measuring the exhaust gaseous emissions including: CO, CO2, NOx and HC. While the span gases was required for each gas measurement calibration (prior to the test), a branch line of the sampling line was maintained at temperature of 464K to prevent condensation. It is worthy to mention that analyser was in communication with the user PC via Ethernet ports.

Several detectors were embedded inside the gas analyser for detecting various species. A pair of AIA-722 non-dispersive infra-red (NDIR) detectors were used for measuring CO and CO2. This way, the EGR rate can be determined using equation below:

$$EGR\ (\%) = \frac{CO2_{intake} - CO2_{atm}}{CO2_{exhaust} - CO2_{atm}} \qquad (3.3)$$

CLA-720MA heated chemiluminescence detector was dedicated for NOx measurement as the sum of NO and NO2. The combination of ozone (O3) with NO-contained exhaust gases in a reactor results in excited NO2 production. After returning back to the stable state, those molecules emit light which is directly proportional to the NO concentration. As an alternative, NO2 can be converted to NO via a catalyst before being measured. The FIA-725A flame ionisation detector (FID) was used for measuring the total HC (without distinguishing between different HC species) on the wet basis.

In addition to Horiba® gas analyser, an AVL smoke meter 415SE was reading the soot emission in a 0-10 relative filter smoke number (FSN).

3.5.2 Post-processing of acquired data

The real-time post-processing of acquired data were handled in a spreadsheet with detailed equations explained in this section. The specific parameters were averaged over 200 sampled cycles.

Combustion heat release was analysed by a single-zone model based on the first law of thermodynamics during the IVC and EVO. The chemical energy released by the combustion (Qch) could undergo 4 different ways:

1. Expansion work over the piston (W)
2. The sensible energy gained by gas (U_s)
3. Heat transfer to cylinder wall (Q_{ht})
4. Enthalpy loss flowed into/out of the chamber crevices ($h_i dm_i$).

$$dQ_{ch} = dW + dU_s + dQ_{ht} + \sum h_i dm_i \quad (3.4)$$

While the heat losses to crevices and cylinder walls were combined with the chemical heat release, the combination is termed as the "net heat release" and can be calculated using ideal gas law:

$$\frac{dQ_n}{dt} = \frac{\gamma}{\gamma-1} p \frac{dV}{dt} + \frac{1}{\gamma-1} V \frac{dp}{dt} \quad (3.5)$$

Although, it is well known that the specific heat ratio ($\gamma = \frac{c_p}{c_v}$) varies with the gas temperature and equivalence ratio as will be discussed in Section 5.4.4; but it can be approximated as average value of air and exhaust gas (γ = 1.33) during the engine cycle for simplifying calculations [Zhao et al. (74)].

Cyclic variability was defined by the coefficient of variation of the net IMEP (COV_IMEPn).

The cylinder volume at any crank angle position θ was given by Eq 3.6:

$$V(\theta) = V_c + \frac{V_d}{2}\left\{\left(\frac{l}{a}\right) + 1 - cos\theta - \left[\left(\frac{l}{a}\right)^2 - sin^2\theta\right]^{1/2}\right\} \quad (3.6)$$

Subsequently, the ratio of integrated heat release from SOC until a given crank angle to the total of cumulative heat release will determine the mass fraction burnt (MFB). This way, the combustion timing (CA50) and combustion duration (CA10-CA90) could be specified accordingly. Furthermore, the interval between start of main injection (SOI) and start of combustion (SOC) at 0.3% MFB point can be assumed as the ignition delay.

As will be explained in Chapter 5, the TPA reverse-run method was used with aim of obtaining the heat release rate (burn rate) associated with low-pass filtration. The average pressure rise rate (PRR) was limited to 20 bar/deg for our testing purposes.

Integrating the in-cylinder pressure over its instant volume (Eq 3.6) during whole cycle, returns the net indicated work:

$$W_{c,ind} = \int_{-180}^{540} pdV \tag{3.7}$$

Subsequently, the net indicated mean effective pressure (IMEPn) as the engine load index is resulted:

$$imep_{net} = \frac{W_{c,ind}}{V_d} \tag{3.8}$$

Cyclic variation can be introduced as an indicator of the flow and combustion stability in form of coefficient of variation of imep_net (COV_IMEPn) over the N=200 sampled cycles:

$$COV_{impe_net} = \left[\sqrt{\frac{\sum_{i=1}^{N} \left(imep_{net_i} - imep_{net_{average}} \right)^2}{N-1}} / imep_net_{average} \right] \times 100 \tag{3.9}$$

The COV_IMEPn was limited to 5% for testing purposes, in line with typical industry limits.

The work loss required for inhaling and exhausting the charge (gas exchange) is known as pumping mean effective pressure (PMEP):

$$PMEP = \frac{\int_{180}^{540} pdV}{V_d} \tag{3.10}$$

The Eq. 3.9 results in a specific efficiency considering the pumping work loss known as the gas exchange efficiency:

$$\eta_g = \left[\frac{imep_net}{imep_net-PMEP}\right] \times 100 \quad (3.11)$$

Ultimately, the specific exhaust gas emissions and combustion efficiency (η_c) were calculated using the calculations defined in [UN/ECE (75)] with wet basis correction.

3.6 Numerical methodology

GT-Power as a user-friendly and powerful engine simulation tool is used by many engine manufacturers and research centres. Based on one-dimensional fluid dynamics, flow and heat transfer are represented in all flow components of an engine unit. GT-Power is an object-oriented graphical user interface with robust modelling capabilities. This has minimised the input data amount since only specific geometrical elements are required. Hence, this commercial package was utilised for processing our numerical modelling of dual-fuel combustion using its phenomenological models.

The following assumptions are common for all of GT phenomenological models:

- The behaviour of all gases are assumed similar to that of the ideal gas.
- In whole engine cycle excluding the combustion process (IVC to EVO), the content of cylinder is assumed as a lump single-zone which is homogenously mixed.
- The heat transfer between burned and unburned zones is neglected.
- Cylinder pressure is assumed uniform ($P_u = P_b = P_{cyl}$).
- Each zone has homogeneous temperature and chemical composition.
- The unburned zone composition is frozen and the composition of burned zone is kept in chemical equilibrium.

After running the model in GT-Power, the post-processing tool, GT-Post, is used for viewing and manipulating its output results. Engine performance plots such as power, torque, ISFC, etc. can be produced in terms of various parameters in each operating case.

3.6.1 Flow computations in GT-Power

This section describes the method of flow solution used in pipes and flow-splits. GT-Power solves the 1D Navier-Stokes equations including conservation of continuity, momentum and energy in all sub-volumes. While there are two methods of time integration which each

affect the solution variables and time step limitations, the explicit method is more recommended for GT-Power simulations. This is due to more accurate predictions of pressure pulsations within air flows and fuel injection systems.

Since the flow system is discretised into many volumes, each flow-split and pipe is represented by one or more volumes connected by boundaries. While scalar variables (pressure, temperature, density, internal energy, etc.) are uniformly assumed in centroid, the vector variables (mass flowrate, velocity, etc.) are calculated at boundaries. This discretisation is known as “staggered grid”, Figure 3.12.

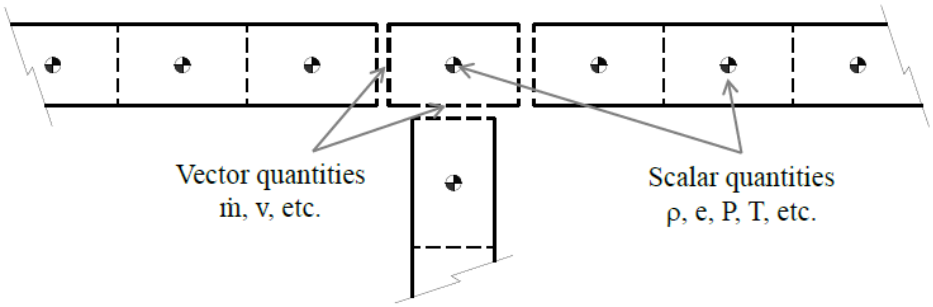


Figure 3.12: Schematic of staggered grid approach: scalars calculated at centroid, vector quantities at boundaries [GT (76)]

The primary solution variables of the explicit method are: mass flowrate, density and internal energy. The pressure and temperature at each time step, are calculated in the following way [GT (76)]:

1) Continuity and energy equations yield the mass and energy in the volume.

2) With the volume and mass known, the density is calculated yielding density and energy.

3) The equations of state for each species define density and energy as a function of pressure and temperature. The solver will iterate on pressure and temperature until they satisfy the density and energy already calculated for this time step. The species chemical change and the mass transfer between species is also accounted for during this iteration.

The conservation equations are presented below where the left hand side represents the derivatives of the primary variable [GT (76)]:

Continuity: $\frac{dm}{dt} = \sum_{boundaries} \dot{m}$ (3.12)

Energy: $\frac{d(me)}{dt} = -p\frac{dV}{dt} + \sum_{boundries}(\dot{m}H) - hA_s(T_{fluid} - T_{wall})$ (3.13)

Momentum: $\frac{d\dot{m}}{dt} = \frac{dpA + \sum_{boundaries}(\dot{m}u) - 4C_f\frac{\rho u|u|dxA}{2\quad D} - K_p\left(\frac{1}{2}\rho u|u|\right)A}{dx}$ (3.14)

$\dot{m}$ = boundary mass flux into volume, $\dot{m} = \rho uA$ m = mass of the volume

V = volume p = pressure

ρ = density A = cross-sectional flow area

A_s = heat transfer surface area e = total specific internal energy

H = total specific enthalpy, $H = e + \frac{P}{\rho}$ h = heat transfer coefficient

T_{fluid} = fluid temperature T_{wall} = wall temperature

U = velocity at the boundary C_f = fanning friction factor

K_p = pressure loss coefficient D = equivalent diameter

dx = discretisation length dp = pressure differential acting across dx

3.6.2 In-cylinder flow and heat transfer modelling in GT-Power

The key object of 'EngCylFlow', predicts/prescribes the in-cylinder flow velocity and turbulent intensity. The outputs of this object are required for the predictive combustion model of "SITurb" which will be explained in Chapter 6. It was attempted to use experimental data in order to help correlate the unknown turbulence variables while verifying the correlated values with relevant existing correlations of similar engine structures.

The in-cylinder chamber is divided into four main regions by this object: central core, squish, head and piston cup region. Taking into account of chamber geometry, piston motion and in/out flowrates via valves, mean axial/radial and swirl velocities are computed in each region. By following a single-zone turbulence sub-model explained in [Morel et al. (77)], the simplified turbulence kinetic energy and turbulence dissipation rate (k-ε) equations are solved. Consequently, the isotropic and homogeneous values of instantaneous mean turbulence intensity (**u'**) and turbulence length scale (**L**) are calculated which are utilised in 'SITurb' model. However, this approach is naive since the discrete

regions of isotropic and homogeneous turbulence do not exist within the combustion chamber of a modern engine. The flowchart of process followed within the "EngCylFlow" is presented in Figure 3.13.

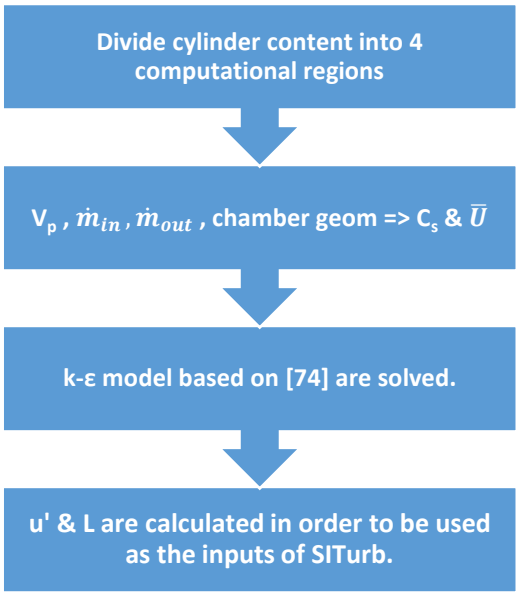


Figure 3.13: Flowchart of flow calculations within "EngCylFlow"

In GT-Power, heat transfer within cylinder and crankcase is modelled using two objects: 'EngCylHeatTr' and 'EngCylTWall*'. 'EngCylHeatTr' permits selecting the appropriate heat transfer model for calculating the in-cylinder heat transfer coefficients. The temperature of the head, piston and cylinder walls are calculated/imposed by one of three 'EngCylTWall*' objects.

Among the existing heat transfer models, "WoschniGT" is recommended since the measured swirl data is not available. This model follows the classical Woschni correlation without swirl as explained in Sec 12.4.3 of Heywood with minor modifications.

The convective heat transfer coefficient for WoschniGT model is specified as follows [GT (63)]:

$$h_c = \frac{K_1 p^{0.8} w^{0.8}}{B^{0.2} T^{K_2}} \qquad (3.15)$$

h_c = Convective heat transfer coefficient (W/m^2.K) B = Cylinder bore (m)

K_1 = 3.01426 K_2 = 0.50

p = Cylinder pressure (kPa) T = Cylinder temperature (K)

w = Average cylinder gas velocity as given below (m/s) [GT (63)]:

$$w = C_1\bar{S}_p + C_2\frac{V_d T_r}{P_r V_r}(p - p_m) \quad (3.16)$$

$\bar{S}_p$=Mean piston speed(m/s) T_r = working fluid temperature prior to combustion(K)

p = Instantaneous fluid pressure (kPa) p_m = Motoring fluid pressure at same angle as p(kPa)

p_r = working fluid pressure prior to combustion(kPa) V_d = Displaced volume (m^3)

V_r = working fluid volume prior to combustion (m^3)

$$C_1 = 2.28 + 3.9\,MIN\left(\frac{Net\ mass\ flow\ into\ cylinder\ from\ valves}{Trapped\ Mass * Engine\ Frequency}, 1\right) \quad (3.17)$$

	C_2
During cylinder gas exchange and compression	0
During combustion and expansion	3.24E-3

3.6.3 Fuel injection modelling in GT-Power

The common rail fuel injection unit of the test rig was modelled by an injection connection named 'InjMultiProfileConn' which allows for multiple pulse injection of periodic mass flow rate or pressure profiles. Since it is aimed to build a predictive combustion model for DI diesel engine, an extensive map of injection rate profiles is required.

The 'InjectionRateMap' object specifies a map of injection profiles in format of mass flowrate vs. time corresponding to different rail pressures and energizing times. This typical output of injection engineers can be provided from test bench measurement which has been collected through diesel injector calibration as described in Section 3.3.

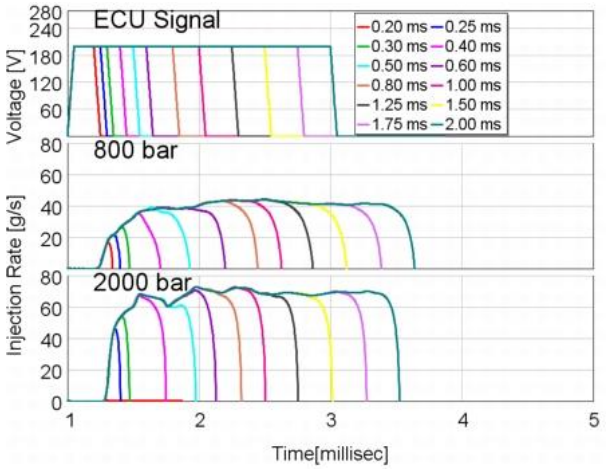


Figure 3.14: Typical injection data: injection mass flow rate vs. time for different rail pressures and electrical energizing times [GT (78)]

The total fuel injected equals the integration of each mass flowrate in terms of time which results in injected mass contour shown in Figure 3.15.a. The rail pressure and the required injected mass are imported in the 'InjMultiProfileConn' by the user. Using the injected mass contour, the injected mass is converted to an energizing time at the given rail pressure. Through an example procedure shown in Figure 3.15, the injection profile is interpolated from the profiles in the 'InjectionRateMap' object. In this example the rail pressure and injected mass in the 'InjMultiProfileConn' have been set to 1000 bar and 70 mg, respectively. This injected mass is achieved with an energizing time of ~1.3 ms at 1000 bar.

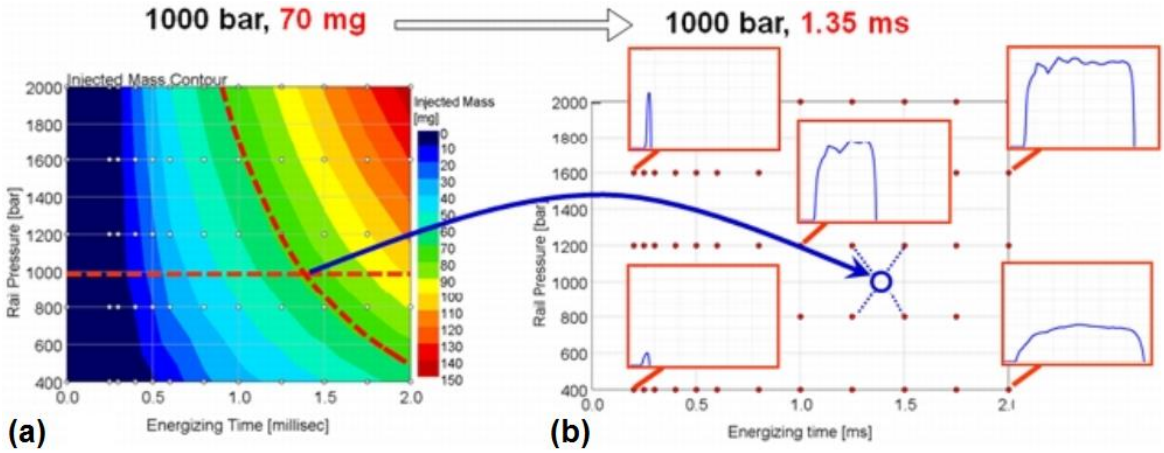


Figure 3.15: a) Injected mass contour b) Map of injection profiles [GT (78)]

In Figure 3.16, the injected mass contour of test engine produced by the 'InjectionRateMap' is shown. This contour is required for calibrating the predictive diesel combustion model, 'DIPulse'.

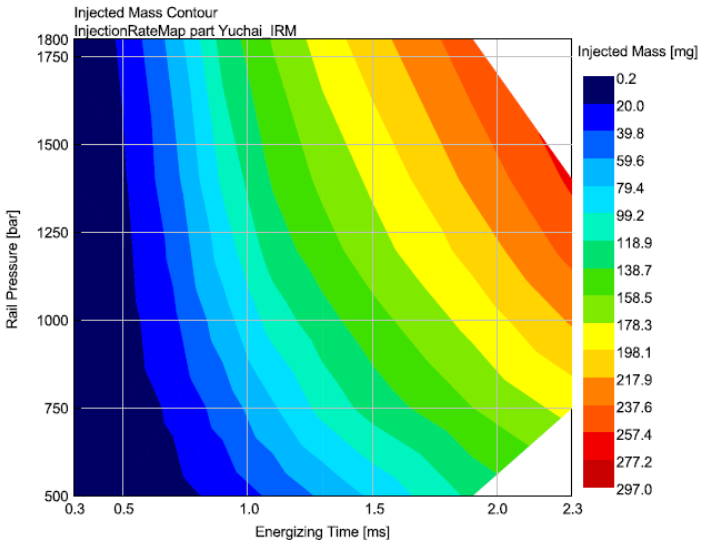


Figure 3.16: Injection rate map for the test engine

3.6.4 Combustion processing in GT-Power

This section explains in particular about the two-zone combustion which applies to all GT-POWER combustion models except for the predictive diesel model, 'DIPulse' which will be detailed in Chapter 5.

The two-zone combustion occurs in the following manner [GT (63)]:

1. Initially, the cylinder content is divided into two zones of unburned and burned zone.
2. Considering chemical equilibrium for all atoms of C, H, O, N, S and Ar existing in the burned zone, the concentrations of combustion products (13 species) are obtained. The concentrations depend mostly on the burned zone temperature and to a lesser degree, the pressure.
3. Once the new composition of the burned zone has been obtained, the internal energy of each species is calculated and summed to give energy of the whole burned zone. Applying the principle that energy is conserved, the new unburned and burned zone temperatures and cylinder pressure are obtained.

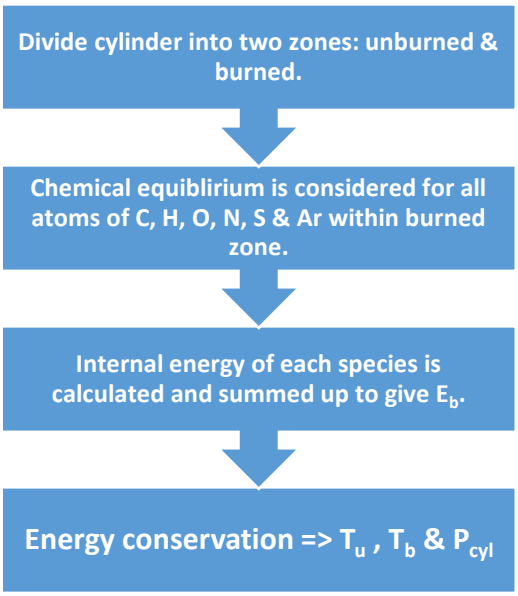


Figure 3.17: Flowchart of combustion process

The following energy equations are solved in each time step of combustion model [GT (63)]:

Unburned zone:

$$\frac{d(m_u e_u)}{dt} = -p\frac{dV_u}{dt} - Q_u + \left(\frac{dm_f}{dt}h_f + \frac{dm_a}{dt}h_a\right) + \frac{dm_{f,i}}{dt}h_{f,i} \qquad (3.18)$$

Where:

m_u = unburned zone mass

m_f = fuel mass

m_a = air mass

$m_{f,I}$ = injected fuel mass

e_u = unburned zone energy

p = cylinder pressure

V_u = unburned zone volume

Q_u = unburned zone heat transfer rate

h_f = enthalpy of fuel mass

h_a = enthalpy of air mass

$h_{f,I}$ = enthalpy of injected fuel mass

Burned zone:

$$\frac{d(m_b e_b)}{dt} = -p\frac{dV_b}{dt} - Q_b - \left(\frac{dm_f}{dt}h_f + \frac{dm_a}{dt}h_a\right) \quad (3.19)$$

where subscript "b" denotes burned zone.

The four terms of the right hand of unburned zone equation, handle pressure work, heat transfer, combustion and enthalpy addition of injected mass, respectively. The third term (combustion) contains the instantaneous rate of fuel consumption or burn rate $\left(\frac{dm_f}{dt}\right)$.

3.6.5 Three Pressure Analysis (TPA)

This section introduces the methodology of a reverse-run known as "Three Pressure Analysis" (TPA) method for exploiting trapped in-cylinder condition and burn rate calculation. Regarding its name, this approach requires three measured pressures as inputs: in-cylinder, intake and exhaust. Thus, the corresponding engine model included valves and ports connected to a single cylinder crank case with all three required pressure curves (vs. CAD) fed into it.

TPA approach is a multi-cycle simulation. For Cycle 1, a mock burn rate is used with no pressure analysis. In next cycles, the forward-run will calculate the burn rate (Eq. (3.18)) using the trapped conditions at IVC and measured pressure profile at the start of each cycle. The injection profile and the heat transfer rate are imported from the previous cycle results. The burn rate will be iterated until the calculated cylinder pressure matches the measured cylinder pressure.

The main benefit of TPA is prediction of all of the cylinder trapped quantities particularly the residual fraction. Another benefit is providing the burn rate input data consistency

check, as there is always some amount of error in calculation of burn rate from cylinder pressure. In addition to the measurement errors of cylinder pressure and other measured quantities (used as inputs), there are sort of inaccuracies and/or assumptions in the model used to calculate the burn rate (i.e. in-cylinder heat transfer). All of these potential errors which can count up to 12 types, add to a single "cumulative error" which results in mismatching of the predicted burned fuel with total in-cylinder fuel mass. With aim of handling this problem, GT-POWER adjusts the fuel energy content (LHV) until the available fuel is consumed right at the end of the predicted burn rate. The amount of this fuel energy adjustment which is reported as “fuel energy (LHV) multiplier”, indicates the amount (and direction) of the cumulative error. This multiplier is provided as an analytical tool, not a solution for a mismatched cylinder pressure. The acceptable value for adjusting LHV multiplier is 1±0.05 which had been abided for all cases.

Furthermore, due to fluctuations seen over measured cylinder pressure trace known as “ringing”, the extracted burn rate was distorted extremely. This distortion was remedied by low-pass filtration of TPA method with no effect on the useful pressure data. A sweep among the cut-off frequency of low-pass filter is seen in Figure 3.18. By reducing the frequency from 7 kHz, the spikes in HRR trace are mitigated insofar as 3 kHz which they were completely removed resulting in a normal HRR trace. The cylinder pressure fluctuations were also smoothed as the maximum pressure rise obtained by low-pass filter was 5.74 bar/deg while it was recorded 12.14 bar/deg before filtration.

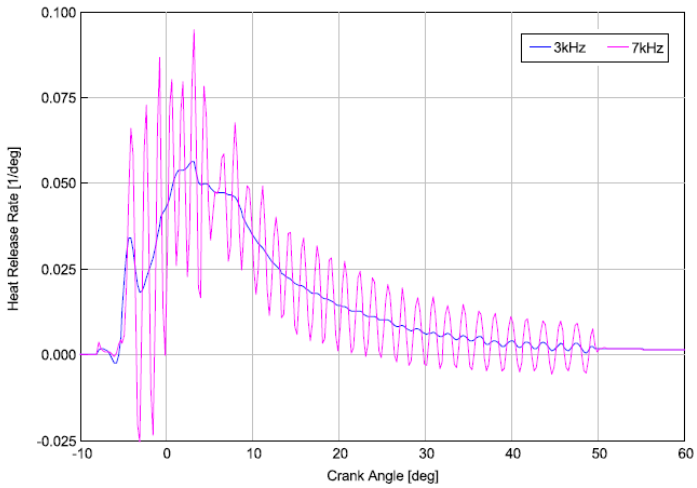


Figure 3.18: Cut-off frequency sweep of low-pass filtration - HRR

The origins for the combustion noise can be divided to direct and indirect factors. The direct noise is related to in-cylinder gas pressure over whole engine block regardless of piston speed. Indirect noise is consequence of gas forces on components making them move into their clearances [Keeler (79)]. Since the pressure trace ringing frequency could be estimated between 4 and 6 kHz (Figure 3.18), the existing pressure noise was resulted from the in-cylinder oscillations across the piston bowl and not derived from the pressure transducer. The Figure 3.19 presents the result of pressure treatment by TPA.

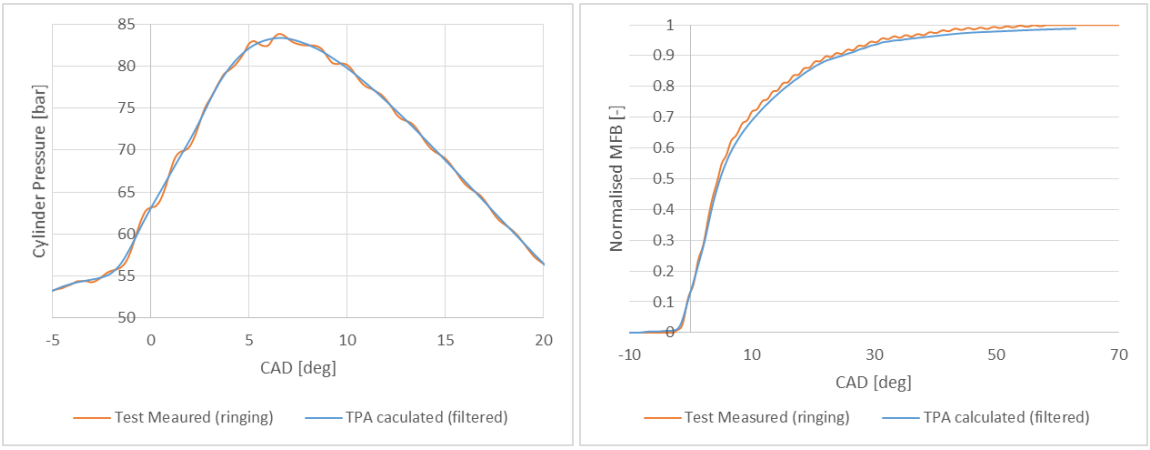


Figure 3.19: Ringing effect: (left) on cylinder pressure (right) on normalised mass fraction burned

One of the beneficial results of TPA method is presenting a detailed energy analysis. As seen in Figure 3.20, the "in-cylinder energy balance" provides a comparison of following measured and predicted results thus can be used as a calibration tool:

- "Total Fuel"
- "Burned Fuel"
- "Cumulative Energy" as the sum of internal Energy, work and heat transfer.

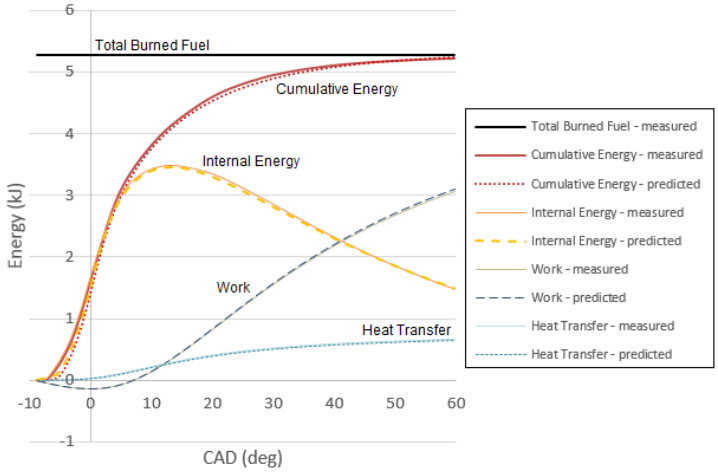


Figure 3.20: In-cylinder energy balance, HF = 15%

The combustion results of post-processing method explained in Section 3.5 (net heat release of [Heywood (7)]), are compared with those of TPA outputs. As seen in Table 3.6, there is very close similarity between all values except dPdCA_max which shows difference. This is because the test value is calculated from unsmoothed measured cylinder pressure while TPA has already filtered the PCyl hence resulted in lower and normal maximum in-cylinder pressure rise rate. The cumulative burn rate (MFB) comparison is made in Figure 3.21, which shows a very close estimation of TPA with LHV multiplier = 0.9727. The existing wrinkles on the measured MFB relates to the PCyl fluctuations due to combustion noise. These fluctuations are smoothed finely with TPA filtration. In conclusion, TPA was considered appropriate for smoothed post-processing of the measured test data obtained in the currently reported study.

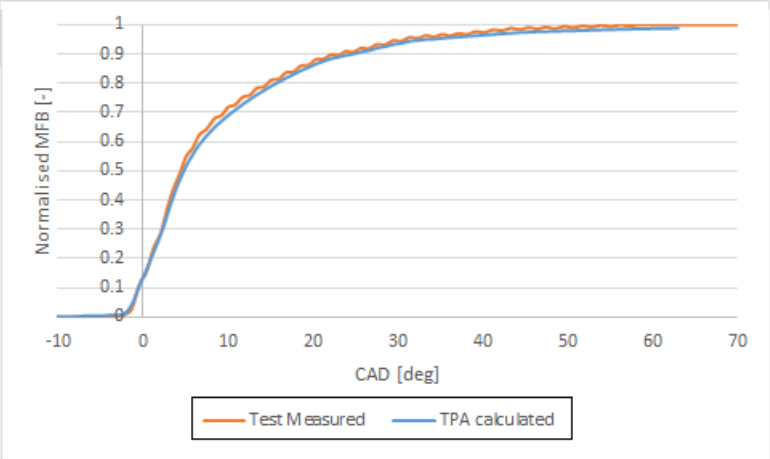


Figure 3.21: Normalised MFB: Test measured vs. TPA calculated

Table 3.6: Combustion parameters comparison: Net. Heat release post-processed results vs. TPA results

Parameter	Unit	Test RLTs	TPA RLTs
IMEPn	bar	6.052	6.052
PMEP	bar	-0.191	-0.191
Pmax	bar	83.840	83.39
CA_Pmax	deg ATDC	6.5	6.50
dPdCA_max	bar/CA	7.858	4.83
CA10	degATDC	-0.65	-0.48
CA50	deg ATDC	4.33	4.75
CA90	deg ATDC	23.27	23.02
CA10-CA90	deg CA	23.92	23.50

3.6.6 GT "DIPulse" combustion model

Although DIJet model can be used for modelling of DI diesel combustion, it has more complicated and slower performance than an alternative model, DIPulse which also can be coupled with "SITurb" model (explained in next section) in order to model Dual-fuel combustion.

DIPulse follows a strategy of tracking fuel as it is injected, evaporates, mixes with entrained air and finally burns. This model must be calibrated with experimental cylinder pressure analysis. Furthermore, in order to achieve acceptable correlation results, an absolute requirement is a precise injection profile which is in form of an "Injection Rate Map" obtained through the method explained in Section 3.6.3. Within DIPulse, the contents of the cylinder are split into three thermodynamic zones as illustrated in Figure 3.22:

(1) main unburned zone (MUZ) includes all cylinder mass at IVC

(2) spray unburned zone (SUZ) contains injected fuel plus entrained gas

(3) spray burned zone (SBZ) comprised of combustion products.

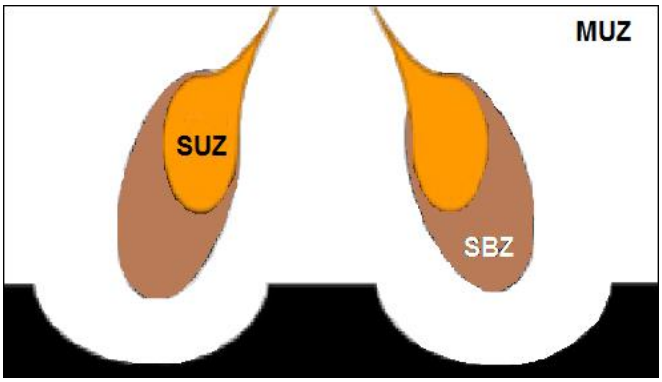


Figure 3.22: three zones of DIPulse model

The physical processes during injection and combustion are simulated by several sub-models within DIPulse, as summarised below and described in following paragraphs:

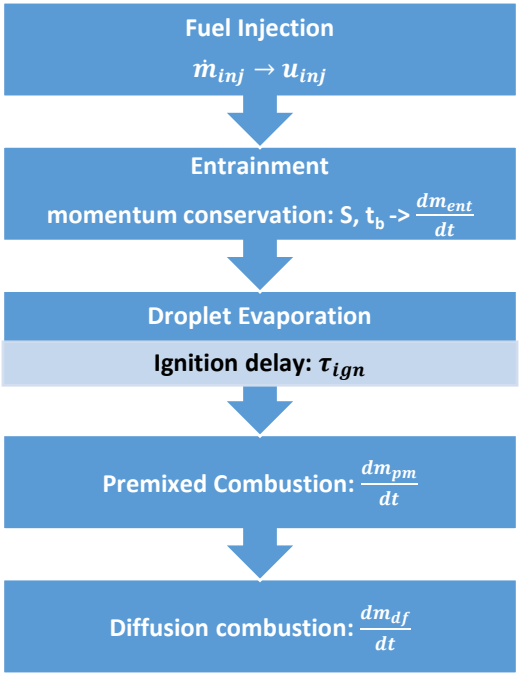


Figure 3.23: Flowchart of DIPulse calculations process

Fuel Injection: any number of injection pulses can be added to the SUZ through the "Injection Rate Map". This sub-model allow tracking each injection pulse individually with no influence on other pulses. The injection mass flow rate through the nozzle is given by:

$$\dot{m}_{inj} = C_D A_n \sqrt{2\rho_l \Delta P} \tag{3.20}$$

where C_D is the discharge coefficient of nozzle, A_n is the nozzle hole area, ρ_l is liquid fuel density and ΔP is the pressure drop across the injector nozzle. As $\dot{m}_{inj} = \rho_l A_n u_{inj}$, the fuel injection velocity at the nozzle tip (u_{inj}) can be expressed as [Jung et al. (80)]:

$$u_{inj} = C_d \sqrt{\frac{2\Delta P}{\rho_l}} \tag{3.21}$$

Entrainment: determines the position and velocity of each packet. The entrainment of unburned gases into the injection pulse causes it to get slowed and makes the intermixing of pulses possible. Using an empirical correlation for spray tip penetration described in [Jung et al. (80)], each packet's position (S) is determined:

$$S = \begin{cases} u_{inj} t \left[1 - \frac{1}{16}\left(\frac{t}{t_b}\right)^8\right], & t < t_b \\ u_{inj} t_b \frac{15}{16}\left(\frac{t}{t_b}\right)^{0.5}, & t \geq t_b \end{cases} \quad (3.22)$$

The breakup time (t_b) as the turning point for the spray penetration is derived by calculations presented in [Jung et al. (80)]:

$$t_b = 4.351 \sqrt{\frac{2\rho_l}{\rho_g}} \frac{d_n}{C_d u_{inj}} \quad (3.23)$$

where d_n indicates the injector nozzle diameter and ρ_g is the gaseous fuel density.

Applying the momentum conservation $(mu = m_{inj} u_{inj})$, the entrainment rate can be calculated and be modified by "Entrainment rate multiplier" (C_{ent}) [GT (63)]:

$$m_{ent} u = m_{inj} u_{inj} \rightarrow m = \frac{(m_{inj} u_{inj})}{u} \rightarrow$$

$$\frac{dm_{ent}}{dt} = -C_{ent} \frac{m_{inj} u_{inj}}{u^2} \frac{du}{dt} \qquad \left(u = \frac{dS}{dt}\right) \quad (3.24)$$

Evaporation: the evaporation of droplet is modelled with a coupled solution of heat and mass transfer. It accounts for limitations due to diffusion and boiling [Aggarwal et al. (81)].

Ignition Delay: The ignition delay is calculated by Arrhenius equation and can be altered by "Ignition Delay Multiplier" (C_{ign}). In addition to entrainment and evaporation, pulse-to-pulse interactions are accounted for ignition delay calculations [GT (63)].

$$\tau_{ign} = C_{ign} \rho^{-1.5} exp\left(\frac{3500}{T}\right) [O_2]^{-0.5} \quad (3.25)$$

The Ignition occurs when $\int_{t_0}^{t_{ign}} \frac{1}{\tau_{ign}} dt = 1$.

Premixed Combustion: Kinetically-limited premixed combustion at the beginning of pulse ignition is calibrated by "Premixed Combustion Rate Multiplier" (C_{pm}) [GT (63)].

$$\frac{dm_{pm}}{dt} = C_{pm} m_{pm} k \left(t - t_{ign}\right)^2 f([O_2]) \quad (3.26)$$

where k is turbulent kinetic energy and $[O_2]$ is oxygen concentration.

Diffusion Combustion: Ultimately, the remained unmixed fuel and entrained gas involves a mixing and diffusion-limited burning which can be calibrated by "Diffusion Combustion Rate Multiplier" (C_{df}) [GT (63)].

$$\frac{dm_{df}}{dt} = C_{df} m \frac{\sqrt{k}}{\sqrt[3]{V_{cyl}}} f([O_2]) \qquad (3.27)$$

where V_{cyl} is cylinder volume.

3.6.7 GT "SITurb" combustion model

Since the turbulence parameters such as integral length scale (L), rms turbulent velocity (u') and laminar burning velocity (u_L) are difficult to measure experimentally under engine conditions, a numerical model must be used to estimate these parameters. The GT premixed combustion model, named as "SITurb" is based on the Blizzard and Keck model [Blizard and Keck (82)] which is the most applicable "turbulent entrainment model" used for SI engines [Heywood (7)]. The computational steps for this model are depicted in Figure 3.24:

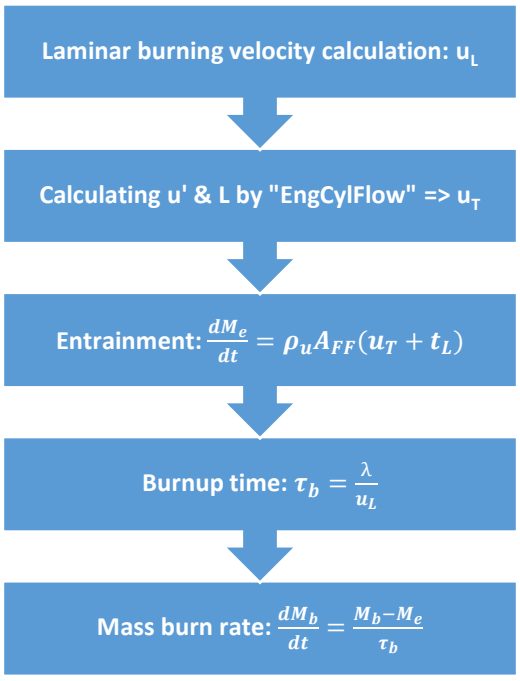


Figure 3.24: Flowchart of SITurb calculations process

This model is formed on three principle equations explained below. The entrainment rate of unburned mass into the turbulent flame is given by [GT (63)]:

$$\frac{dM_e}{dt} = \rho_u A_{FF} u_{te} \quad (3.28)$$

M_e: entrained mass — ρ_u: unburned density

A_{FF}: flame front area — u_{te}: turbulent entrainment velocity

The rate of mass burning is determined as [GT (63)]:

$$\frac{dM_b}{dt} = \frac{M_e - M_b}{\tau_b} \quad (3.29)$$

where ($M_e - M_b$) is the mass of entrained yet unburned gas and τ_b is the burning characteristic time defined in Eq. 2.8. Equations (3.28) and (3.29) in addition to Eq. 2.8, constitute the fundamentals of Blizzard and Keck model [Blizard and Keck (82)].

In GT-Power, the turbulent entrainment velocity in Eq. 2.8 has been replaced with ($\mathbf{u_T + u_L}$) in accordance with improvements applied to Keck and Blizzard model by Tabaczynski et al. [Hires et al. (83)]. This was aimed to split the effects of laminar burning velocity component normal to the flame surface and the turbulent distortion of flame surface.

As explained in Section 3.6.2, turbulence intensity (u') and integral length scale (L) are prescribed by in-cylinder flow which is modelled by "EngCylFlow" object in GT-Power. By adjusting the effects these parameters via three multipliers of SITurb model which are highlighted in red in the below equations, the premixed combustion can be calibrated [GT (63)]:

$$u_T = C_{TFS} u' \left(1 - \frac{1}{1 + C_{FKG} \left(\frac{R_f}{L} \right)^2} \right) \quad (3.30)$$

$$\lambda = \frac{C_{TLS} L}{\sqrt{Re_t}} \quad (3.31)$$

$$Re_t = \frac{\rho_u u' L}{\mu_u} \quad (3.32)$$

$\mathbf{C_{TFS}}$: turbulent flame speed multiplier — Re_t: turbulent Reynold number

$\mathbf{C_{TLS}}$: Taylor length scale multiplier — μ_u: unburned zone dynamic viscosity

$\mathbf{C_{FKG}}$: flame kernel growth multiplier — ρ_u: unburned density

3.6.8 GT "DualFuel" combustion model

The conventional spark ignition models are not precisely applicable for premixed dual-fuel combustion particularly during the ignition and early stages of combustion as the pilot injection is applied. Indeed, the prospect model for dual-fuel combustion would divide the

burn process into two dedicated regimes: pilot spray auto-ignition and the subsequent burning of premixed charge.

The “DualFuel” combustion model of GT-Power was used for predicting the burn rate for the dual-fuel engines where a pilot injection was used to ignite a premixed gaseous fuel/air mixture. This model combines two distinct combustion models: “DIPuse” and “SITurb”. DIPulse handles the burning of the direct injected fuel and any premixed fuel that is entrained by the fuel spray and SITurb will model the resulting flame propagation for the premixed mixture. Both these two models take effect in parallel with an interaction between them.

Regarding optical observations, at the beginning of combustion, the spray shaped flames are formed. Then the flame front propagates into the unburned zone and ultimately will dominate the whole combustion chamber. Although, the flame front area for SITurb will initially use the conical area of the spray from DIPulse but the flame will finally transit to a spherical flame as seen in Figure 3.25. A linear transition function will model this transformation [Walther (84)]:

$$A_{FF} = \left(1 - \frac{R_f}{l_{k0}}\right) A_{FF_jet} + \left(1 - \frac{R_f}{l_{k0}}\right) A_{FF_hemispherical} \tag{3.33}$$

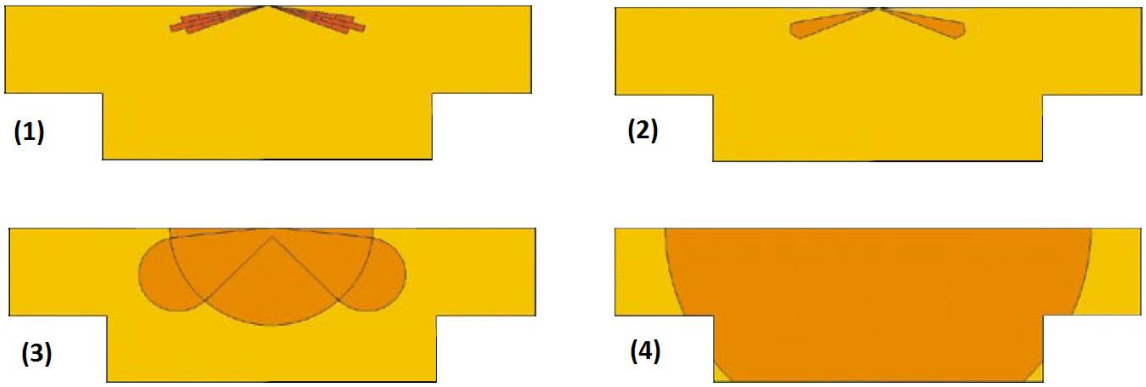


Figure 3.25: Flame propagation in GT DualFuel model [Walther (84)]

The flame jet geometry includes a truncated cone and a hemisphere. Its incremental growth is depicted in Figure 3.26 as it is required for surface area calculation in Eq. 3.33.

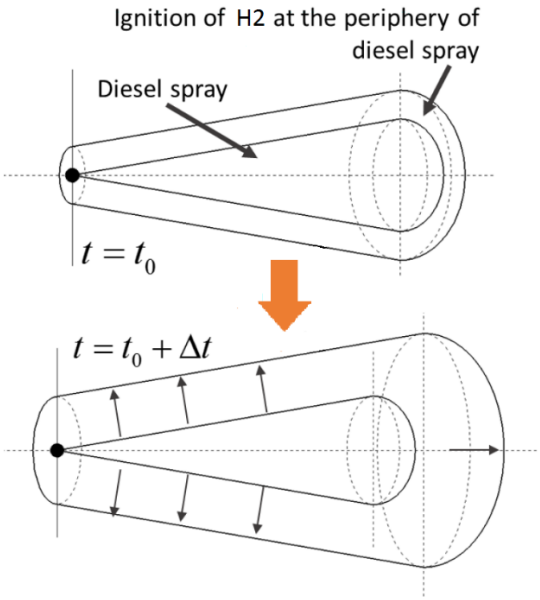


Figure 3.26: incremental flame growth in GT DualFuel model

3.7 Summary

The test engine and H2/O2 enrichment setup in addition to all experimental devices were described at the beginning of this chapter. Later, the data post-processing of DAQ system was presented. The numerical methodology including different aspects of the simulation program and its optimisation methods were described. In addition, GT models such as DIPulse, SITurb and DualFuel were introduced specifically.

Chapter 4: Experimental Evaluation of hydrogen enrichment of diesel test engine

The following sections present the experimental results of hydrogen and oxygen enrichment in a HD diesel engine via "fumigation" approach. This approach is in accordance with two pathways for hydrogen supply mentioned in Section 2.6: on-board diesel fuel reformation and hydrogen electrolysed from renewable sources.

4.1 Testing conditions for hydrogen enrichment

As indicated in Table 4.1, two specific operating points were chosen for the hydrogen enrichment. The first corresponds to 1200 rpm and 6 bar IMEPn, equivalent to 25% load representing operating point #7 of the ESC13 i.e. A25. The second operating point was 1200 rpm and 12 bar IMEPn, equivalent to 50% load close to point #5 of the ESC13 i.e. A50.

Based on energy input, the hydrogen fraction ratio (HF) was calculated, Eq. (4.1):

$$HF = \frac{\dot{m}_{hydrogen} LHV_{hydrogen}}{\dot{m}_{hydrogen} LHV_{hydrogen} + \dot{m}_{diesel} LHV_{diesel}} \qquad (4.1)$$

With aim of simplification in writing, it is convectional to use "H" plus a number to refer to a specific hydrogen fraction ratio (e.g. H20 means HF = 20%).

Table 4.1: Engine Operating Conditions of H2 enrichment

Parameter	***Operating Point 1 (A25)***	***Operating Point 2 (A50)***
Engine Speed	1200 rpm	1200 rpm
Load (IMEPn)	6 bar	12 bar
Intake Air Temperature	309 K	318 K
Intake Pressure	125 kPa	190 kPa
Exhaust Pressure	135 kPa	200 kPa
EGR Rate	25%	25%
EGR Temperature	339 K	367 K
Rail Pressure	1250 bar	1400 bar
Diesel Injection Strategy	Pre-injection	Pre-injection
H2 Energy Fraction Range	0% to 65%	0% to 35%

Figure 4.1 denotes where the operating points (patterned circles) are placed over the operational map of a HD engine fitted to a truck. The selected test points are placed in a frequent residence area of a generic HD engine driving cycle. The corresponding baseline calibration is based on operating conditions optimised during the prior work done by Vinicius Pedrozo [Pedrozo (85)] at Brunel University.

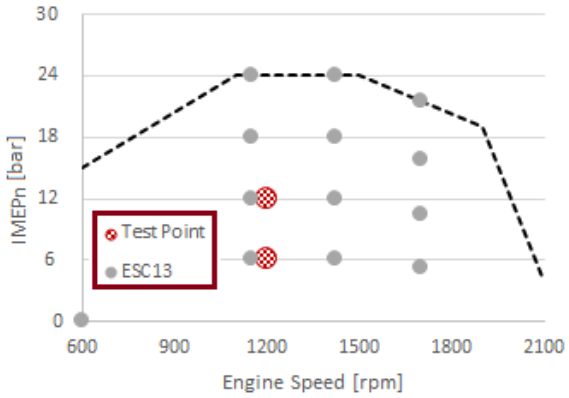


Figure 4.1: The selected test points with ESC13 points over the HD engine operational map

By optimising the injection pressures and timings (SOI), it was aimed to obtain the best indicated efficiency-ISSoot trade-off. While H2 substitution ratio was altered with 10% and 5% increments at A25 and A50, respectively; it is worthwhile to note that highest hydrogen fraction in each operating point, was limited by the maximum flow rate of H2 mass flow controller (100 lit/min).

4.2 H2-Diesel combustion analysis

Initially, with aim of reducing the high pressure rise rate (PRR), pre-injection strategy was followed. As seen in Figure 4.2(a), pre-injection allowed the heat release rate (HRR) reduction with lower pressure rise rate (PRR). The same sensation was observed during hydrogen enrichment while keeping the SOIs fixed (with lower main injection duration), Figure 4.2(b). Hence, the pre-injection resulted in advancing SOC and reducing ignition delay. As single injection resulted in very high in-cylinder pressure rise (> 20 bar/CAD) with remarkable higher HHR, the pre-injection strategy was chosen for all test cases.

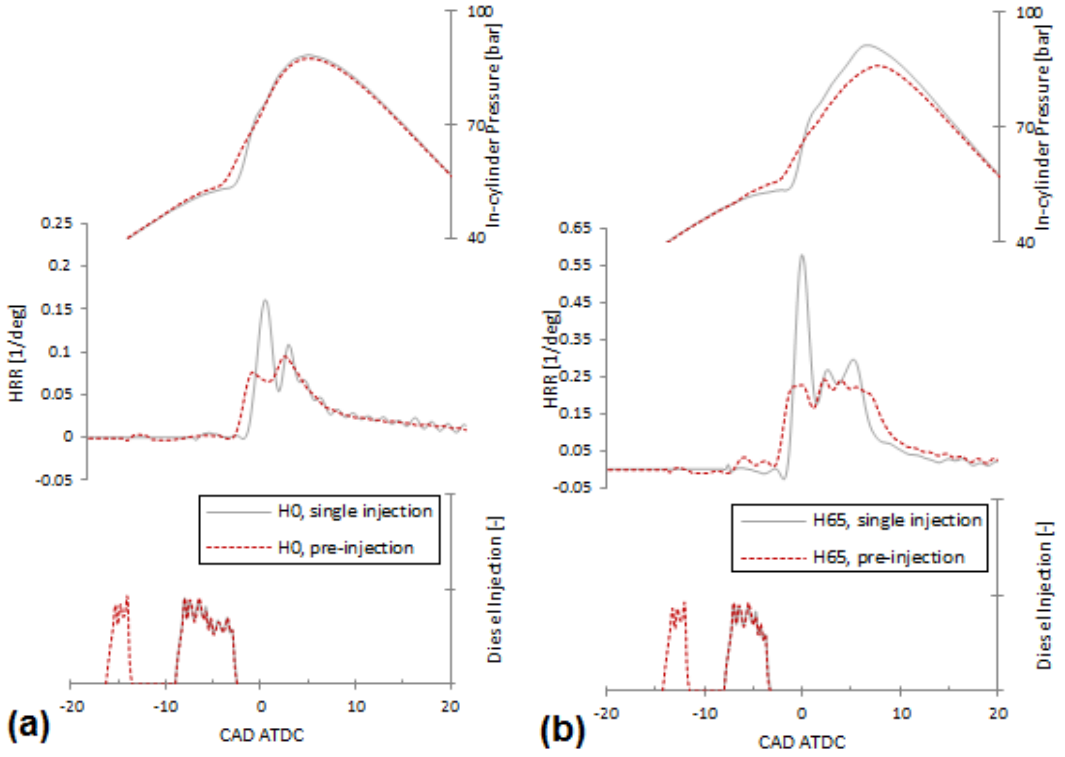


Figure 4.2: Use of pre-injection to reduce combustion noise_A25 (a) diesel-only (H0) (b) dual-fuel (H65) [Monemian et al. (27)]

According to the conceptual model proposed in Section 2.6 by [Morgan et al. (19)], for experimental studying effect of hydrogen enrichment on diesel combustion, in each two operating points, specific hydrogen substitution ratios were selected regarding their H2 concentration in air. Their corresponding burn rate and cylinder pressure plus the key attributes were post-processed by the three-pressure analysis (TPA) reverse-run calculation (explained in Section 3.6.5) on the measured test results.

Combustion characteristics affected by hydrogen enrichment over two test operating points are presented in Figure 4.3. While φ_{global} was kept fairly constant for both loads, it was leaner at low load compared to mid load. Evaluating in-cylinder flow, it was observed that volumetric efficiency dropped drastically as expected. This is because significant amount of intake air was displaced with hydrogen which although has higher LHV but low molecular weight.

The key parameter, CA10-CA50, represents the premixed combustion part which set out and dominates the entire combustion process. While it was almost reluctant at A25, it was reducing monotonically by H2 enrichment at A50. This phenomena is felt well in burn rate

comparisons presented in Figure 4.5 and 4.7 as there is no variation at A25 while significant change is seemed at A50. The same trend was seen for combustion timing (CA50). These prove stimulating effect of hydrogen enrichment which was more pronounced at mid load in comparison to low load. In addition, as presented later in Section 5.4.4, the flame radius and mass fraction burned for all selected cases at A25 except H65, are fairly reluctant to H2 enrichment.

Nevertheless, combustion duration (CA10-CA90) was descending for both loads with shorter combustion for A25 cf. A50. A similar trend is reported in [Dhole et al. (86)]. Ultimately, despite higher cyclic variation at A50, the COV_IMEPn was slightly affected by HF change, resulted in reasonable COV (< 5%) for both loads.

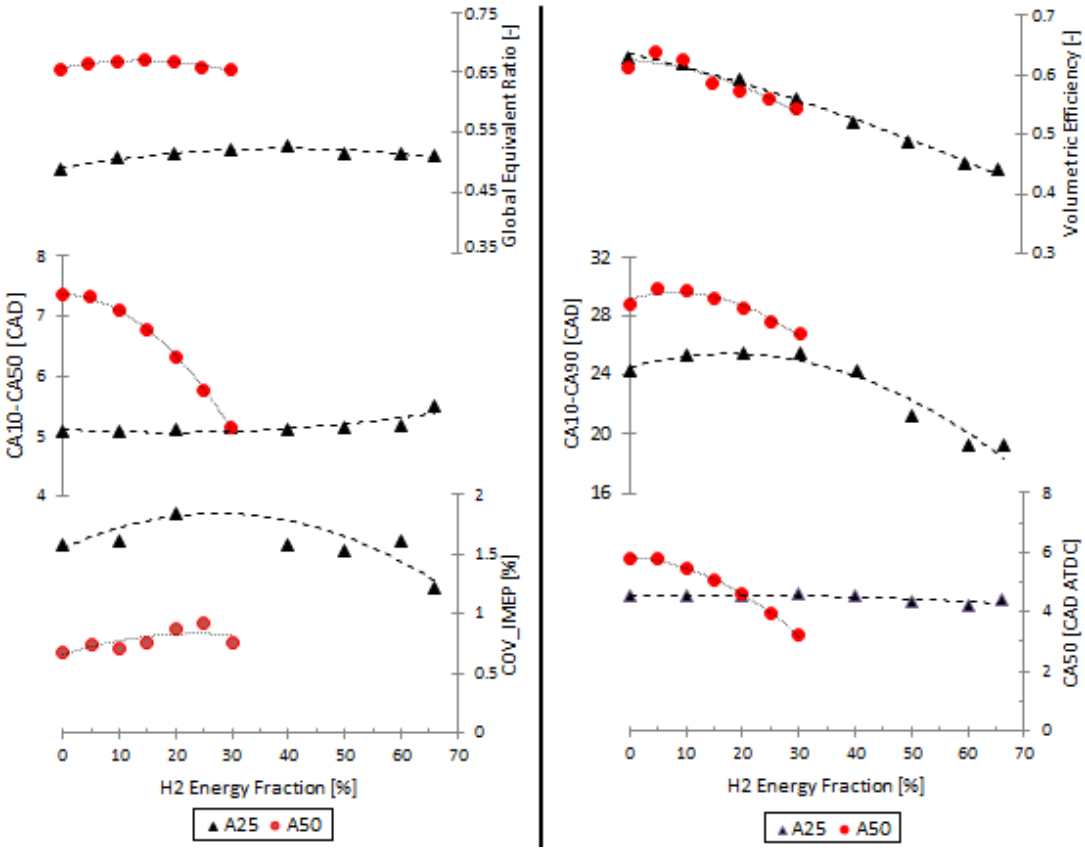


Figure 4.3: H2-diesel: Combustion characteristics [Monemian et al. (27)]

4.2.1 H2-Diesel combustion: low load operation (A25)

With aim of focusing on the effects of hydrogen enrichment on the H2-diesel combustion, 4 specific test cases were selected in the A25 operating point: H0, H20, H40 and H65. In low

load, less diesel fuel is required for the injection pulses (pre and main). This can be problematic, since more diesel fuel is needed to be premixed with aim of promoting mixture flammability at low equivalence ratio and temperature. However, there must be still enough ignition energy to be provided by second (main) injection. Thus, the injection pulses must be retarded to allow more stratification. This stratification causes the differentiation in local chemical reaction rates and hence have influences on the ignition delay and combustion duration as seen in Figure 4.5. In addition, this late injection in A25, makes the probability of spray impingement on piston and hence increasing the CO and HC emissions cf. A50 operating points as seen in Figure 4.9.

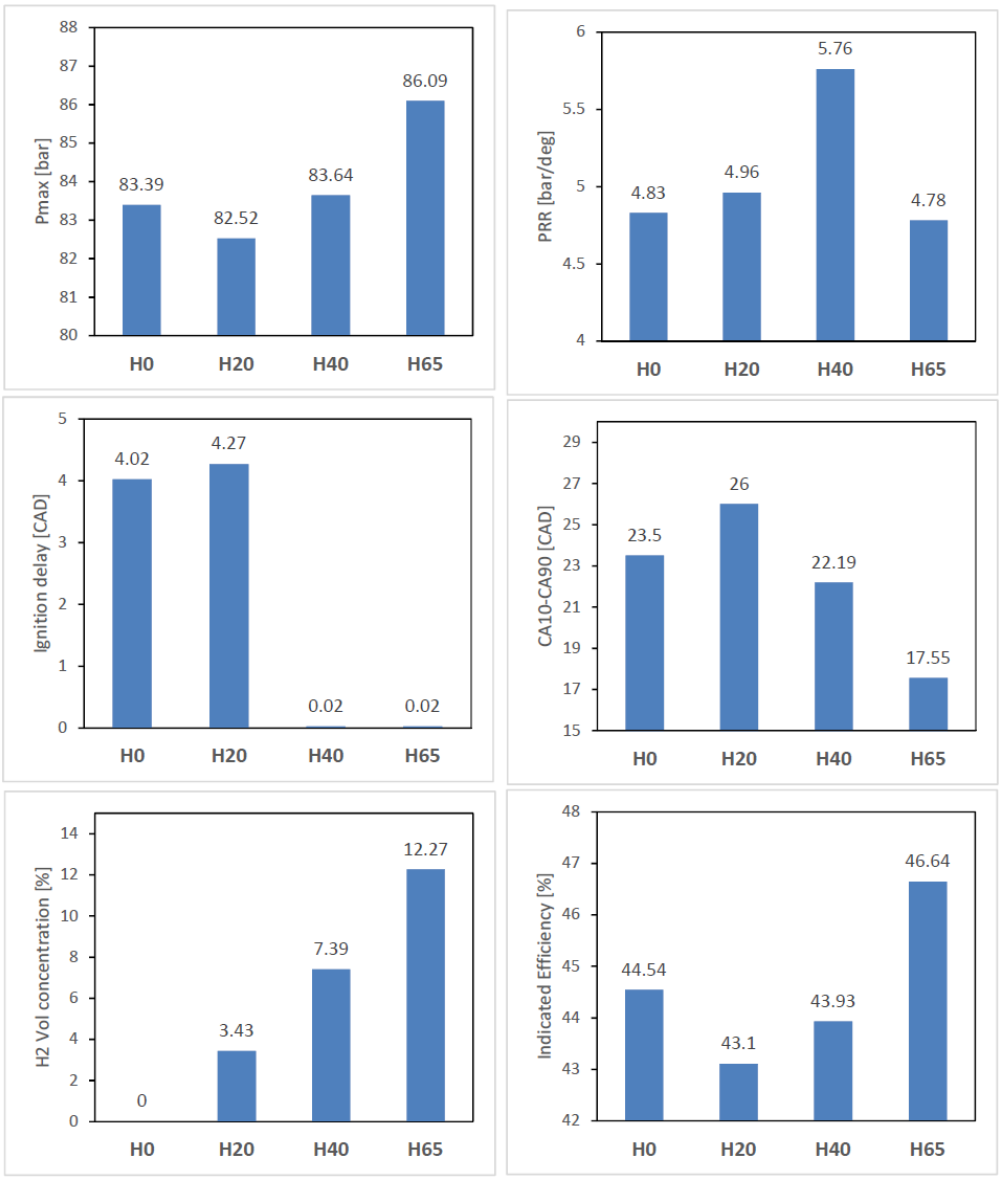


Figure 4.4: Key attributes of the selected cases at A25

Key attributes of the selected cases (obtained by TPA) are presented in Figure 4.4. The LFL of hydrogen (4% Vol concentration in air) is considered as the threshold which H2-diesel combustion would be evolved. After this threshold which results in hydrogen pre-ignition in the premixed charge, the ignition delay is almost vanished. In addition, combustion has been accelerated dramatically resulting in enhancing the indicated efficiency. Hence, the H65 has the shortest combustion duration with highest indicated efficiency approx. 4.7% higher than diesel-only case (H0).

Despite the variations in key attributes of selected test cases, the cylinder pressure and burn rate trends are pretty similar for various HFs. The reason can be related to low load characteristics which impede the hydrogen enrichment influence.

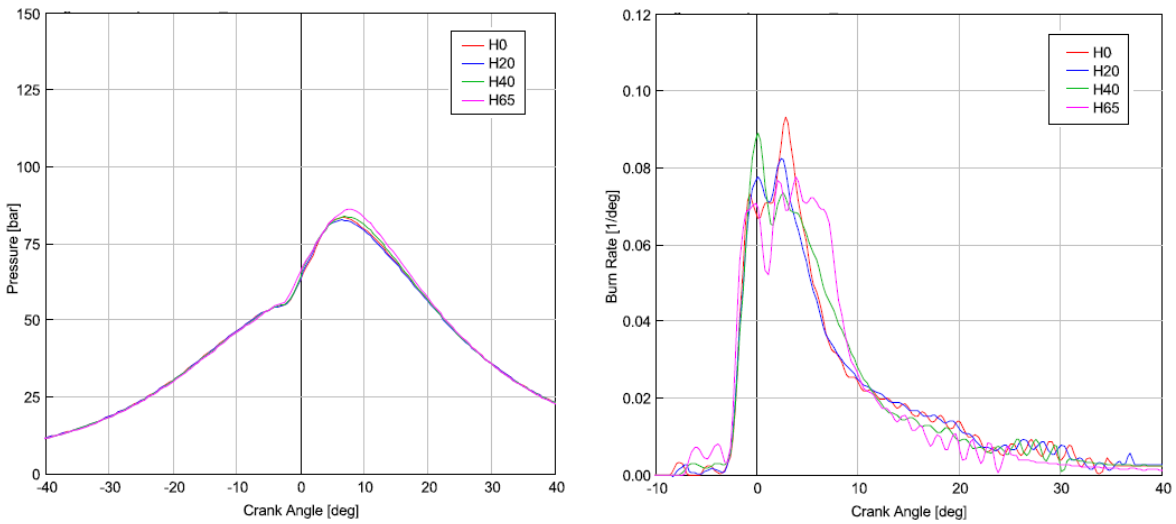


Figure 4.5: H2-diesel at A25: Cylinder pressure (left) and burn rate (right)

4.2.2 H2-Diesel combustion: medium load operation (A50)

Three test cases at A50 were selected for presenting the effects of hydrogen enrichment: H0, H15 and H30. In contrast to the selected cases of A25, the H2 enrichment influence has evolved the combustion process for A50 cases. This claim is affirmed in Figure 4.7 particularly for H30 where all key attributes were changed for both corresponding pressure and burn rate. Indeed, the mode 1 of the proposed conceptual model [Morgan et al. (19)] is well presented in H30 whereas hydrogen pre-ignition prior to diesel fuel injection has been a game changer.

This phenomenon resulted in higher maximum pressure and PRR. In addition, combustion timing is advanced and burn duration is shortened significantly. More importantly, indicated efficiency has increased up to 46.44% i.e. 2.3% increase cf. H0 case. This is because less heat was transferred to cylinder wall due to faster combustion.

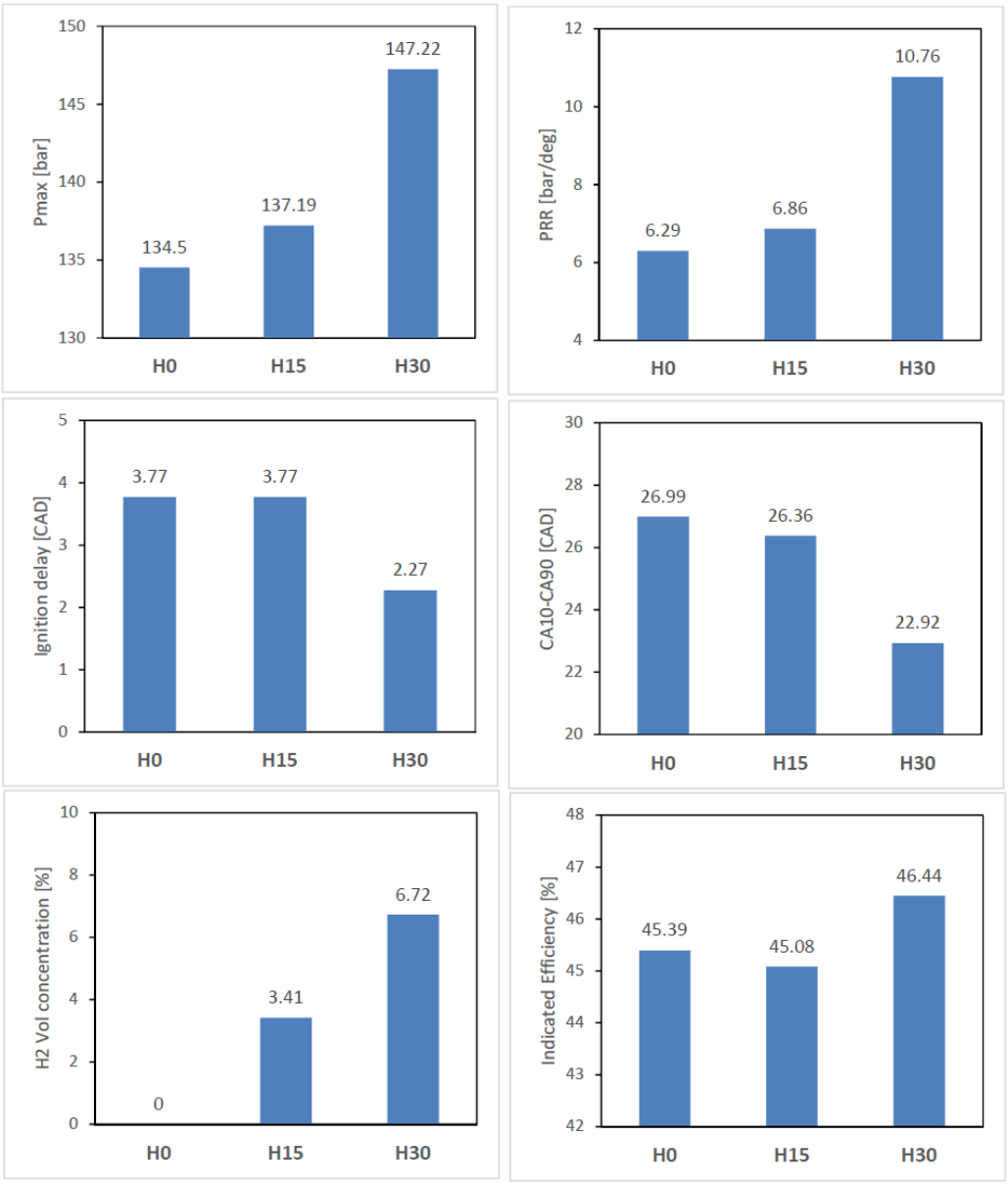


Figure 4.6: Key attributes of the selected cases at A50

As seen in Figure 4.7, for H30, the pre-ignition of hydrogen has dominated in premixed combustion section of H2-diesel dual-fuel combustion and this trend increased substantially at 30% substitution. Hence, this test point stands out from other ones due to the arising abnormal heat release.

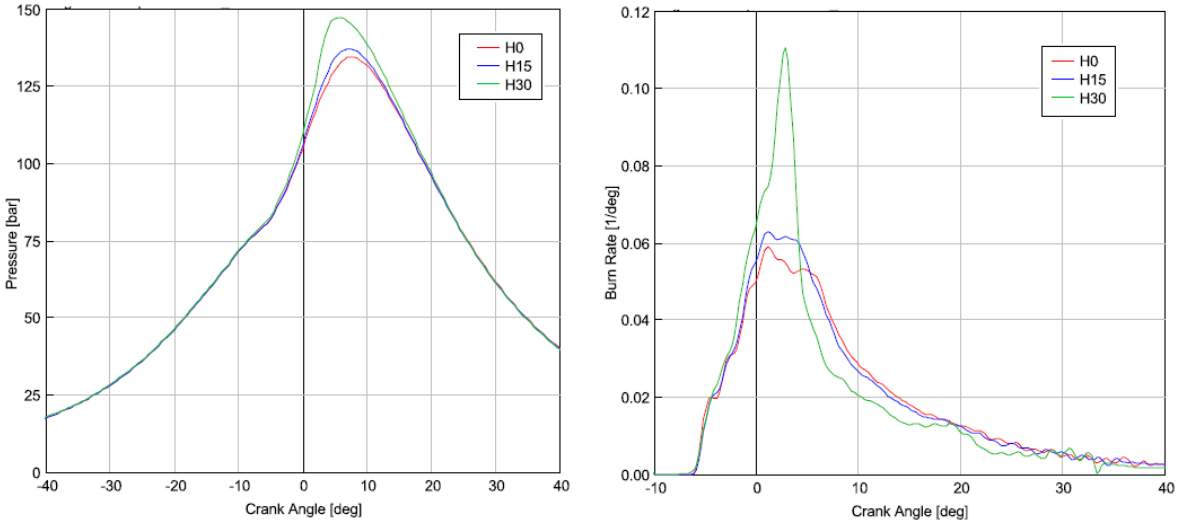


Figure 4.7: H2-diesel at A50: Cylinder pressure (left) and burn rate (right)

4.3 Exhaust emissions and performance of H2-Diesel combustion

Hydrogen enrichment had a positive effect on all carbon-related pollutants specially CO2. According to Figure 4.8, ISSoot, ISCO and ISCO2 all decreased abruptly by increasing HF for both loads due to reduction of the C / H ratio. This trend of dropping CO2 emissions within dual-fuel HD diesel engine is very rewarding as the conventional HD diesel engines suffer from high CO2 emission seriously.

On the other hand, nitrogen oxides emission rate increased with higher mass flow of hydrogen, as H2 stimulates the combustion leading to higher temperatures. NOx-phi correlation presented in [70] can justify the ISNOx trends presented in Figure 4.8. As average equivalence ratio at A25 was near NOx rising threshold (φ = 0.5), this resulted in relatively low increase of NOx emission (~26% c.f. diesel-only) in 6 bar IMEPn. However, the NOx increase was significant at 12 bar IMEPn which exceeded 56% as the equivalence ratio was higher (φ = 0.66) at A50. A same NOx trend was observed by relevant work in [Verhelsta et al. (87)].

One interesting characteristic with hydrogen fumigation was remaining the ISHC fairly reluctant, particularly at A25, where it was unchanged. This can be due to constant combustion timing.

Adding small amounts of hydrogen led to slight reduction in indicated efficiency, potentially associated with reduced ratio of specific heats due to displacement of air. The reason for initial drop in efficiency could be due to 'hydrogen slip' (incomplete combustion of hydrogen) as claimed in [Morgan et al. (19)]. This issue was more pronounced at low load as the diesel fuel injected was relatively small, hence the gaseous fuel could not fully burn by entraining into the liquid fuel. However, at higher substitution ratio the faster combustion of hydrogen outweighed this effect and led to improved efficiency especially after hydrogen's lower flammability limit (LFL = 4% Vol). At A25, η_{ind} has a detrimental effect in the small hydrogen fractions until HF = 30%, where after efficiency starts to rise significantly until η_{ind} = 46.5%. For A50, elevated η_{ind} starts to recover at HF = 10% and reaches a peak of 46.4% at the highest attainable HF.

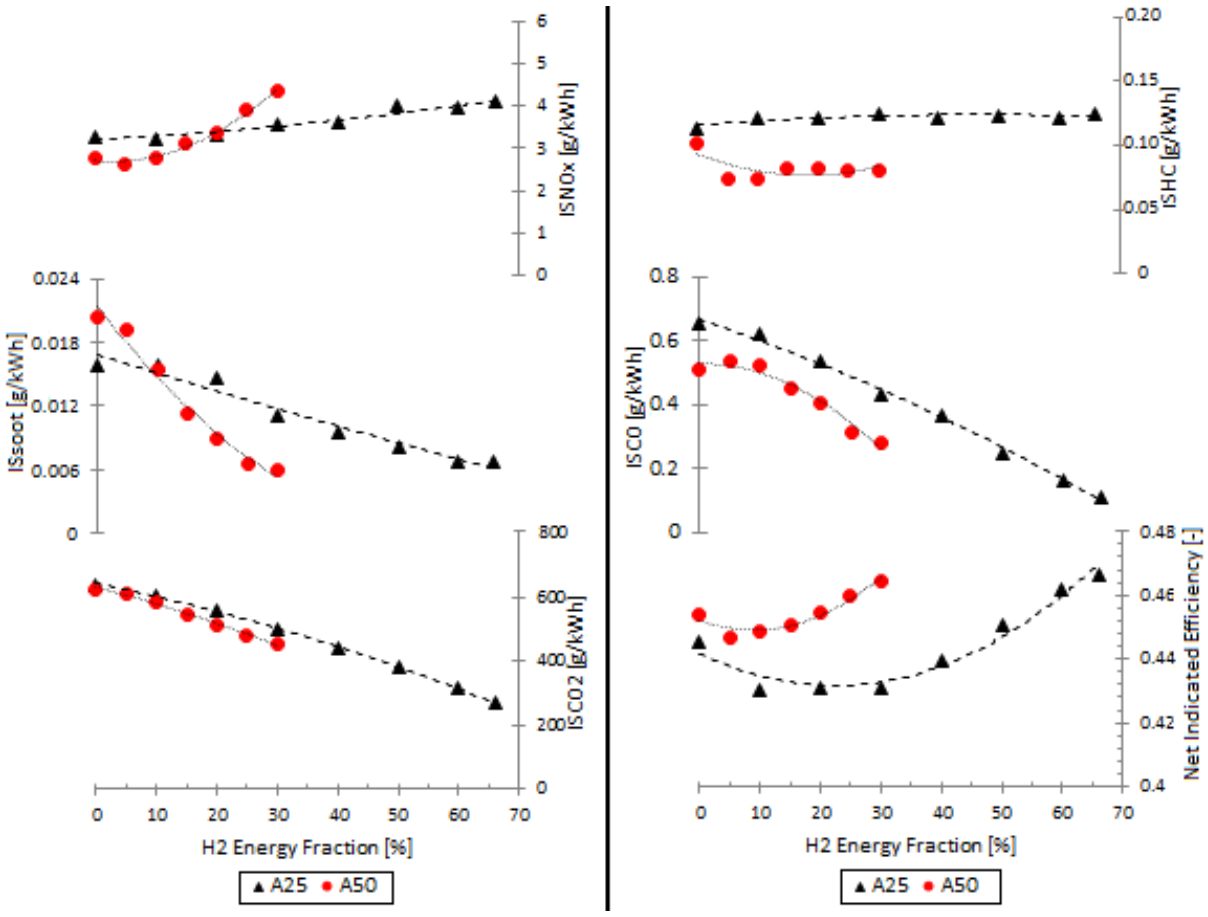


Figure 4.8: Exhaust Emissions and Performance (A25 and A50) [Monemian et al. (27)]

The emission alteration for highest hydrogen fractions in two test points regarding the diesel-only baseline is presented in Figure 4.9.

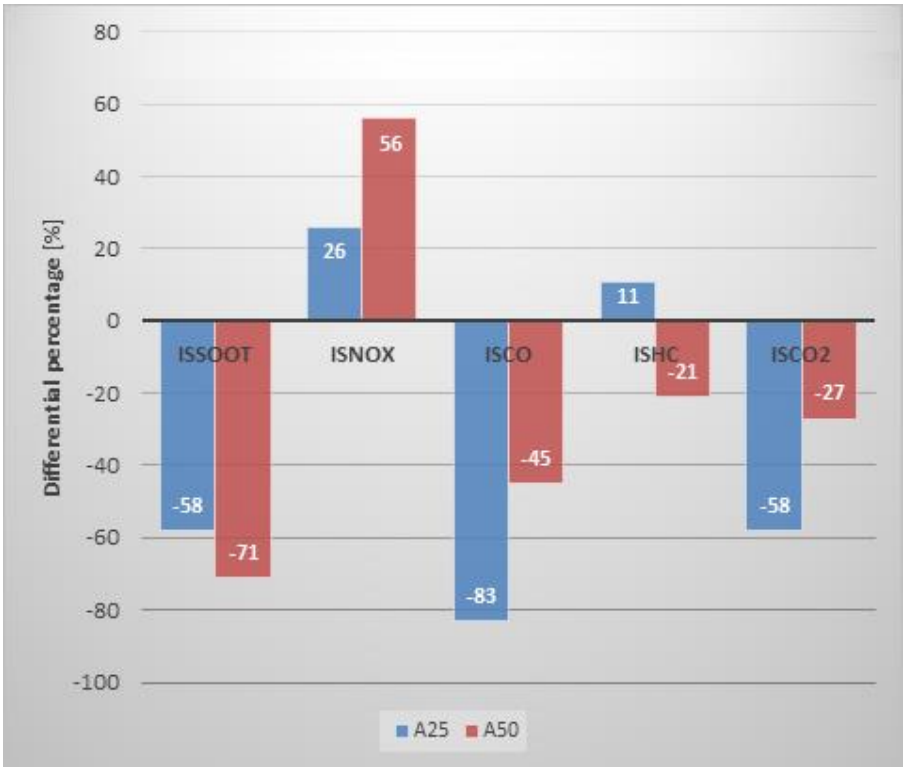


Figure 4.9: Emissions alteration of highest HFs (H65 at A25 and H35 at A50) to the diesel baseline

4.4 Oxygen enrichment of H2-Diesel combustion

As explained in Section 3.3, the initiative for current work was developing an on-board electro hydrogen generation machine. Since, the output of this machine was hydrogen and oxygen, it was aimed to study a process which these pure gases joined with diesel in a HD engine. Therefore, in second testing stage, hydrogen substitution ratio was fixed (HF = 20%) and pure oxygen was fumigated into the intake air pipeline in order to vary the actual O2 concentration of the intake charge. This would simulate the ideal output conditions of the hydrogen generator when it joins the HD diesel engine. In addition, EGR rate was varied to allow two different cases.

It is worthwhile to mention that O2 enrichment levels were approximately equivalent to 10% and 20% of the initial O2 concentration in each particular cases taking into account that H2 and EGR gases would occupy part of intake charge and alter the exact air mass. The Table 4.2 presents the details of testing point:

Table 4.2: Operating Conditions: O2 enrichment of intake air

Parameter	Test Point 1	Test Point 2
Speed	1200 rpm	1200 rpm
IMEPn	12 bar	12 bar
H2 Energy Fraction	20%	20%
EGR Rate	0%	30%
EGR Temperature	-	372 K
Intake Air Temperature	320 K	320 K
Intake Pressure	1.90 bar	1.90 bar
Exhaust Pressure	2.00 bar	2.00 bar
Rail Pressure	1400 bar	1400 bar

Figure 4.10 shows effect of O2 enrichment on in-cylinder pressure and HRR. O2 addition caused slight increase to these parameters due to providing a leaner combustion as global equivalence ratio shows in Figure 4.11. As expected, EGR had mitigated the maximum pressure and rate of heat release in comparison to non-EGR mode.

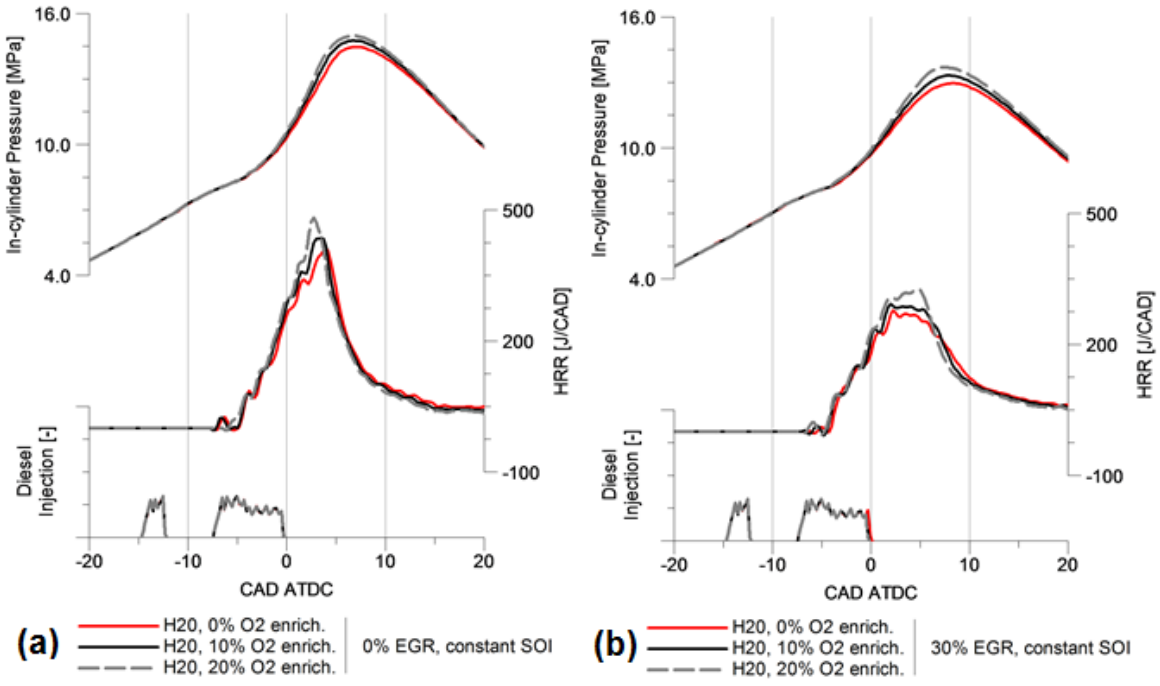


Figure 4.10: O2 enrichment combustion effects: (a) 0% EGR (b) 30% EGR [Monemian et al. (88)]

As seen in Figure 4.11, O2 enrichment has shortened slightly the combustion duration due to leaner in-cylinder condition. In addition, combustion phasing and CA10-CA50 duration were decreasing. This trend is well presented with EGR rather than without it. It is obvious that dilution effect of EGR caused overall deceleration in burn process.

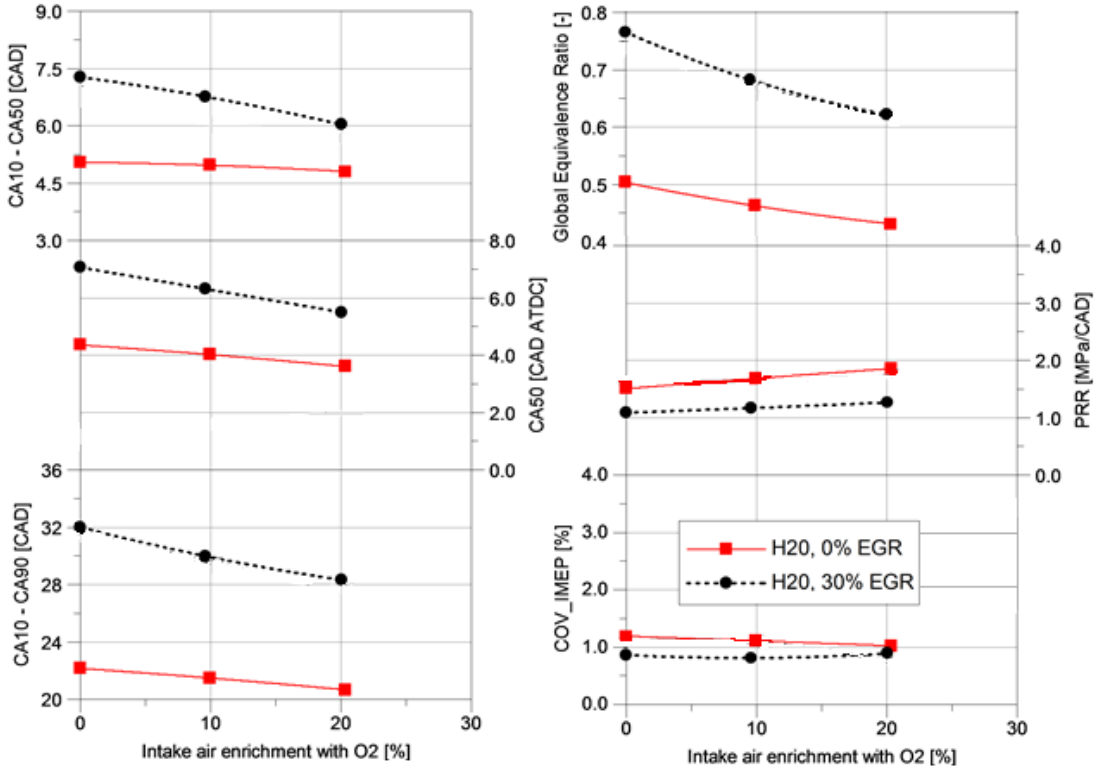


Figure 4.11: O2 enrichment: In-cylinder conditions [Monemian et al. (88)]

On other hand, EGR mitigated the pressure rise and stabilised the combustion in comparison to the EGR mode. In addition, it was well expected that EGR mode provides lower T_{max}, therefore it would restrain the NOx formation as seen in Figure 4.12. However, enriching O2 had made the charge leaner, so the ISNOx trend is rising. In non-EGR mode (red lines in Figure 4.12), CO, CO2 and soot were unwilling to change with O2 enrichment. This can be due to excess oxygen which had not limited the carbon oxidation. However, in EGR mode (black lines in Figure 4.12), CO and soot pollutants were decreasing dramatically while enriching the intake charge with oxygen, since the shortage of oxygen (due to replacement with exhaust gas residuals) was compensated. Ultimately, although indicated efficiency was increasing with O2 enrichment in EGR mode, it was decreasing in non-EGR mode.

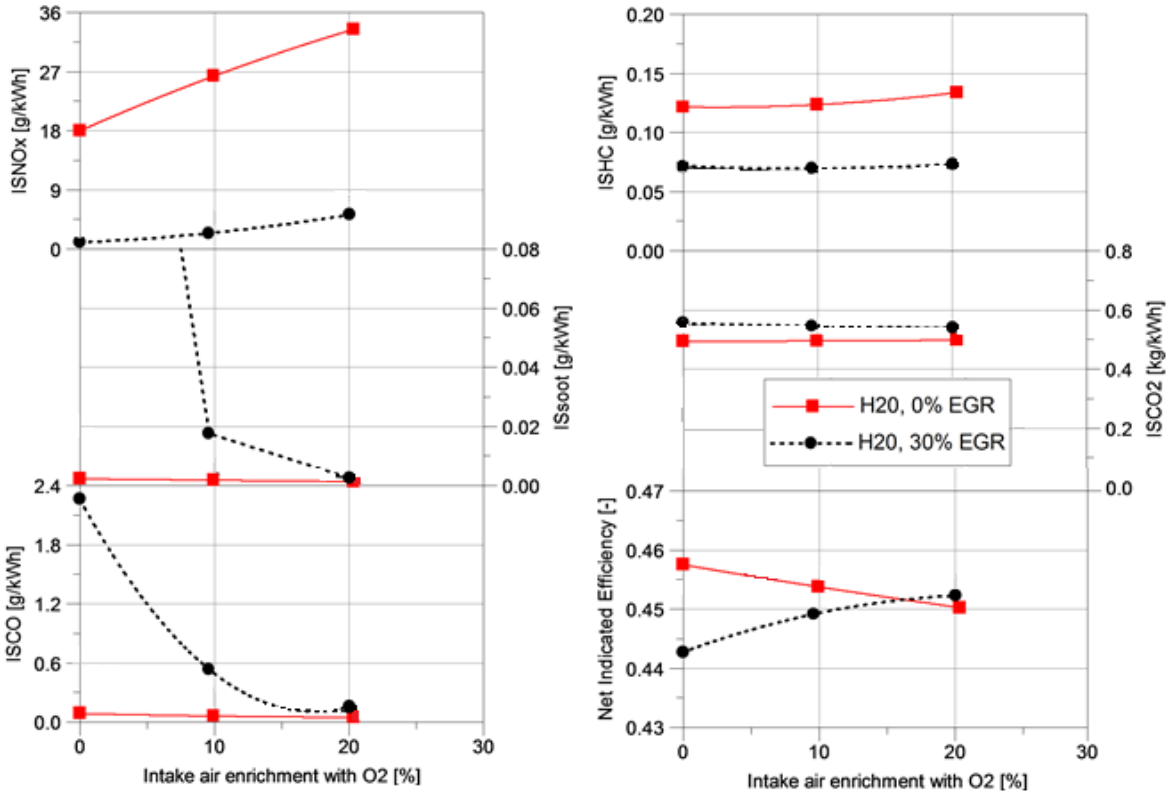


Figure 4.12: O2 enrichment: Emissions and indicated efficiency [Monemian et al. (88)]

It is worthwhile to mention that making the on-board reformation viable requires deeper investigation of the dual-fuel combustion. The computational fluid dynamics (CFD) and optical diagnostic techniques can be beneficial to have more insight into this type of combustion. Although, the current study had looked into the ideal conditions of introducing hydrogen and oxygen as the outputs of EHG machine (explained in Section 3.3), the feasibility of this idea must be studied in a case which this machine can be practically connected to an IC engine under real operating conditions.

4.5 Summary

Nevertheless, the outcomes of hydrogen enrichment on a HD diesel engine can be rewarding for the future studies and the key findings are concluded as follow:

- The highest obtained hydrogen fractions made indicated efficiency to increase up to 4.6% at 6 bar IMEPn (HF = 65%) and 2.4% at 12 bar IMEPn (HF = 35%), respectively.

- CO2 emissions were reduced by 58% and 32% at 6 and 12 bar IMEPn respectively, using highest HF. Soot and CO emissions were reduced as more hydrogen was injected, particularly at the lower load of 6 bar IMEP.

- The O2 enrichment strategy curbed smoke and minimised CO emissions to the detriment of considerable NOx increase.

Chapter 5: Numerical Study of H2-Diesel Combustion

5.1 Introduction

This chapter starts with discussion of various optimisation methods for simulating the baseline diesel-only mode via Sensitivity Analysis. Later, the empirical Wiebe function is used for dual-fuel modelling. The multipliers of GT "DIPulse" and "SITurb" models are characterised. The chapter concludes with full assessment of the GT "DualFuel" modelling of measured H2-Diesel results considering the performance of the model.

5.2 Optimisation solution

In association with TPA, the "Burnrate RMS" error can represent the error between the burn rate predicted by predictive model and experimental burn rate measured by TPA. Our optimisation aim was minimising this error. With this aim, the threshold of 0.005 was determined for the burnrate RMS which the values lower than that give acceptable burn rate correlation.

In this section, two optimisation methods were considered for evaluating the effect of 'DIPulse' diesel combustion model multipliers to correlate the baseline diesel-only combustion.

5.2.1 Design of Experiments (DOE)

Initially, the Design of Experiments (DOE) optimisation method was used with DIPulse multipliers ranges recommended by Gamma Technologies, Table 5.1.

Table 5.1: Recommended range for DIPulse multipliers [GT (63)]

DIPulse multiplier	Min. value	Max. value
Entrainment Rate	0.95	2.8
Ignition Delay	0.3	1.7
Premixed combustion Rate	0.05	2.5
Diffusion Combustion Rate	0.4	1.4

Since DOE is only evaluating mathematical models for each iteration, its runs are very fast. Among 7 types of DOE in GT-Power, the "Latin Hypercube DOE" was considered. This method divides the range of each factor into a number of equal-sized ranges (bins) equal to requested number of experiments. Each experiment will contain a random value from

within one bin for each factor and each bin will be used only once within design matrix. This DOE type is used when there is no prior knowledge of approximate shape of resulting response surface. Latin Hypercube has some merits in comparison to the 'Full Factorial' type which considers all possible combinations of factors: fewer experiments, better Burn Rate RMS Error and better curve fitting [GT (89)].

By running DOE, the results were processed in DOE-POST by applying a 'Model Fit' with most common fitting method, "Quadratic Least Squares". Model fitting is usually a manual trial-and-error process where one fit is tried, the model is evaluated, and then another is tried, and so on. Once an adequate fit has been found, the other DOE-POST features can be explored.

After applying a model fit, the Residual-XY plot should automatically appear. A well fit model will have all points lying on or near the line with slope = 1, Figure 5.8. The "coefficient of determination" (R2), as the square of the correlation between two general variables is calculated for this model fitting.

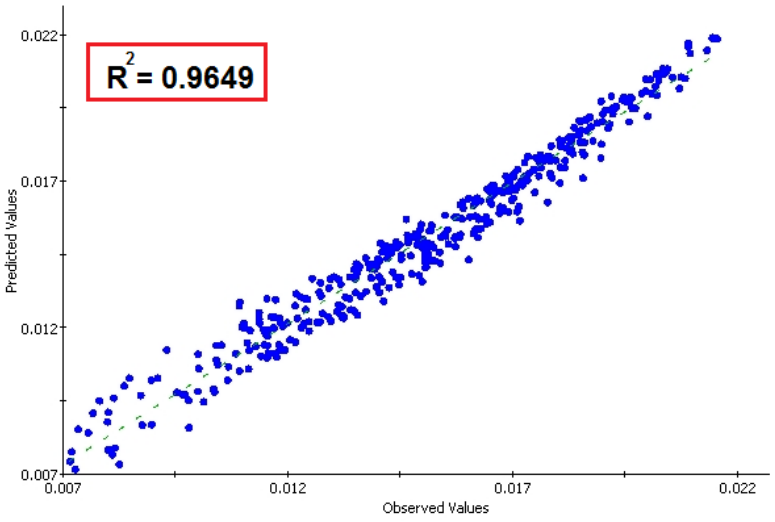


Figure 5.1: Residual plot for fitted model for DOE of baseline diesel-only single injection at A50

The coefficients plot for each of the polynomial terms within the response surface is presented in Figure 5.2. Each factor is normalized between a range of -1 and 1 while each response is normalized by the maximum value. The relative height of each bar presents the relative importance of each polynomial term to the overall response. It is seen that first degree of diffusion, entrainment and ignition delay multipliers have the most importance in the response surface respectively.

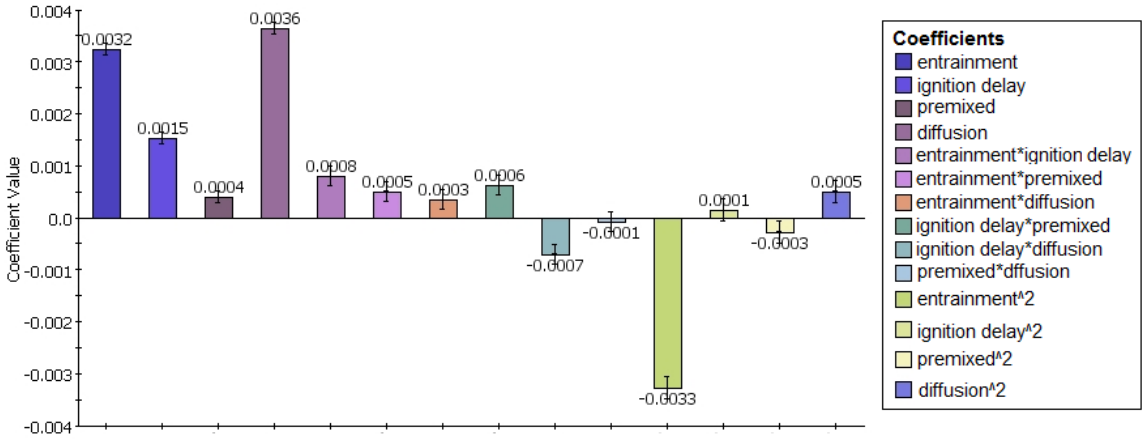


Figure 5.2: Coefficients plot of quadratic least squares fitting surface, diesel baseline single-injection at A50

The model fitted for the single-injection (Figure 5.3), shows that entrainment and diffusion factors have significant effect and premixed factor has almost no effect.

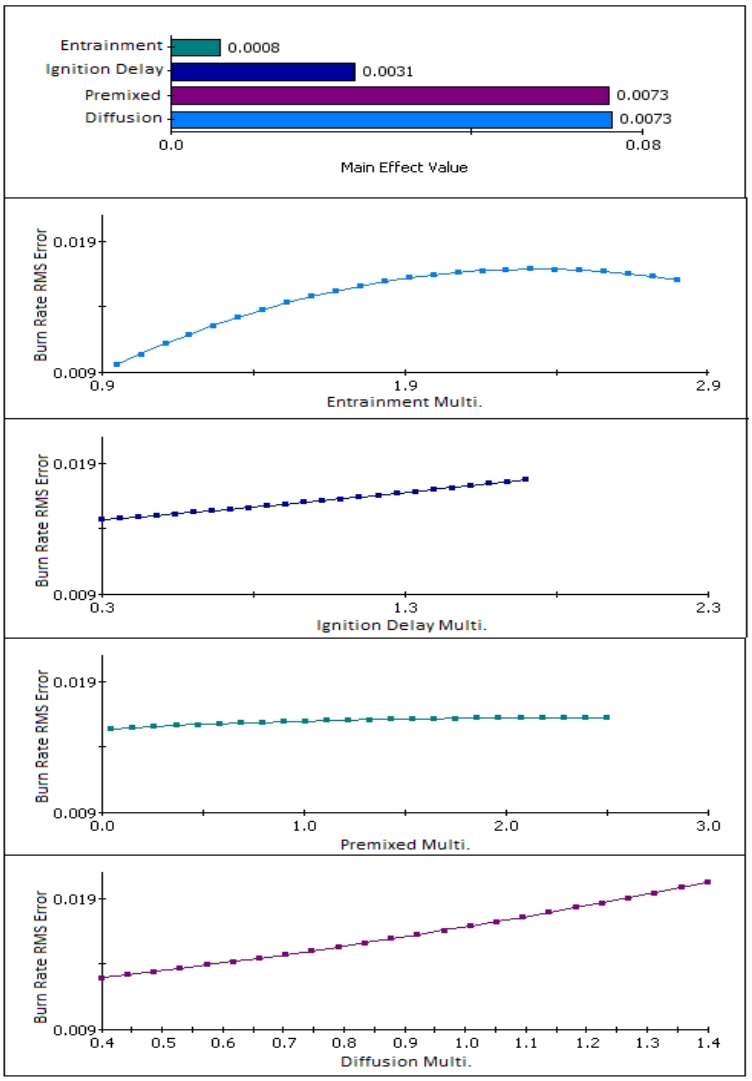


Figure 5.3: DOE Latin Hypercube results, single injection diesel-only mode

5.2.2 Advanced Direct Optimiser (ADO)

The non-gradient search algorithm methods can be divided into two main categories: metaheuristic and deterministic. While metaheuristic algorithm runs the optimisation using random numbers, deterministic optimisers are repeatable with no randomness. Thus, deterministic techniques are suitable for local optimisations while metaheuristic method suits global optimisations [GT (90)].

The Advanced Direct Optimizer (ADO) within GT-Power, contains one metaheuristic search algorithm, named “NSGA-III” and two simpler deterministic algorithms, “Discrete-Grid” and “Brent Method”. The Discrete-Grid algorithm is a fast simple bisection method that repeatedly bisects the search space and then selects the subinterval in which to keep searching. Brent Method is a root-finding tool that combines three methods of bisection, secant and inverse quadratic interpolation. This gradient-free method runs much faster than the Discrete-Grid with capability of finding optimums in fewer iterations. Applying both these methods on diesel-only (no pilot) combustion in A50, it was found the Discrete-Grid very poor and divergent in same number of iterations, Figure 5.4. Indeed, none of four multipliers of DIPulse could be converged.

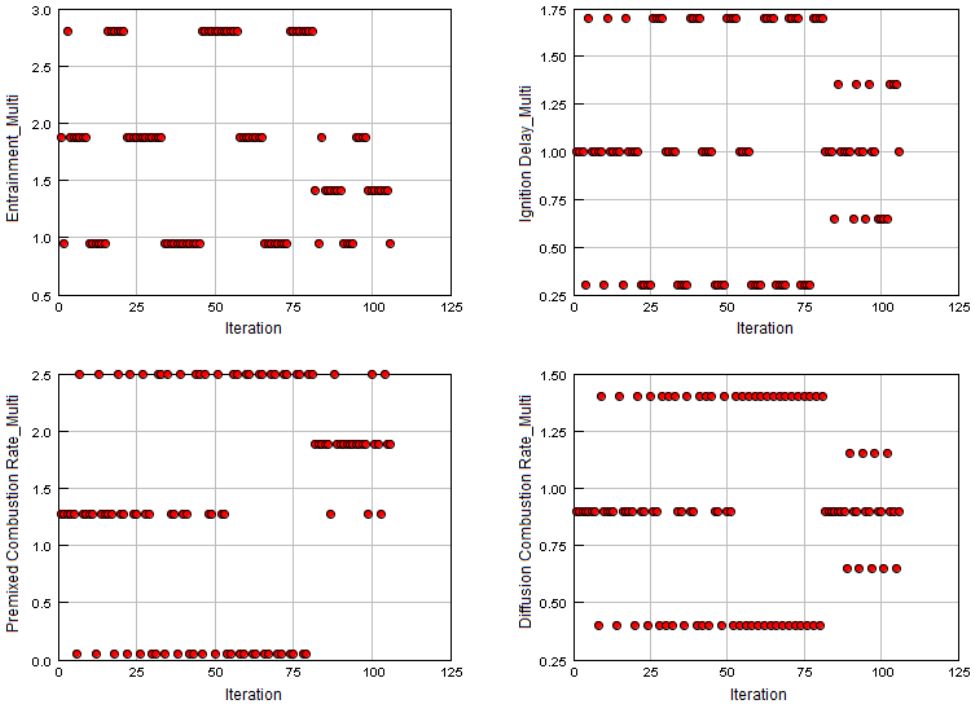


Figure 5.4: Discrete-Grid Optimising of DIPulse, single injection diesel-only combustion in A50

Brent optimisation of DIPulse over the same operating condition shows relatively powerful performance in converging the DIPulse multipliers, Figure 5.5.

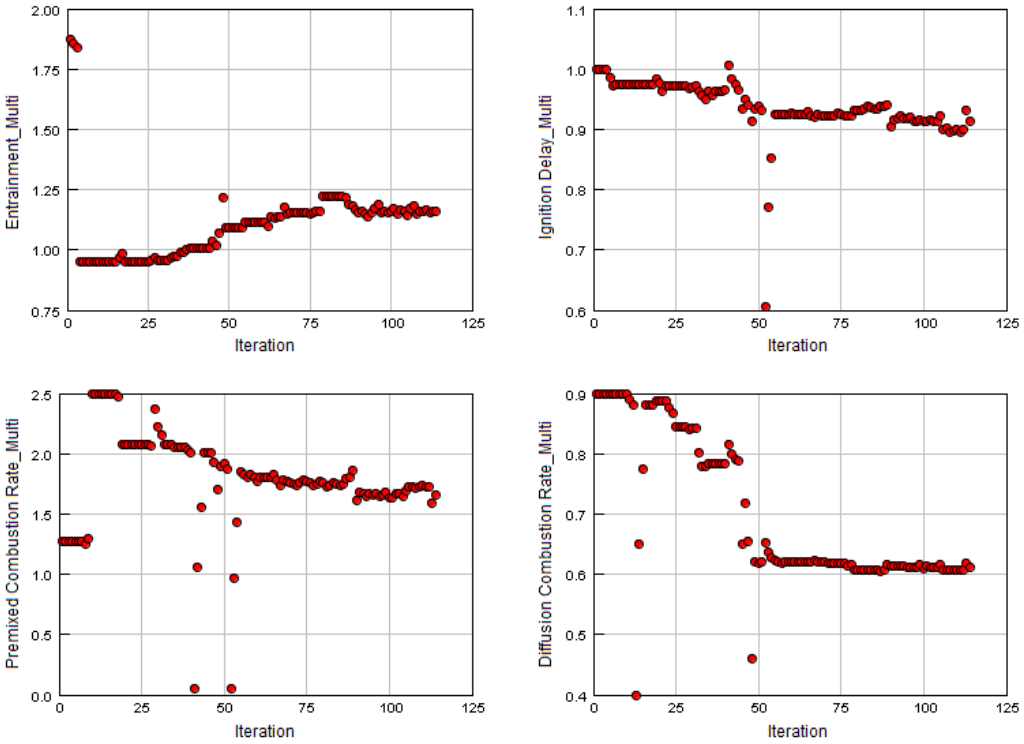


Figure 5.5: Brent Optimising of DIPulse, single injection diesel-only combustion in A50

The study of allocating the output uncertainty of a mathematical model to different sources of uncertainty in its inputs is called Sensitivity Analysis. This analysis has some advantages such as follows [Sensitivity Analysis (91)]:

- The relationships between output and input variables of a model can be understood better.
- The model inputs which result in major output uncertainty are specified.
- By identifying and removing the inputs with no effect on output, the model can be simplified.
- The optimum values of input factors can be found.

The most conventional methodology comprises altering one-factor-at-a-time (OFAT) to evaluate its effect on the output by linear regression or partial derivatives. Hence, in case of model failure, the responsible factor can be identified at once however the interaction among input factors cannot be detected.

The Burnrate RMS alteration for two optimisation methods of Brent and Discrete-Grid is presented in Figure 5.6 along with their sensitivity analysis of DIPulse multipliers. While the Burnrate RMS for Discrete-Grid was being dodging, it was converged acceptably to value of 0.0028 for Brent method. Nevertheless, both methods present approximate similar sensitivity analysis results.

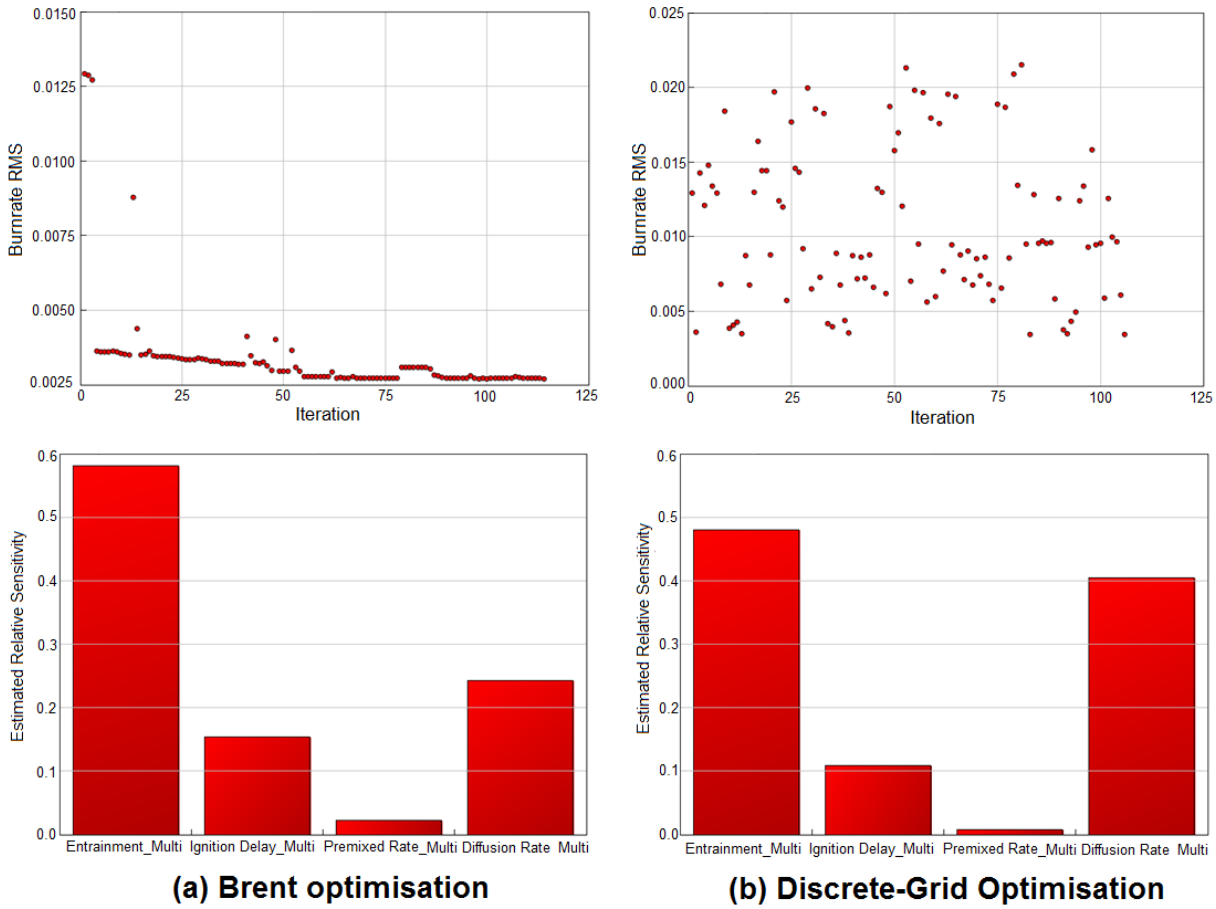


Figure 5.6: Burnrate RMS optimising and sensitivity analysis results:(a) Brent (b) Discrete-Grid, single injection diesel-only combustion in A50

According to the characteristics of third search algorithm method, NSGA-III, it is recommended for problems with medium to high complexity such as the calibration of predictive combustion constants. The NSGA-III which has been explained in detail in [Deb et al. (92)], is more robust and intelligent than two other algorithms. Its two key inputs required from the user are the population size and the number of generations to run. Multiplying these two inputs yields the total number of iterations that the optimizer will

run. The population size should generally increase as the number of independent variables increases, where the counting of the independent variables, n, should be as follows:

n = (number of "Independent" variables) × (number of active cases) + (number of "Sweep" variables) (5.1)

An "Independent" variable is one where a different optimal value may be found for each case or operating point. A "Sweep" variable is one for which the optimizer will find a single optimal value with respect to all cases.

The genetic algorithm has five parameter settings: population size, crossover rate, mutation rate, crossover rate distribution index and mutation rate distribution index. Although the best choice of population size will depend on the particular problem and should be considered in conjunction with the number of generations, the following table can serve as an initial recommendation.

Table 5.2: Recommended population size for NGSA-III optimiser [GT (90)]

n	Population size
3	10
4	16
5	20
6	26
7	30
8	40
9+	50

Crossover rate range for the genetic algorithm is between 0 and 1 with recommended value of 1. With aim of preserving the diversity, mutation changes the gene value of algorithm chromosomes in same way of biological mutation. Hence, the mutation rate should be considered too low to avoid primitive random search. The recommended value for mutation rate equals 1/n. Crossover rate distribution index and mutation rate distribution index both determine the spread of offspring solutions with range of 10 to 100. Larger values are more likely to create solutions nearer to the parents whereas smaller values lead to a more diverse search. Recommended value for these parameters is 15. The typical settings for the NSGA-III optimiser with recommended values of parameters can be seen in Figure 5.7.

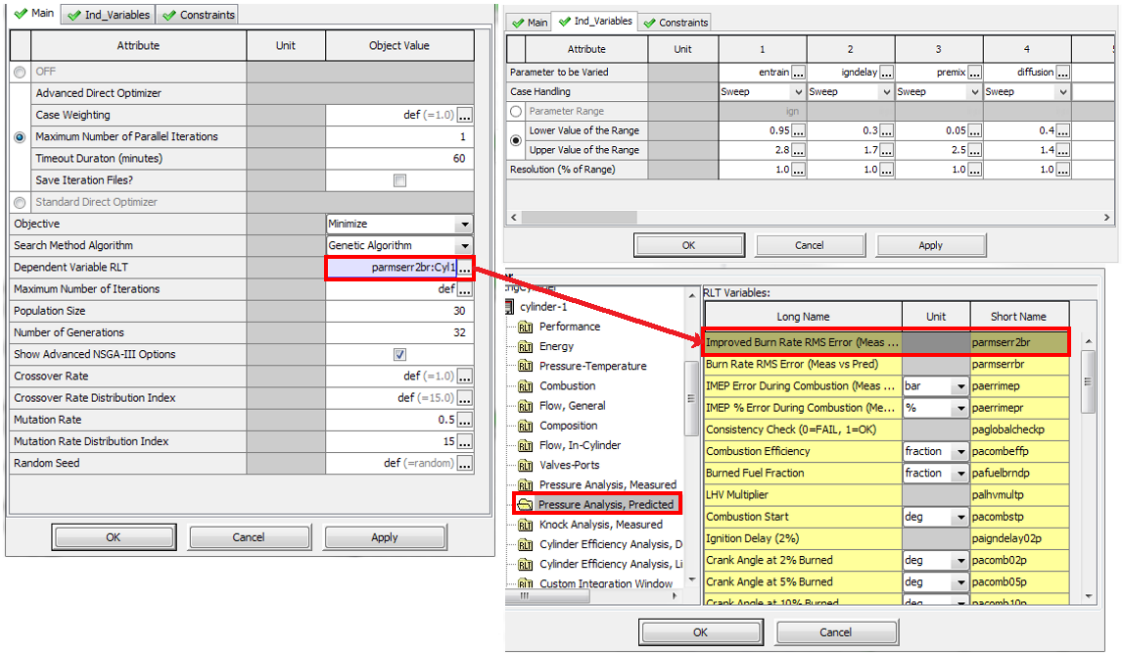


Figure 5.7: Typical settings for NGSA-III optimiser [GT (63)]

The optimisation results of NSGA-III optimiser is seen in Figure 5.8. It is worthwhile to mention that the number of iterations of this optimiser is much more than the other previous optimisers with longer run time for each iteration which results in much higher time consuming total run time (approx. 1 or 2 hours with Core i7 CPU speed).

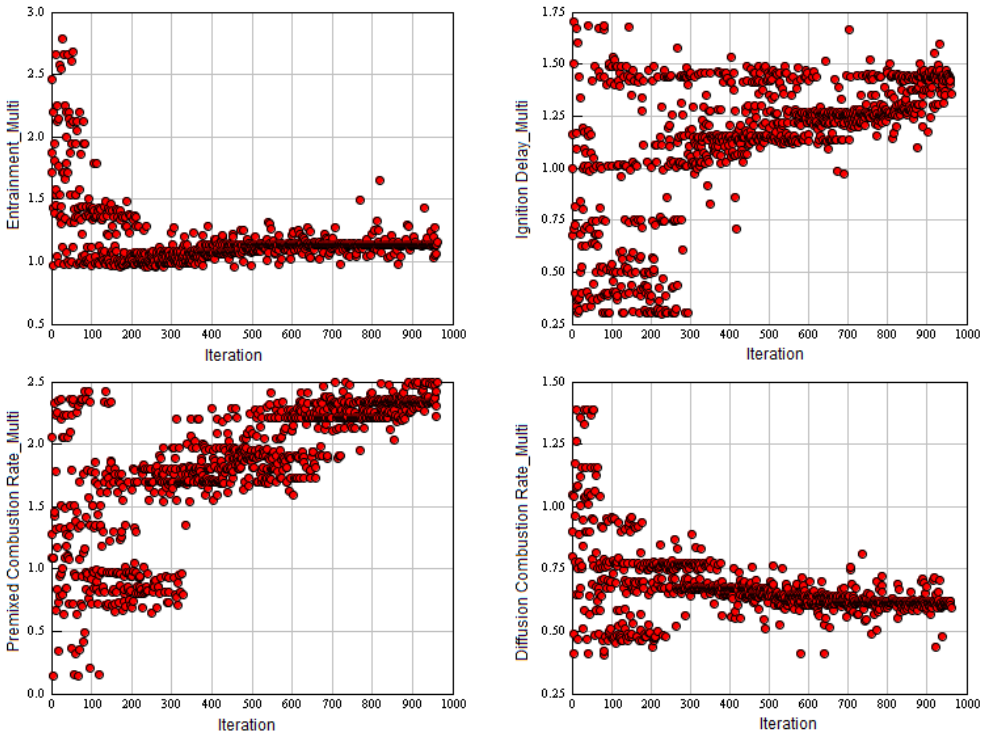


Figure 5.8: NSGA-III optimisation result of single injection diesel-only in A50

The cylinder pressure estimation of optimum values for DIPulse multipliers (Table 5.3) is presented in Figure 5.9. As seen, there is excellent agreement between measured pressure trend and the trend predicted by the optimised DIPulse model.

Table 5.3: Optimised DIPulse multipliers by NSGA-III (single injection diesel-only in A50)

DIPulse multiplier	**Value**
Entrainment Rate	1.16
Ignition Delay	1.36
Premixed combustion Rate	2.49
Diffusion Combustion Rate	0.59

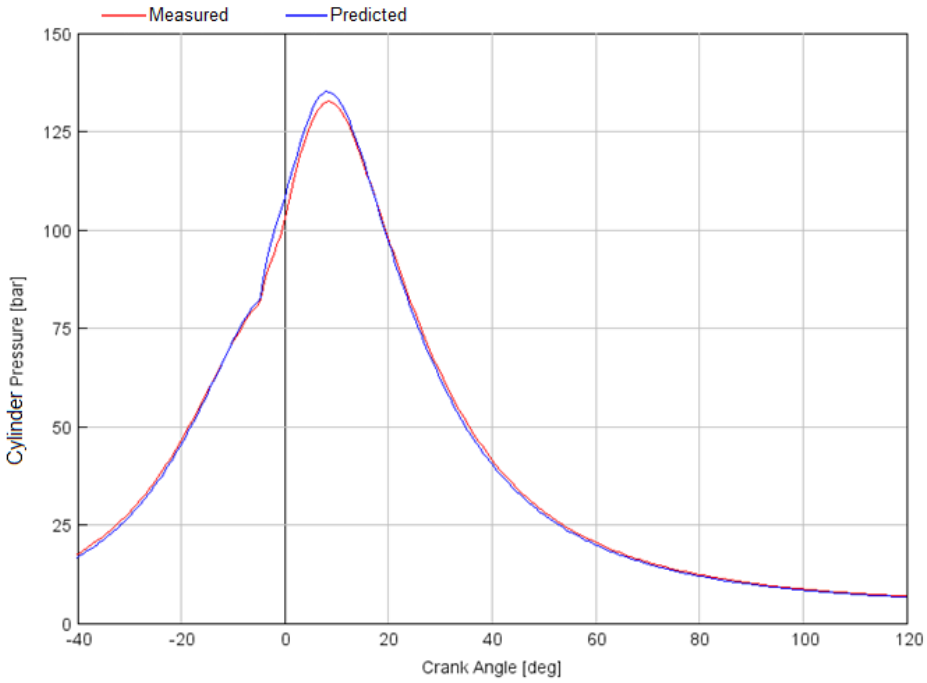


Figure 5.9: Cylinder pressure estimation by DIPulse optimised by NSGA-III (single injection, diesel-only in A50)

While NSGA-III solution converges slower than Brent method, it presented the similar sensitivity analysis (Figure 5.10) as the Brent optimiser except for premixed combustion rate and ignition delay multipliers.

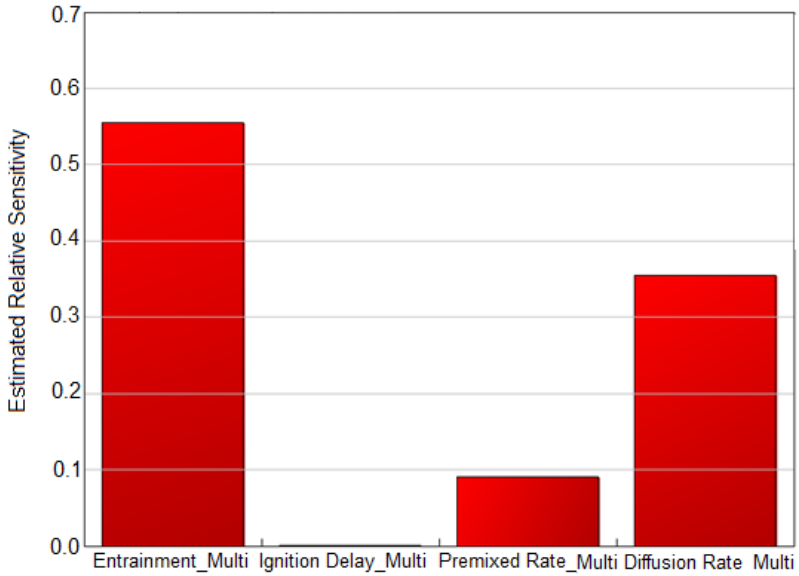


Figure 5.10: Sensitivity analysis: NSGA-III optimisation, single injection diesel-only in A50

Two multipliers of entrainment and diffusion combustion rate were found as the most dominant factors of DIPulse model. Taking only these two multipliers as the independent variables for NSGA-III optimiser, results in an output contour for burnrate RMS as seen in Figure 5.11:

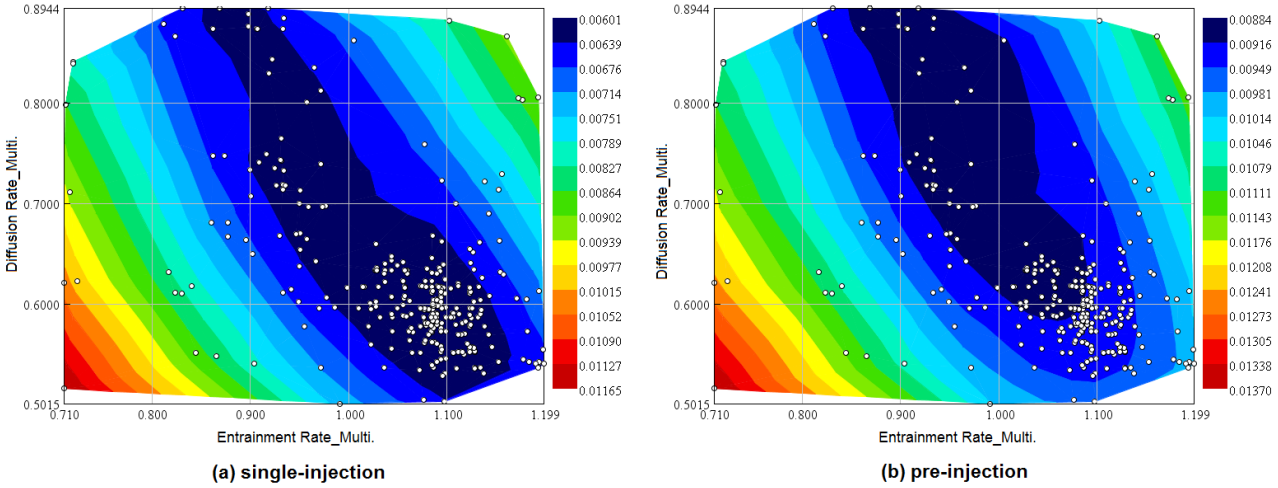


Figure 5.11: Burnrate RMS contour in terms of entrainment and diffusion multipliers: (a) single-injection (b) pre-injection diesel-only at A50

From the contour the area, it can identified where the minimum burnrate RMS is achieved (dark blue area). The minimum burnrate RMS for single-injection was 0.00601 while it was 0.00884 for pre-injection case. Since this area has been the most populated area for

optimiser iterations, the best-fit ranges for these multipliers for each case can be declared as follows:

Single-injection:

$$1.0 \leq \text{Entrainment rate Multi.} \leq 1.15$$

$$0.55 \leq \text{Diffusion rate Multi.} \leq 0.65$$

Pre-injection:

$$1.0 \leq \text{Entrainment rate Multi.} \leq 1.10$$

$$0.60 \leq \text{Diffusion rate Multi.} \leq 0.65$$

Hence, the entrainment rate for pre-injection is slightly increased due to advancing the SOC. Overall, it can be concluded that single-injection can be optimised better than pre-injection resulting in better combustion correlation with less burnrate RMS.

5.3 DIPulse genetic optimisation results

Initially, DIPulse combustion was chosen for correlating diesel-only and dual-fuel H2-diesel combustion within GT-Power. Using the NGSA-III optimiser, DIPulse multipliers were optimised with the aim of minimising the Burnrate RMS. The outputs of the optimised model is seen in Figure 5.12. While diesel-only (H0) case was perfectly correlated by optimised DIPulse in both P_{cyl} (cylinder pressure) and burnrate, DIPulse capability in dual-fuel modelling has been harmed by increasing hydrogen fraction as P_{cyl} and burnrate are not calibrated well.

In conclusion, DIPulse is not able to calibrate high HF% as the premixed part of dual-fuel combustion was highly dominant. This has been certified by results shown in Figure 5.12 and the burnrate RMS indicator. Therefore, a more robust model for dual-fuel combustion modelling was required, which will be explained in detail in next sections.

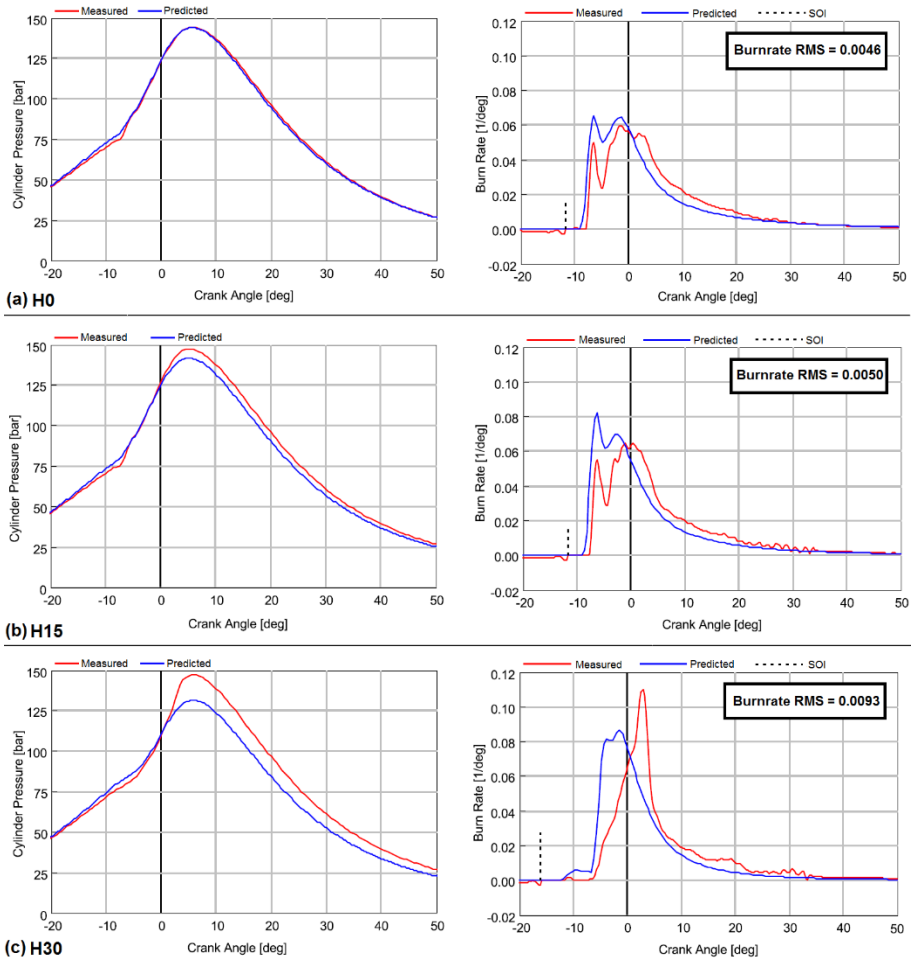


Figure 5.12: Calibrated DIPulse RLTs: (a) H0 (b) H15 (c) H30 at A50, single-injection

5.4 Dual-fuel modelling results

5.4.1 Calibrating the dual-fuel combustion by GT "DI-Wiebe" model

Using a three-term Multi-Wiebe function, the "DI-Wiebe" model executes the burn rate for direct-injection diesel engines; i.e. the superposition of three normal Wiebe curves. These Wiebe curves estimate the characteristic shape of a DI compression ignition, single main injection burn rate. The objective of using three functions is to facilitate the modelling of the premixed and diffusion sections of the combustion process. In case the measured cylinder pressure is not available, this model implements the burn rate based upon user input.

For evaluation of the DI-Wiebe model, the estimated burn rate with manually-adjusted constants was compared with measured burn rate in three HFs over A50 operating point (selected experimental points mentioned in Section 4.2.2).

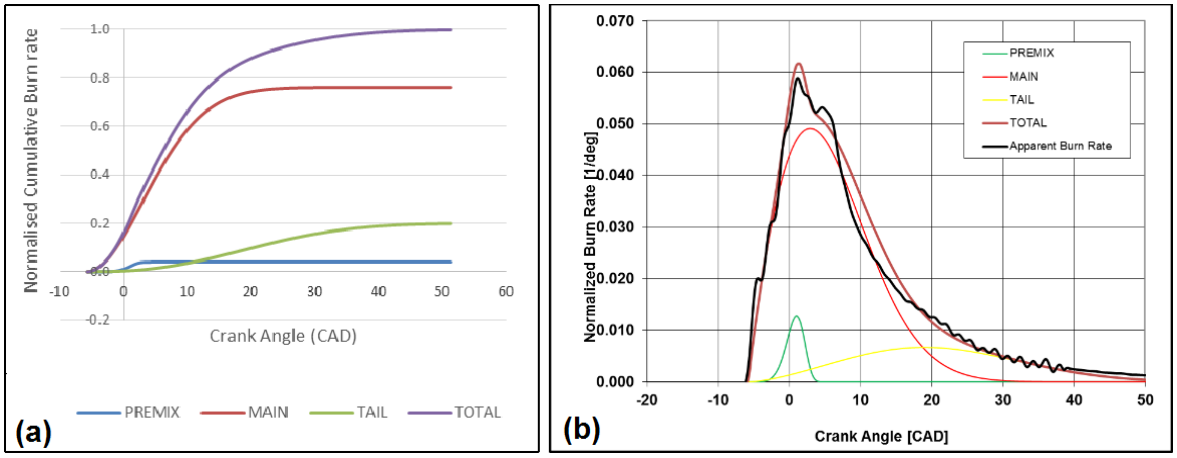


Figure 5.13: DI-Wiebe vs measured burn rate, **H0** at A50 (a) cumulative (b) normalised burn rate

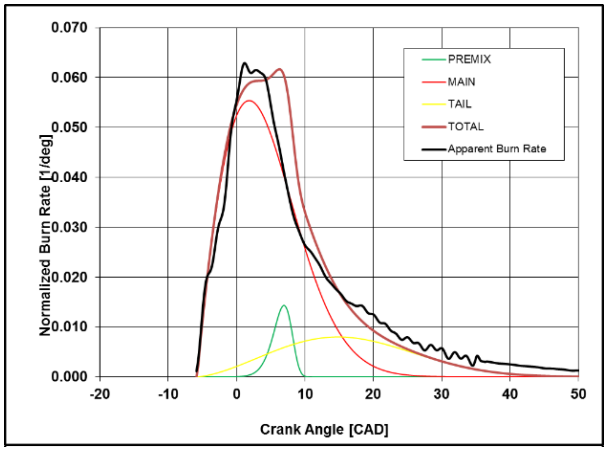


Figure 5.14: DI-Wiebe vs measured burn rate, **H15** at A50

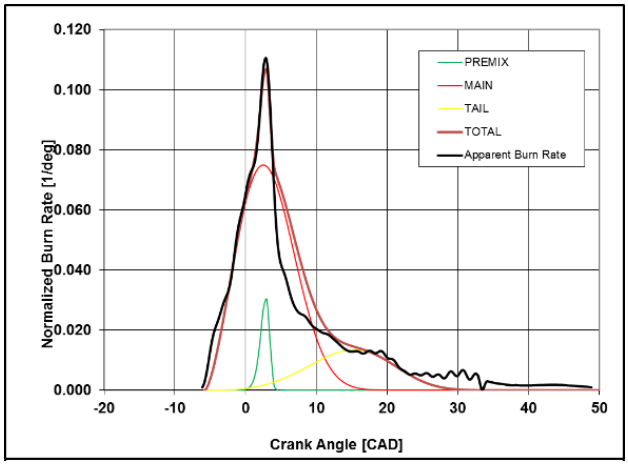


Figure 5.15: DI-Wiebe vs measured burn rate, **H30** at A50

Table 5.4: DI-Wiebe constants for three HFs: H0, H15 and H30 at A50

Input	H0	H15	H30
Ignition delay	3 deg	3 deg	3 deg
Start of injection	-8.75 CAD	-8.75 CAD	-8.75 CAD
Premixed Fraction	0.04	0.05	0.05
Main Fraction	0.76	0.75	0.75
Tail Fraction	0.20	0.20	0.20
Premixed Duration	5 deg	5 deg	2 deg
Main Duration	16 deg	14 deg	10 deg
Tail Duration	30 deg	25 deg	15 deg
Premixed Exponent	5	9	14
Main Exponent	0.91	0.9	1.5
Tail Exponent	1.5	1.5	3

As seen in Table 5.4, the contributions of each section of DI combustion are in accordance with the conventional amounts suggested in [Heywood (7)]. The premixed section is mostly altered by various hydrogen substitution rates. Bearing in mind, the boost pressure was kept fixed during hydrogen enrichment, the oxygen concentration would be reduced. Despite this fact, the burn rate is faster in higher HFs. This reflects that higher H2 concentration has caused pre-ignition which resulted in more rapid premixed section. Also, the main section is shortened by adding H2 since less diesel fuel is burned in form of diffusion combustion. The tail duration is constantly decreasing by increasing H2 fraction, representing the shorter overall combustion duration.

In addition to the fact that Wiebe function works just in zero-dimensional computations, the physical and chemical conditions are not properly represented as combustion duration needs to be known beforehand. Hence, the quasi-dimensional or phenomenological models are proposed here with aim of more detailed investigation of combustion reactions within ICEs.

5.4.2 DIPulse multipliers characterisation

After obtaining optimised DIPulse multipliers using the optimisation solution, the best-fit results could be achieved by manual tuning the constants. Hence, their influence on the cylinder pressure and burn rate was observed beforehand. Each DIPulse factor (except

premixed rate multiplier) was changed from “0.5” to “1.5” with 0.25 increment while all other ones was set to “1”. The aim is to show the sensitivity of cylinder pressure and burn rate to each factor variation.

1. Entrainment multiplier:

The higher value results in higher burn rate in shorter duration. This is depicted in Figure 5.16 and Figure 5.17 where CA50 (combustion timing) got advanced and CA10-CA90 (combustion duration) got shortened dramatically. In addition, the peak in-cylinder pressure was risen by increasing entrainment. Hence, the entrainment factor has a significant effect on the combustion process.

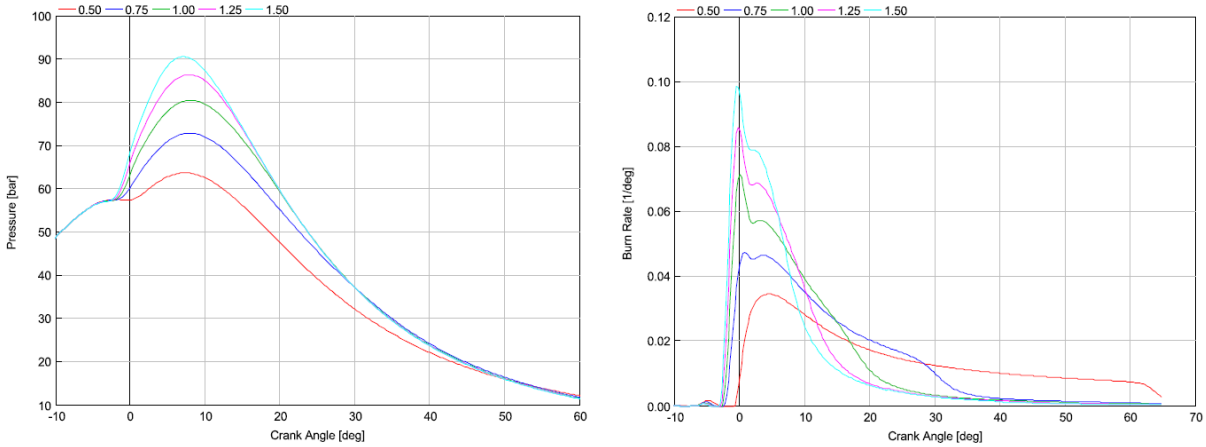


Figure 5.16: Entrainment multiplier value sweep

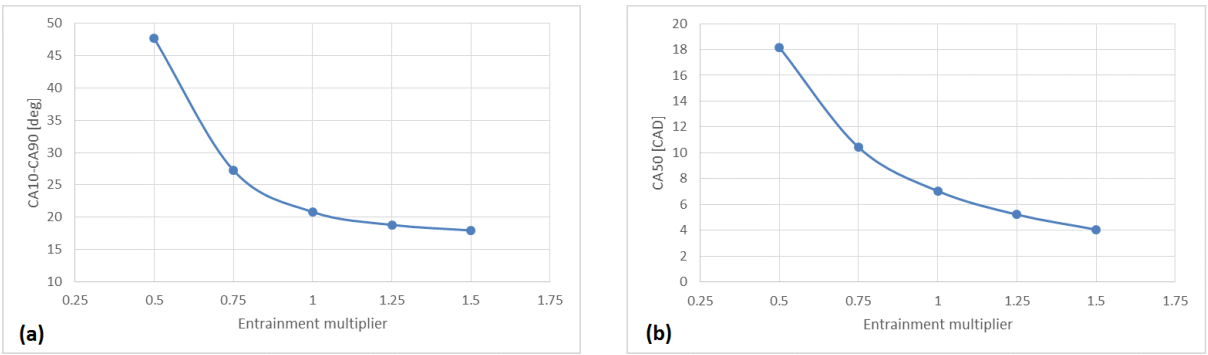


Figure 5.17: Entrainment multiplier effect on combustion: (a) duration (b) timing

Regarding the entrainment part of the DIPulse model, breakup time of spray into droplets (t_b) is a turning point in the spray penetration length (Eq. 3.20). Since t_b depends on nozzle geometry (d_n: diameter & C_d: coefficient of discharge), these elements must be specified.

According to the technical specs of test engine, $\mathbf{d_n}$ = 0.176 mm (x8 nozzle holes). In order to evaluate effects of $\mathbf{C_d}$, it was introduced as a case parameter (Cd_nozzle) within the model's injector, "InjMultiProfileConn" when DIPulse was run. For instance, the predicted burnrate was compared by reducing Cd_nozzle from 0.7 to 0.4 (Figure 5.18). burnrate is affected mainly in the entrainment part as $\mathbf{t_b}$ is lengthened. This effect assimilates the increase of ignition delay. Thus, since spray tip length and its velocity are directly proportional to Cd_nozzle, this attribute can be used for entrainment calibration.

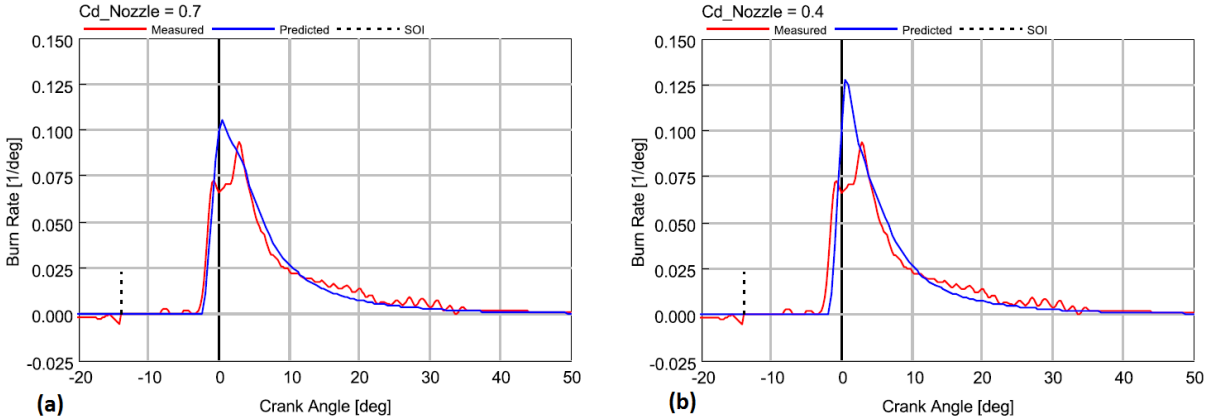


Figure 5.18: Cd_Nozzle effect on burnrate: H0 at A25, Cd_Nozzle = (a) 0.7 (b) 0.4

2. Ignition delay:

The time elapsed between fuel injection and SOC (ignition delay) has direct proportionality with this factor. As higher value allows more fuel to be agglomerated and then burn in a premixed mode, with the peak of premixed phase increased as shown in Figure 5.19. However, this has a relatively small effect on cylinder pressure.

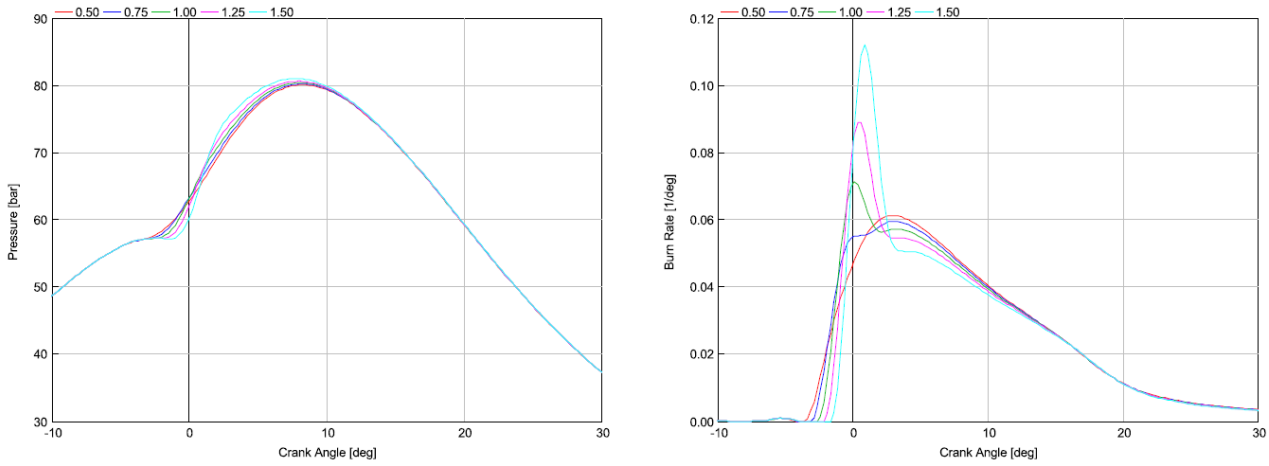


Figure 5.19: Ignition delay multiplier value sweep

3. Premixed multiplier:

The rate of premixed combustion is altered by this multiplier. The range of variating this factor was excluded from others due to very low sensitivity of cylinder pressure to this factor. As seen in Figure 5.20, the slope of premixed curve was just slightly increased with higher values of this factor.

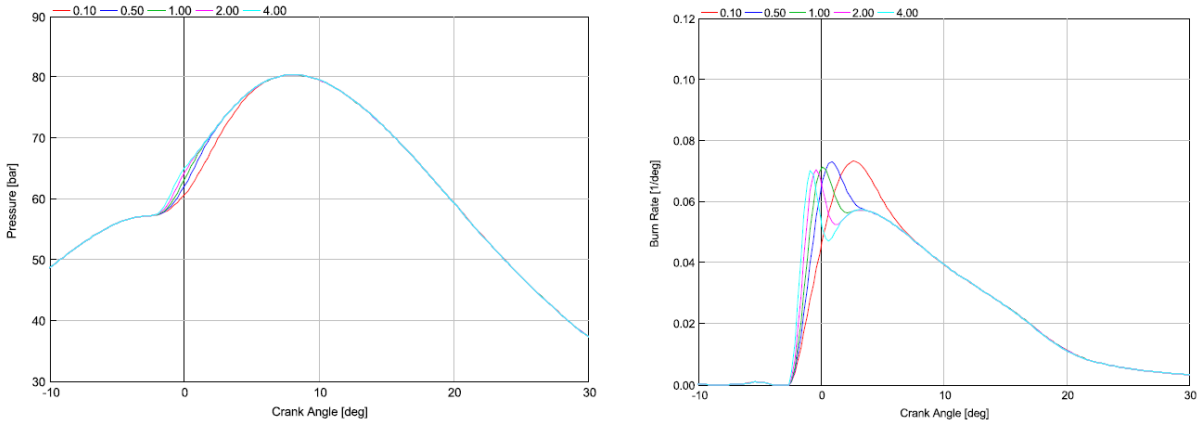


Figure 5.20: Premixed rate multiplier value sweep

4. Diffusion multiplier:

The rate of diffusion combustion (slope of the diffusion curve) and its curve peak will be increased with higher values of diffusion rate multiplier. Furthermore, the cylinder pressure peak was enhanced by increasing this multiplier, Figure 5.22.

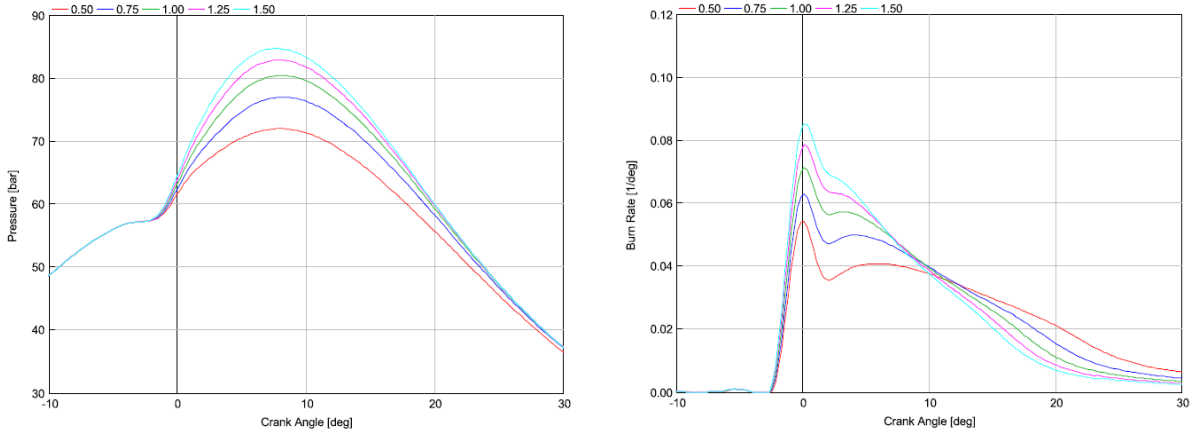


Figure 5.21: Diffusion rate multiplier value sweep

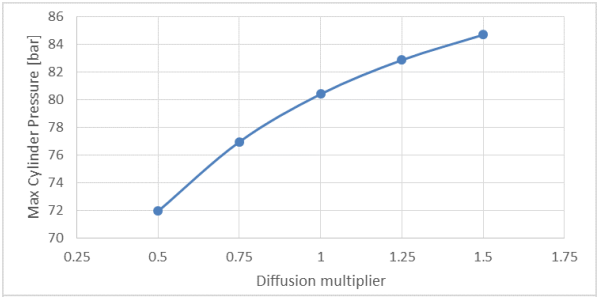


Figure 5.22: Max cylinder pressure vs diffusion rate multiplier

In conclusion, the DIPulse multipliers effect can be characterised as follows:

- DIPulse model tries to individualise the combustion sub-processes with minimum effects on each other. However, this is not in accordance with what exactly happens in reality.
- Entrainment and ignition multipliers have inverse effect, both are adjusting the first premixed curvature. As ignition delay is increased, the premixed peak will be enhanced and it is reverse for entrainment multiplier.
- As premixed multiplier (less than 1) is reduced, the burn rate will be prone to the diffusion rather than premixed; hence, a single-humped burn rate curvature will result.
- If diffusion multiplier increases, both premixed and diffusion humps will be enhanced but in case of reduction, just the diffusion hump will lower.
- As premixed multiplier has very slight effect on burn rate and almost no effect on cylinder pressure, it can be neglected. (set to “1.0” value.)
- While cylinder pressure has not been affected by either ignition delay or premixed multipliers, it is directly proportional to the entrainment and diffusion very significantly.

5.4.3 SITurb multipliers characterisation

The accuracy of the turbulent entrainment model proposed in GT, depends on the precision of calculations for: (1) projected flame area, (2) laminar burning velocity and (3) turbulent burning velocity. Nevertheless, the current GT turbulent entrainment model is not comprehensive. It ignores the effects of “de-developing” turbulence (reduction of turbulence scale by approaching the cylinder wall) and does not directly account for thermo-diffusive effects.

Since large set of experimental data (pressure, burn rate and flame image) would be essential to derive a robust comprehensive predictive model, characterising the SITurb key multipliers with aim of calibrating this model was required. The baseline experimental data obtained from a gasoline single-cylinder engine were used for validation of SITurb model in this section.

Firstly, a sensitivity analysis of the SITurb multipliers for the test point of 4 bar IMEPn – 2000 rpm was done. The sweeping range for all SITurb multipliers were from 0.1 to 4.0 with unequal intervals in order to cover wide range of variations.

1. Turbulent flame speed multiplier (C_{TFS}):

This is the multiplier which has the direct relation with turbulent burning velocity. Hence, its higher values will accelerate combustion and increase heat release. It is also seen that predicted cylinder pressure is hugely magnified by increasing this multiplier. Thus, selecting this multiplier should be carried out with extra care; i.e. it has the highest relative sensitivity.

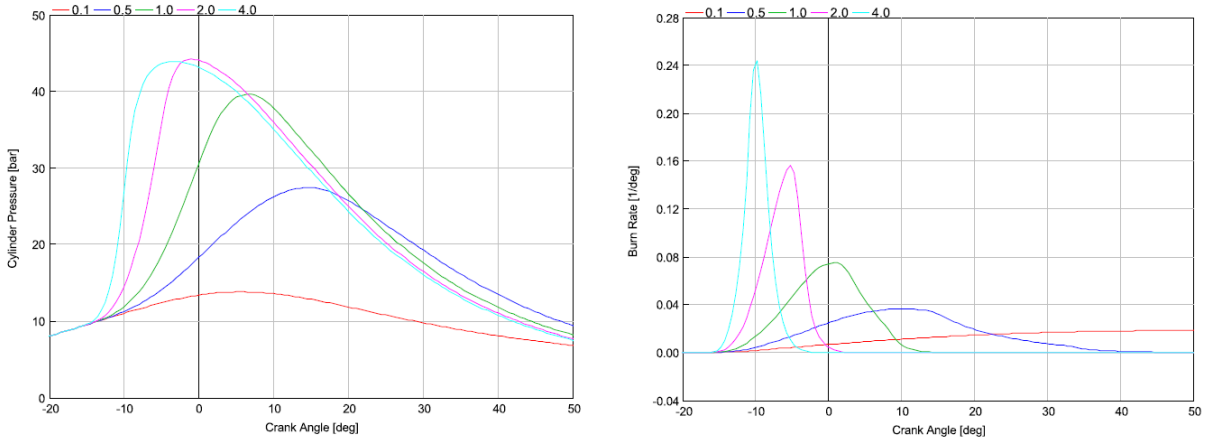


Figure 5.23: C_{TFS} value sweep – gasoline SITurb model

The effect of turbulent flame speed multiplier on the combustion duration and timing is seen in Figure 5.24. This trend is similar to effect of entrainment multiplier of DIPulse (Figure 5.17), since the combustion has been accelerated and advanced.

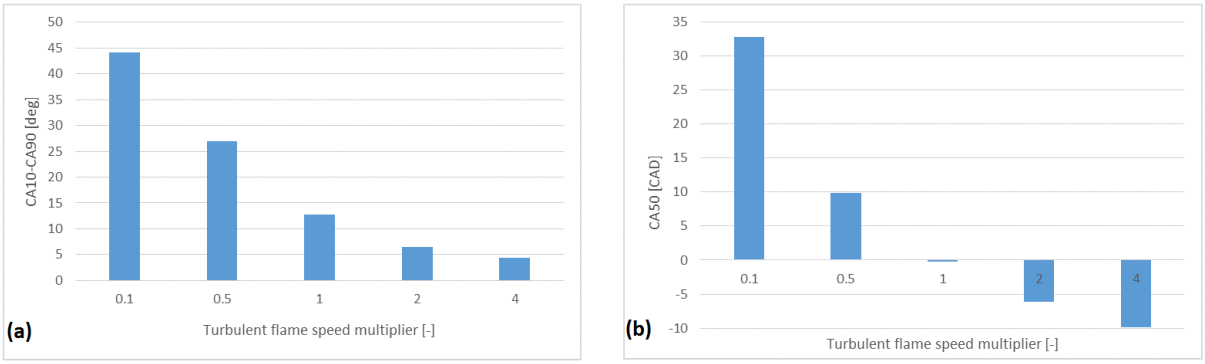


Figure 5.24: C_{TFS} effect on combustion: (a) duration (b) timing – gasoline SITurb model

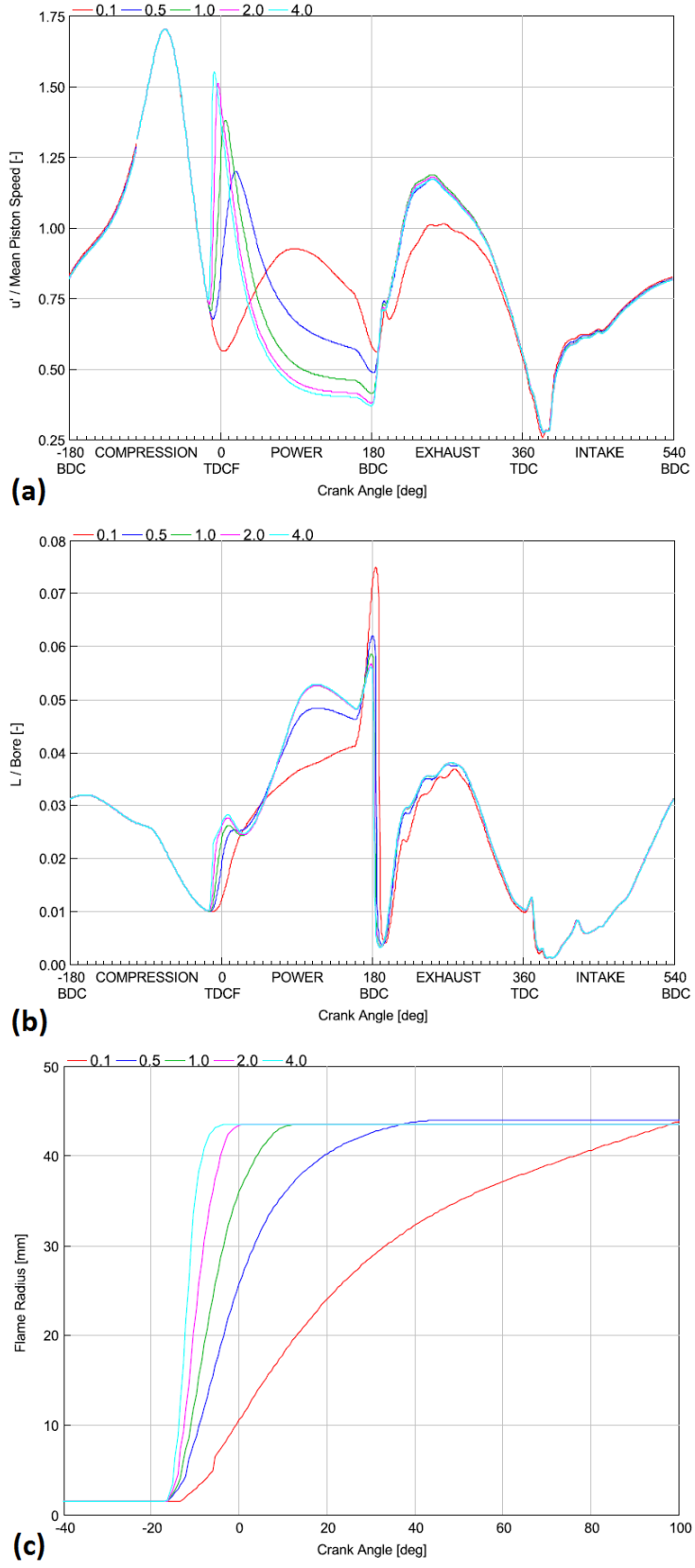


Figure 5.25: C_{TFS} value effect on turbulent parameters: (a) normalised turbulence intensity (b) normalised integral length scale (c) flame radius – gasoline SITurb model

In addition, C_{TFS} has significant effect on turbulent parameters. This effect has been mainly pronounced on turbulence intensity during combustion, as seen in Figure 5.25 (a). The integral length scale variance is reduced for the C_{TFS} values higher than unity. In addition, as expected, the higher values of C_{TFS} would accelerate the flame propagation according to Figure 5.25 (c).

2. Taylor length scale multiplier (C_{TLS}):

This multiplier scales the λ (Taylor length scale) and regarding Eq. (2.8), it is directly related to τ_b (burning time scale). In another word, the higher values of this parameter will lengthen the laminar burning and the total mass burning process. In fact, it has a swinging effect with turbulent flame speed multiplier. Nevertheless, the cylinder pressure and burn rate sensitivity to this multiplier is less than turbulent flame speed multiplier.

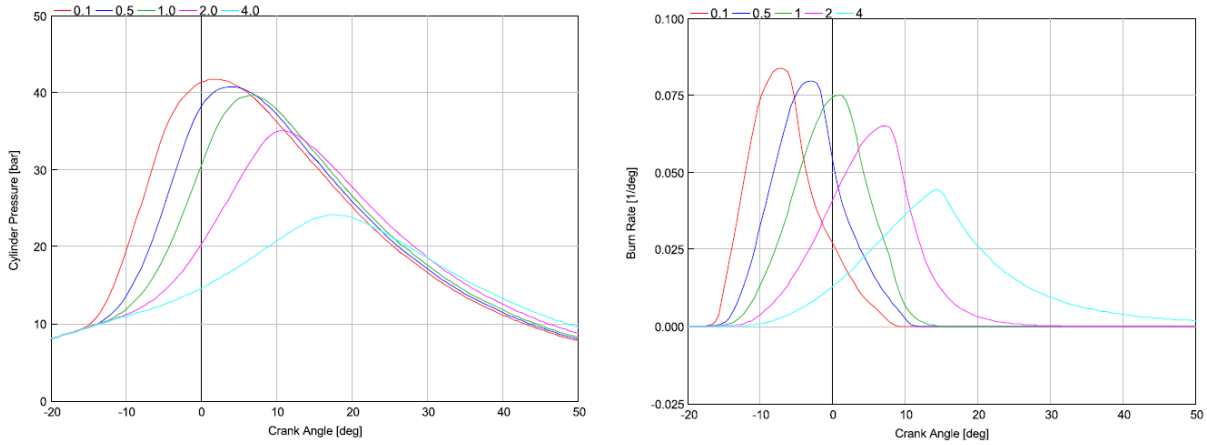


Figure 5.26: C_{TLS} value sweep – gasoline SITurb model

3. Dilution effect multiplier (C_{DE}):

This is the direct constant of proportionality within the laminar burning velocity equation (Eq. 2.9) which reflects the effect of residual burnt gas. Its effect on burn rate and cylinder pressure except in excessive values is not significant and it can only be applied for fine-tuning the predicted burn rate. It is observed that the values below unity for this multiplier are not too much effective and just higher values than unity are being influential. Since the EGR percentage was kept fixed during our testing, this multiplier can be set to "1" for all simulating cases.

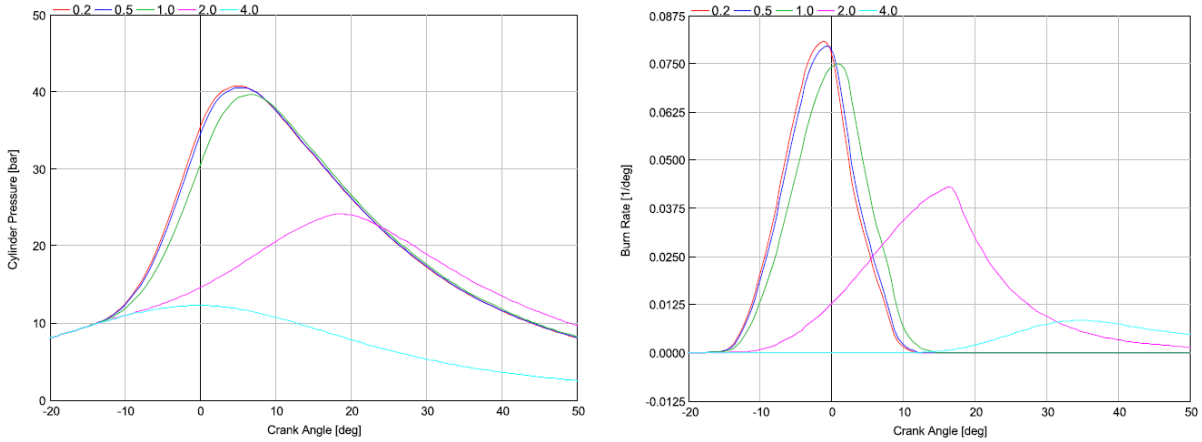


Figure 5.27: C_{DE} value sweep – gasoline SITurb model

4. Flame kernel growth multiplier (C_{FKG}):

This factor which is used as the multiplier of integral length scale within the equation for turbulent burning velocity (Eq. 3.28), has no major effect on either burn rate or cylinder pressure. The only exception is very low value of "0.1" which is not in our aim. Thus, it is set to "1" for all simulating cases.

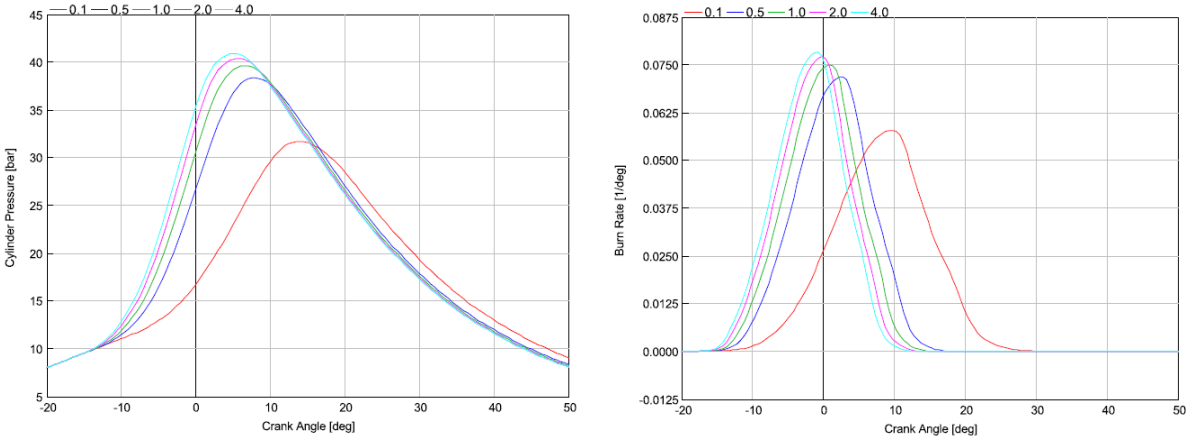


Figure 5.28: C_{FKG} value sweep – gasoline SITurb model

Thereupon the evaluation of SITurb multipliers sweeping on the specific operating point, it was concluded to utilise the C_{TFS} and C_{TLS} for initial prediction. Then C_{DE} and C_{FKG} were used for fine-tuning of burn rate prediction.

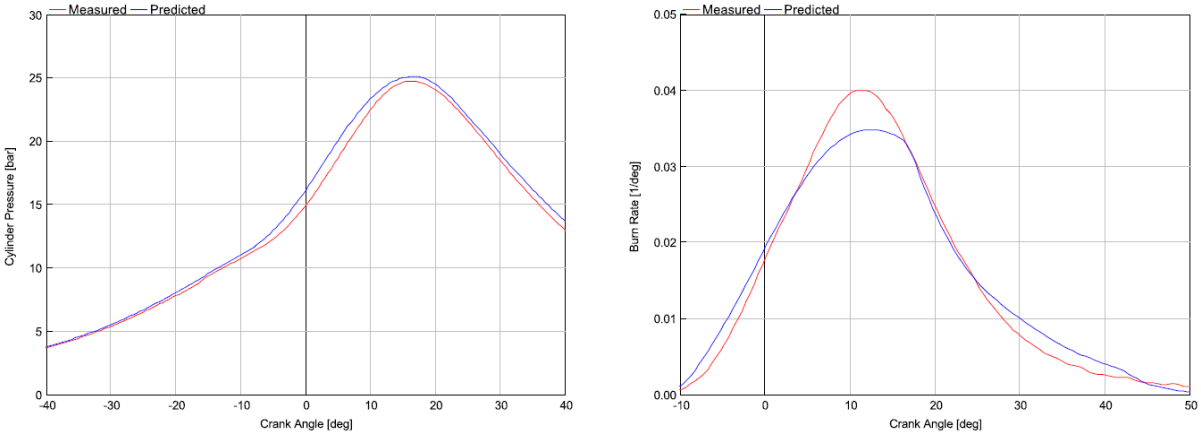


Figure 5.29: SITurb calibration results for pivotal point (4 bar IMEPn, 2000 rpm)

As seen in Figure 5.29, the cylinder pressure and burn rate were predicted in good agreement with the measured values. This has been also certified with the in-cylinder energy balance, Figure 5.30. The heat transfer and work are perfectly correlated. The only divergence is seen in internal energy from 20 aTDC afterwards.

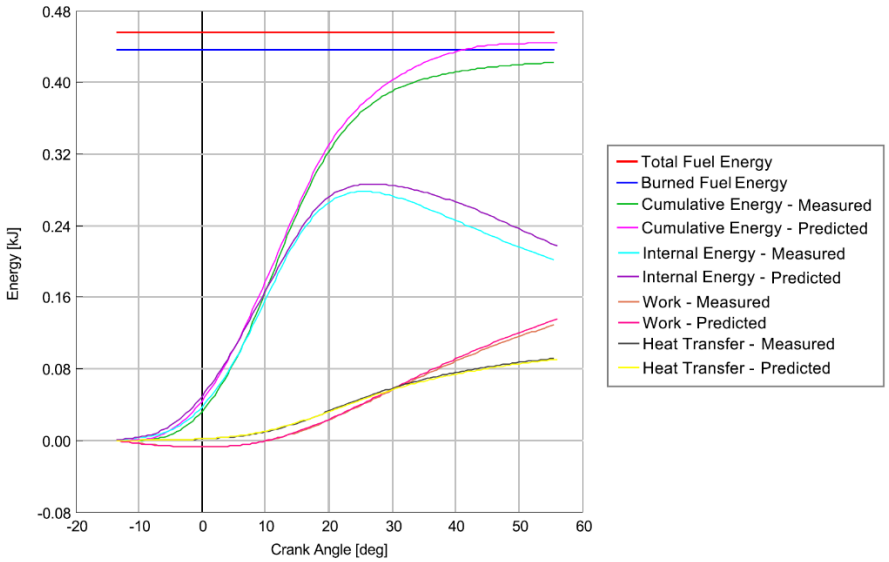


Figure 5.30: In-cylinder energy balance (2000 rpm – 4 bar IMEPn) – gasoline SITurb model

In Figure 5.31, the calculated laminar and turbulent flame speeds are presented. The trend of laminar burning velocity is justifiable with trend of in-cylinder temperature; while it was increasing in the first half until reaching the T_max crank angle, it would drop since piston is going down and temperature is mitigated. The turbulent burning velocity set to rise with spark ignition until TDC-firing where it falls down afterwards. This behaviour is in accordance with turbulent intensity trend depicted in Figure 5.25 (a).

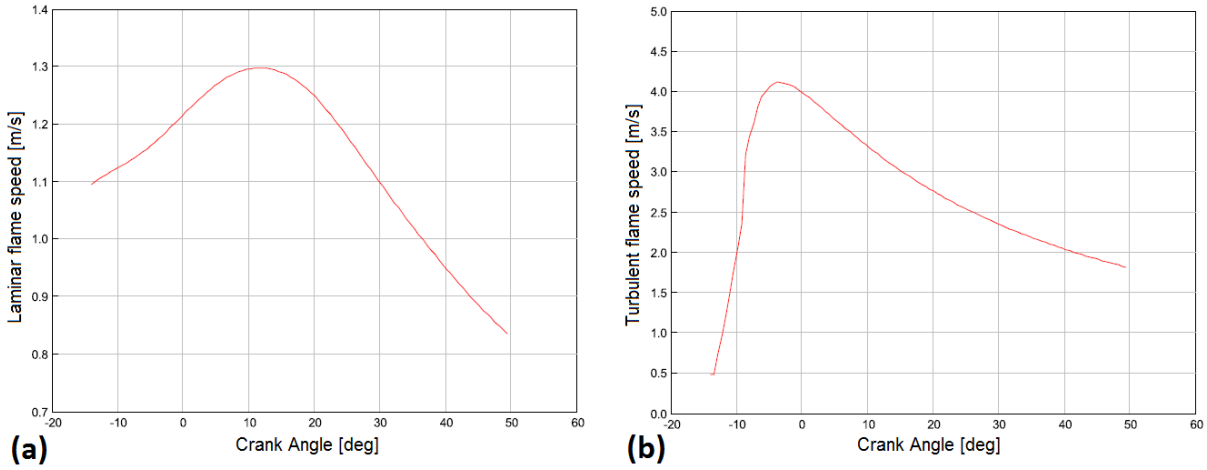


Figure 5.31: Calculated flame speeds: (a) laminar (b) turbulent (4 bar IMEPn, 2000 rpm)

The flame speed ratio (ratio of turbulent speed to laminar speed) can be seen in Figure 5.32. This is an index for evaluating the burn process.

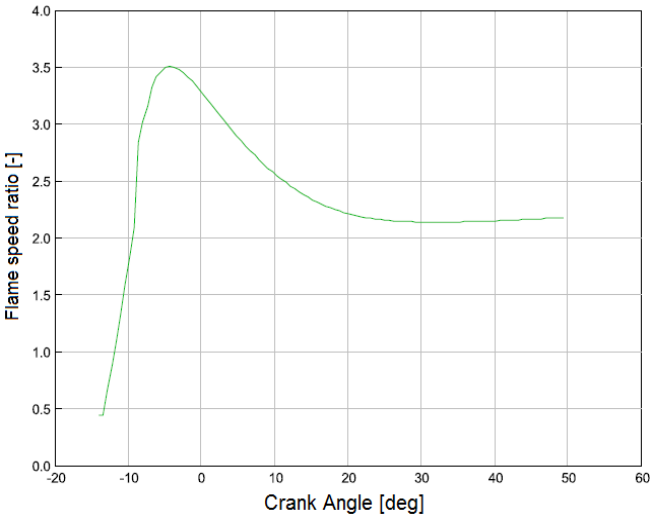


Figure 5.32: Flame speed ratio (4 bar IMEPn, 2000 rpm)

The calibration for the pivotal point paved the way for the calibrating the load swept points within 2000 rpm, starting from 2 bar to 10 bar IMEPn with 2 bar increment. During this calibration, all 3 factors: C_{TLS}, C_{DE} and C_{FKG} were kept fixed. Thus, the C_{TFS} was just altering in order to find the best-fit.

The results of cylinder pressure and burn rate validation for these points are presented in Figure A.1 and A.2 in the Appendix. As expected, the turbulent flame speed multiplier adjusted for swept loads increases in direct proportionality of load (IMEPn), Table 5.5. The fixed calibrating multipliers for all swept loads are presented in Table 5.6.

Table 5.5: Turbulent flame speed multiplier adjusted for all swept loads – gasoline SITurb model

IMEPn	C_{TFS}
2 bar	0.44
4 bar	0.51
6 bar	0.60
8 bar	0.67
10 bar	0.70

Table 5.6: Fixed calibrating multipliers for all swept loads – gasoline SITurb model

Multiplier	Value
C_{TLS}	0.6
C_{DE}	1.1
C_{FKG}	0.5

The flame speeds for the other 4 swept loads are presented in Figure 5.33. As expected turbulent burning velocity is enhanced by increasing the load. However, laminar burning velocity alteration in terms of load is a small effect.

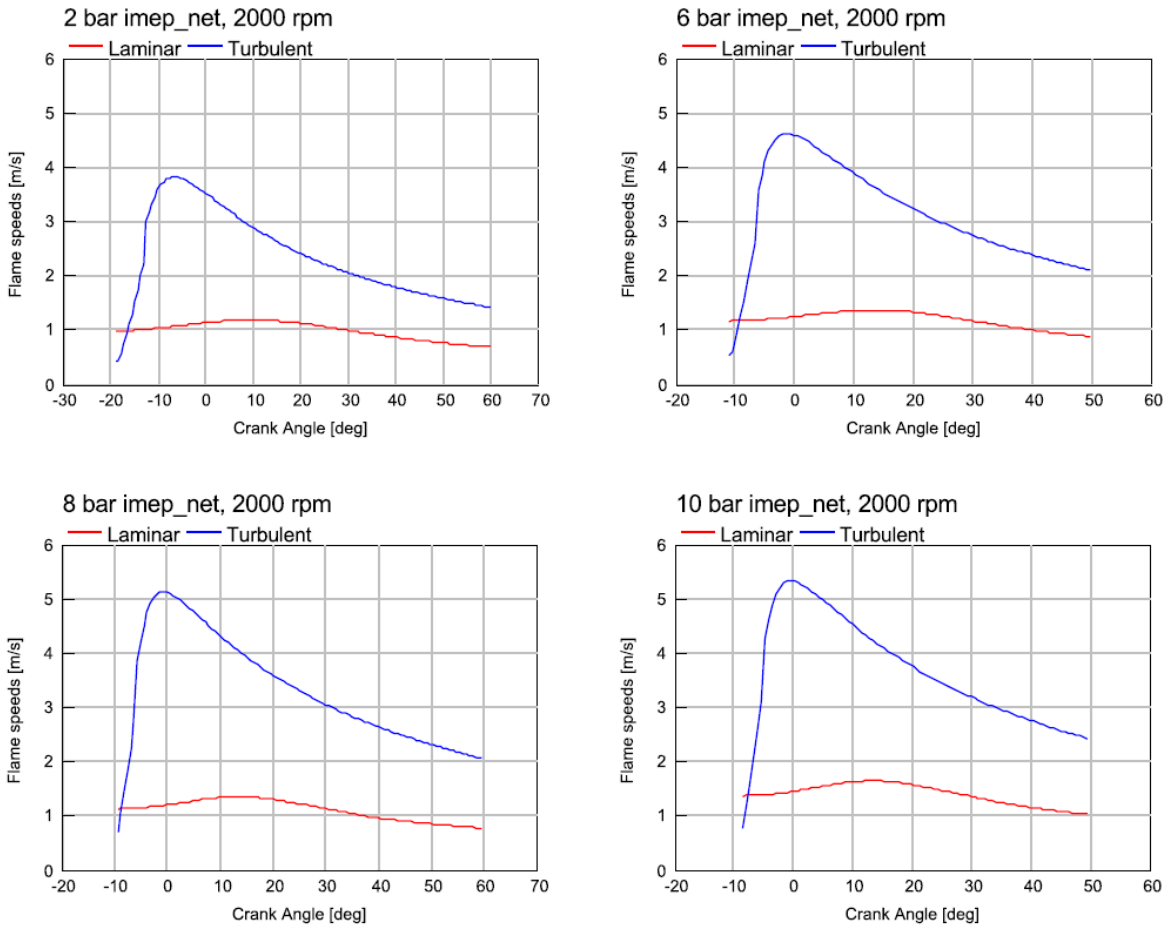


Figure 5.33: Flame speeds: 4 other swept loads – gasoline SITurb model

5.4.4 H2-Diesel “dual-fuel” modelling results

Following the DIPulse and SITurb characterisation, it was concluded the following influential multipliers for ‘DualFuel’ burn rate prediction in order of importance:

1. Diffusion multiplier
2. Entrainment multiplier
3. Turbulent flame speed multiplier
4. Ignition delay multiplier (featured by SOI)

Thus, it was attempted to achieve the best fit of dual-fuel model for simulating H2-diesel combustion in the A25 operating point in this section. The selected test cases for this simulation were the same as the cases selected in Section 4.2.1. The cylinder pressure and burn rate prediction by DualFuel model is presented at Figure 5.34 and 5.35. It was observed that measured curves for the cylinder pressure and burn rate are very similar for H0, H20 and H40. In H65, the highest ratio of hydrogen substituted has resulted in similarity of burn rate trend to the premixed (SI) combustion.

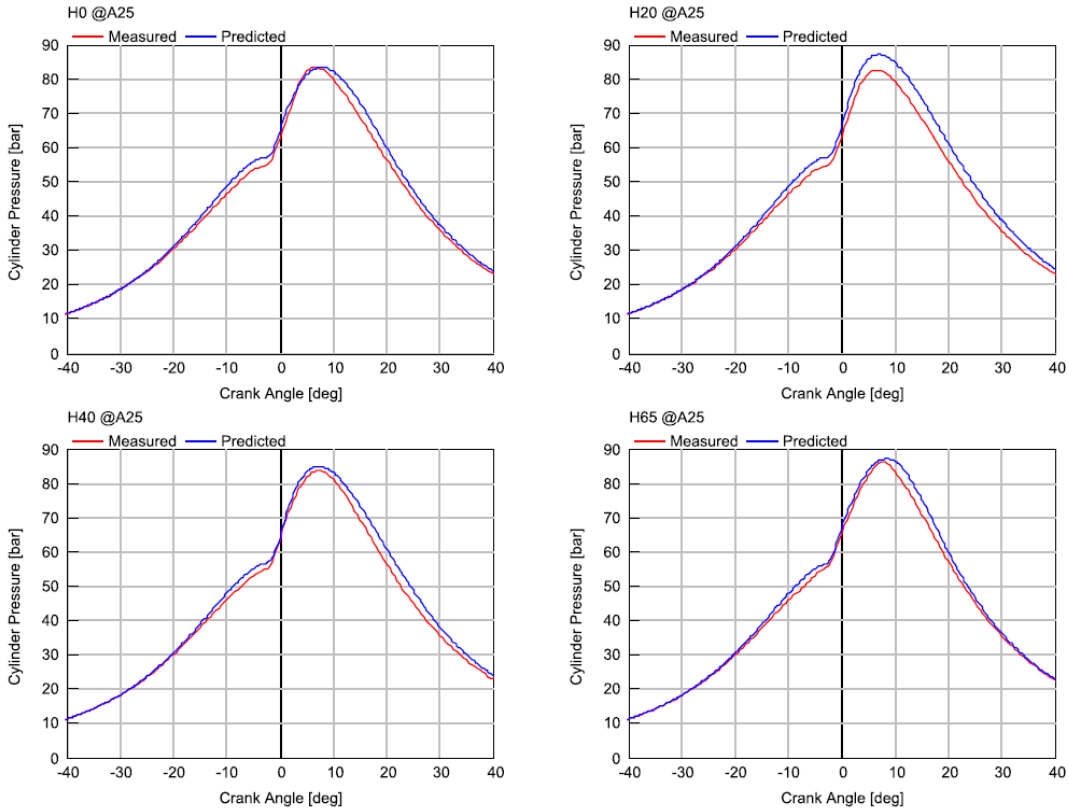


Figure 5.34: Cylinder pressure prediction at A25 - DualFuel model

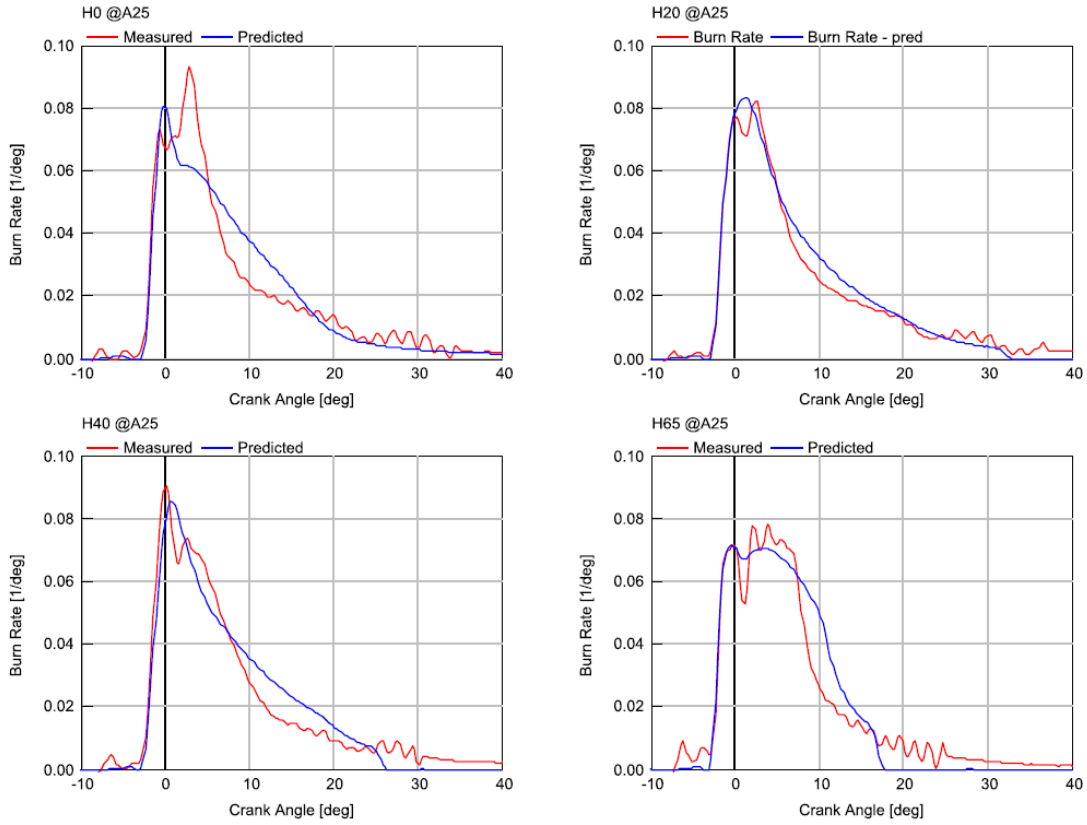


Figure 5.35: Burn rate prediction at A25 - DualFuel model

The behaviour of burn rate for these test cases can be judged by their corresponding calibration multipliers presented in Table 5.7:

Table 5.7: Calibration multipliers for prediction of selected test cases at A25 – DualFuel model

Calibration multiplier	H0	H20	H40	H65
Entrainment	1	0.5	0.7	0.7
Ignition delay	1	0.45	0.3	0.3
Diffusion	1.2	0.4	0.6	0.6
Turbulent Flame Speed	N/A	0.5	0.7	1.5

It is worthwhile to mention that for simulating H0, the DIPulse model was used instead of DualFuel as it is a diesel-only case. Thus, the TFS multiplier was not applicable and this test case is different from all other three cases. Also, flame speeds and flame radius calculations were not possible for this test case since the SITurb was not engaged; therefore, its results are not presented in Figures 5.37, 5.38 and 5.40.

For overall evaluation of DualFuel model capability of simulating H2-diesel combustion, the mass burned fraction for the selected case at A25 were calculated. As seen in Figure 5.36, the DualFuel modelling of hydrogen enriched cases suffer from the same weaknesses as the SITurb modelling. Indeed, the rate of turbulent premixed combustion could not be predicted precisely. This is the result of a source of error which appeared mostly at the end of mass burning. The reasons for this source of error could include:

- De-developing turbulence is not taken into account in the SITurb model.
- The flame-wall interactions and associated physical phenomena are also not directly accounted for (i.e. quench).
- Considerable scatter in the burning velocity correlations.

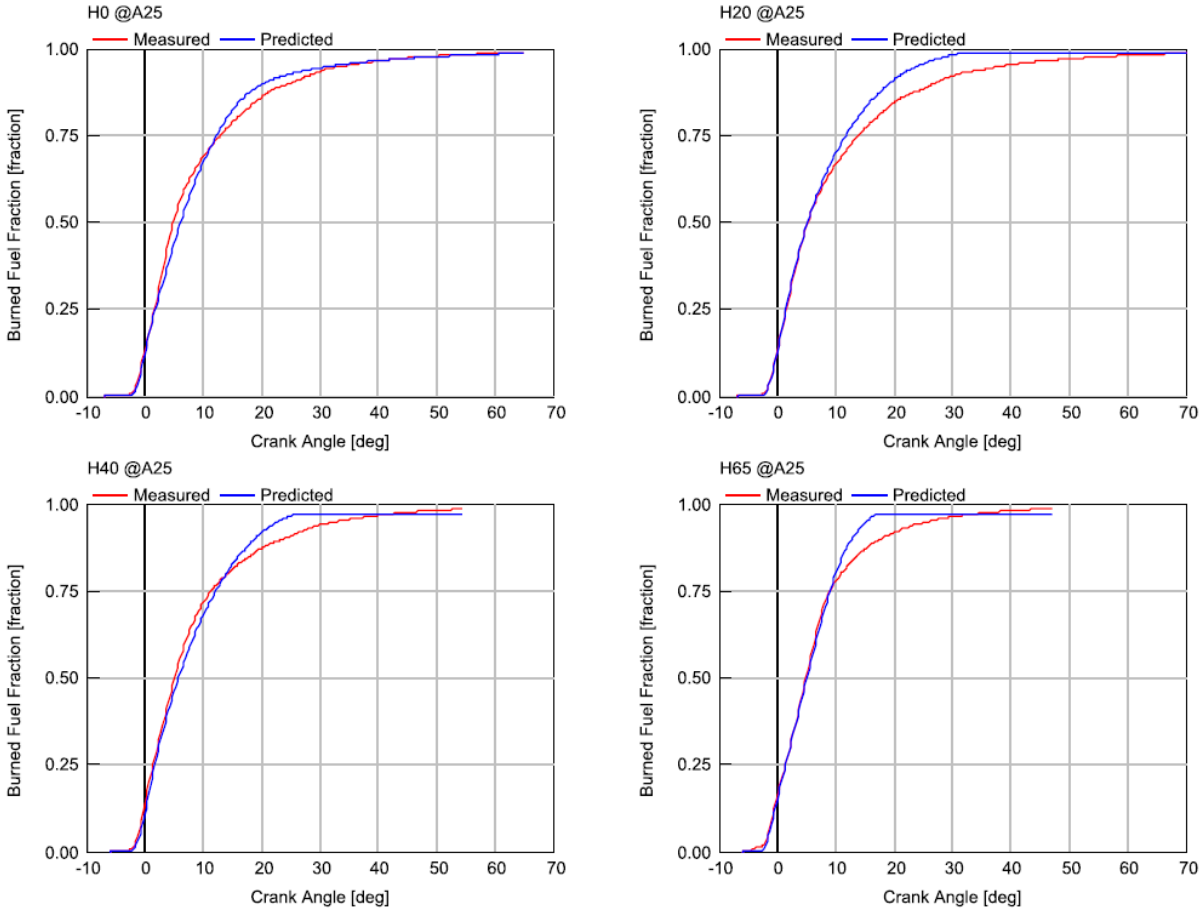


Figure 5.36: Mass burned fraction for selected cases at A25 – DualFuel model

Comparing the hydrogen-enriched cases, a significant change in the calibration multipliers is observed while shifting from H20 to H40. More entrainment was seen in H40 cf. H20 with

shorter ignition delay. Also, turbulent speed was increased as depicted in Figure 5.37. The laminar flame speed is increasing by enriching more hydrogen in dual-fuel combustion mode. These changes are all explainable regarding the conceptual model proposed by [Morgan et al. (19)] first mentioned in Section 2.6, within which the hydrogen volumetric concentration in air has a key role in dual-fuel combustion of hydrogen and diesel. In fact, the hydrogen LFL plays as a turning point where exceeding this limit leads to hydrogen pre-ignition in the hydrogen/air premixed charge.

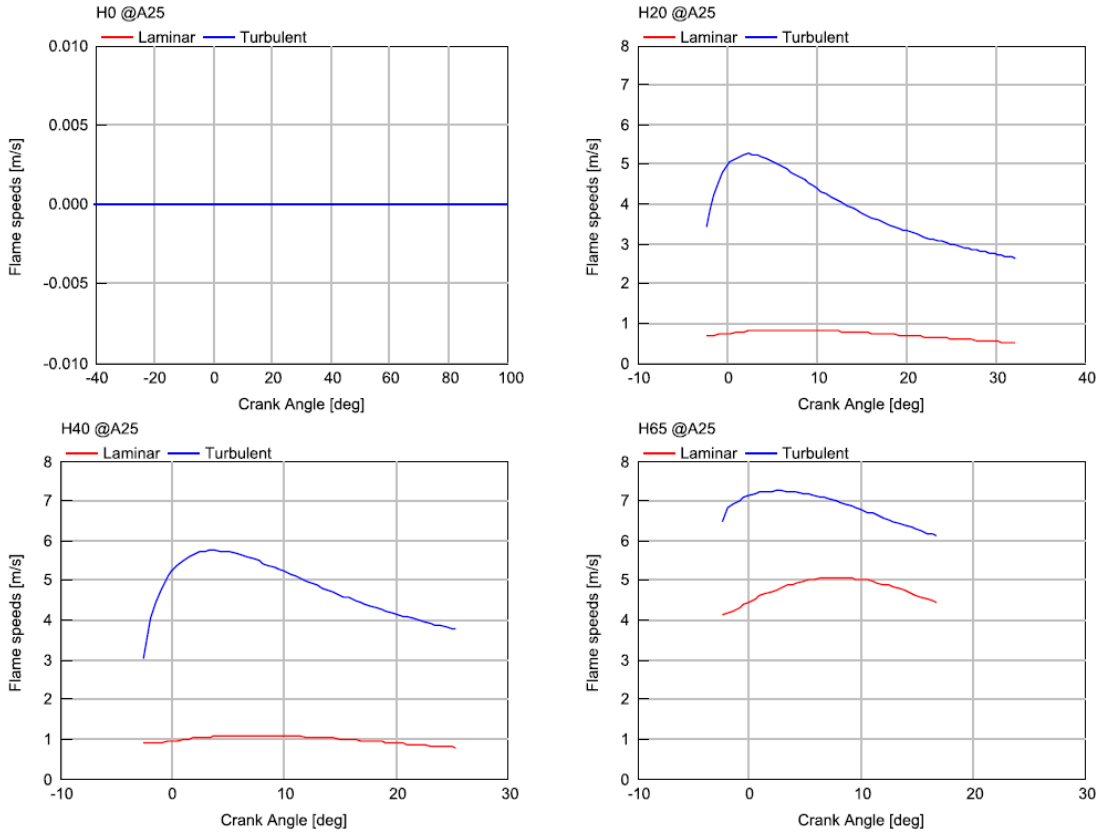


Figure 5.37: Flame speeds of selected test cases at A25 – DualFuel model

The quasi-dimensional combustion model employs the empirical "flame speed ratio" (FSR) as ratio of turbulent flame speed to laminar flame speed (Eq. 5.2), in order to define the flame propagation rate. Indeed, FSR is a useful metric for comparing the ability of the flow field to increase the rate of unburned mass entrainment.

$$FSR = \frac{u_T}{u_L} \tag{5.2}$$

FSR usefully indicates if the combustion is most affected by chemical factors (laminar flame) or turbulence. Therefore, this parameter is depicted in Figure 5.38 for the calibrated test cases.

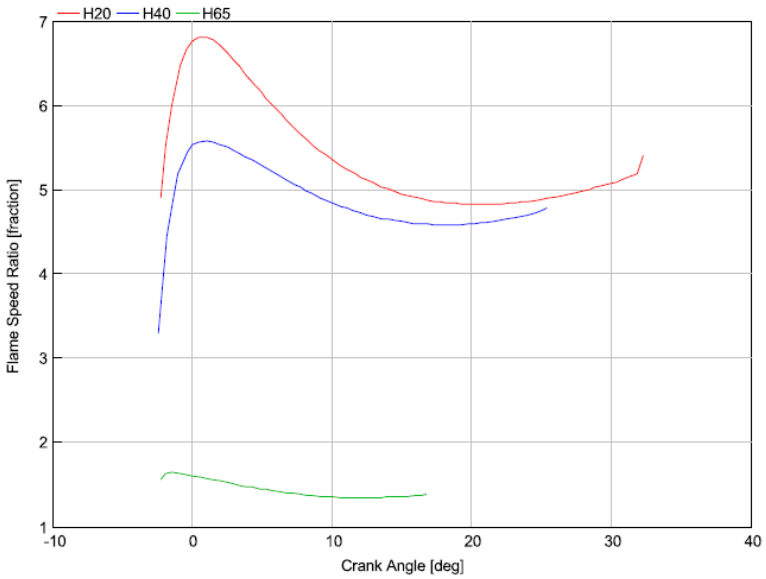


Figure 5.38: Flame speed ratio at A25 – DualFuel model

Despite the enhancement of flame speeds in both laminar and turbulent regimes for H65, it has the lowest FSR comparing with other HFs. This can be interpreted that combustion process was mostly influenced by the laminar chemical reactions rather than turbulence. However, the combustion was shorter in this case than other HFs. In addition, Figure 5.38 shows the highest FSR curve for H20 (lowest H2 fraction). This represents that influence of turbulence was more robust than effect of the chemical reactions initiated the flame at earliest stage of combustion. Therefore, hydrogen enrichment contributed mostly in accelerating the early chemical reactions rather than enhancing the turbulence level.

The significant rise of laminar flame speed for H65 is related to its extra-ordinary rise of the in-cylinder temperature (Eq. 2.9), as depicted in Figure 5.39.

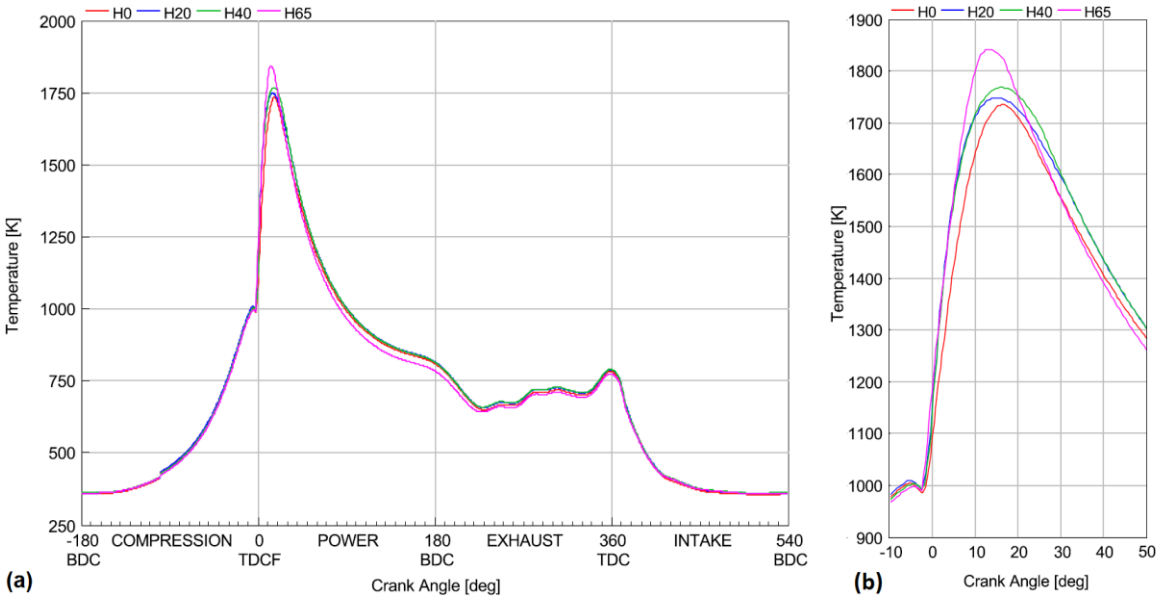


Figure 5.39: In-cylinder temperature during (a) entire cycle (b) combustion process at A25 – DualFuel model

An attribute featured by SITurb model is flame radius which is calculated for all selected cases except H0 as SITurb was not engaged for its prediction. As seen in Figure 5.40, the H65, has the fastest flame propagation. This is in accordance with MFB curve of this case (Figure 5.36) which resulted in shortest combustion duration among all cases.

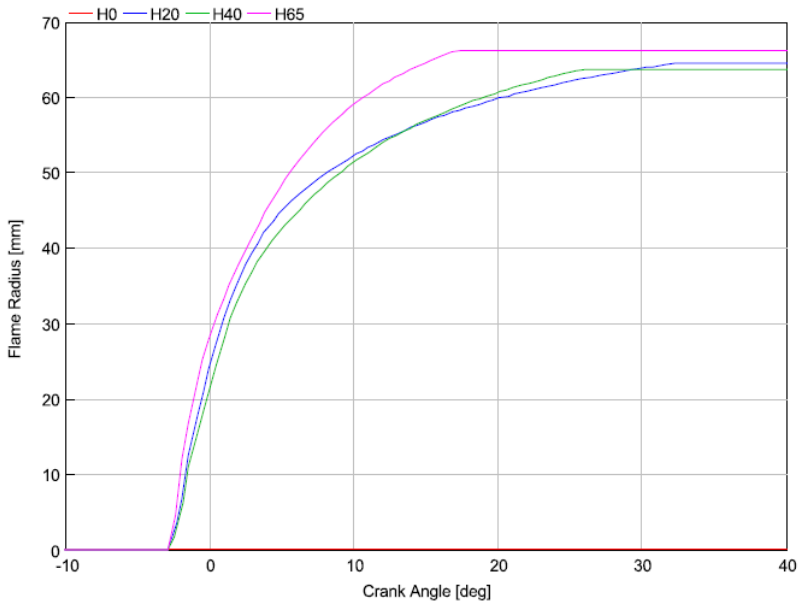


Figure 5.40: Flame radius for selected test cases at A25 – DualFuel model

The significance of H65 case can also be assessed by the specific heat ratio $\left(\gamma = \frac{c_p}{c_v}\right)$ as indicator of sources of efficiency [Heywood (7)] during the engine cycle. As seen in Figure

5.41, this case has the highest γ over the engine cycle in comparison to other test cases. This can contribute in achieving the highest indicated efficiency among all HFs at A25, as depicted in Figure 4.10.

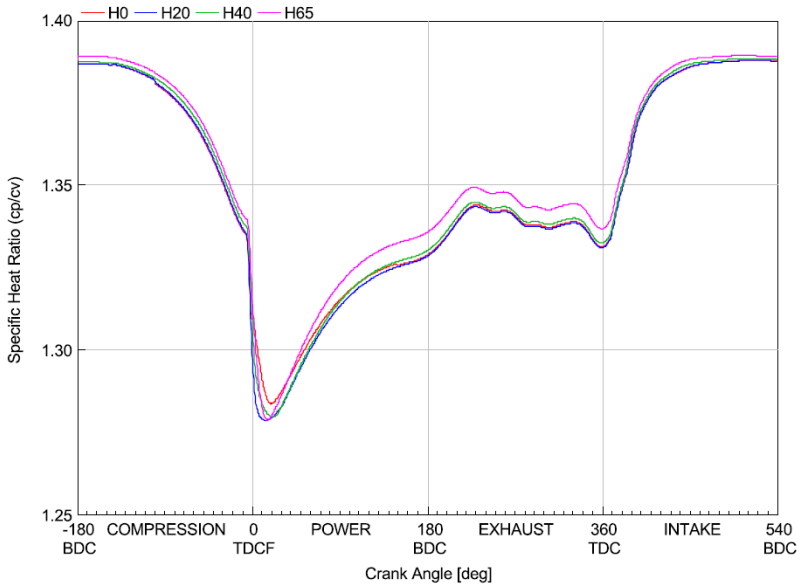


Figure 5.41: Specific heat ratio at A25 – DualFuel model

With aim of extracting more specific results from the DualFuel modelling, the in-cylinder energy balance evaluation was made by TPA approach for all calibrated test cases. As seen in Figure 5.42, the predicted indicated work and heat transfer were estimated with excellent agreement with measured counterparts. The inconsistency returns just to the predicted internal energy which can be result of two main sources of errors:

- **Estimation of burned and unburned zone temperature:** The gas temperature within each zone is assumed uniform. The model of [Martin et al. (93)] was used to calculate the average values of the specific internal energy and specific volume in the burned region. The calculations for the unburned region were described by [Hires et al. (94)].
- **Insufficiency of in-cylinder flow prediction:** this insufficiency returns to many factors mentioned here briefly: excessive simplification of hypotheses in turbulence and spray models, profound dependence of model authenticity to empirical correlations and lack of sufficient embedded data, inexistence of correlations for

hydrogen flame speed within premixed diesel, inexistence of tumble and swirl flow measurements, etc.

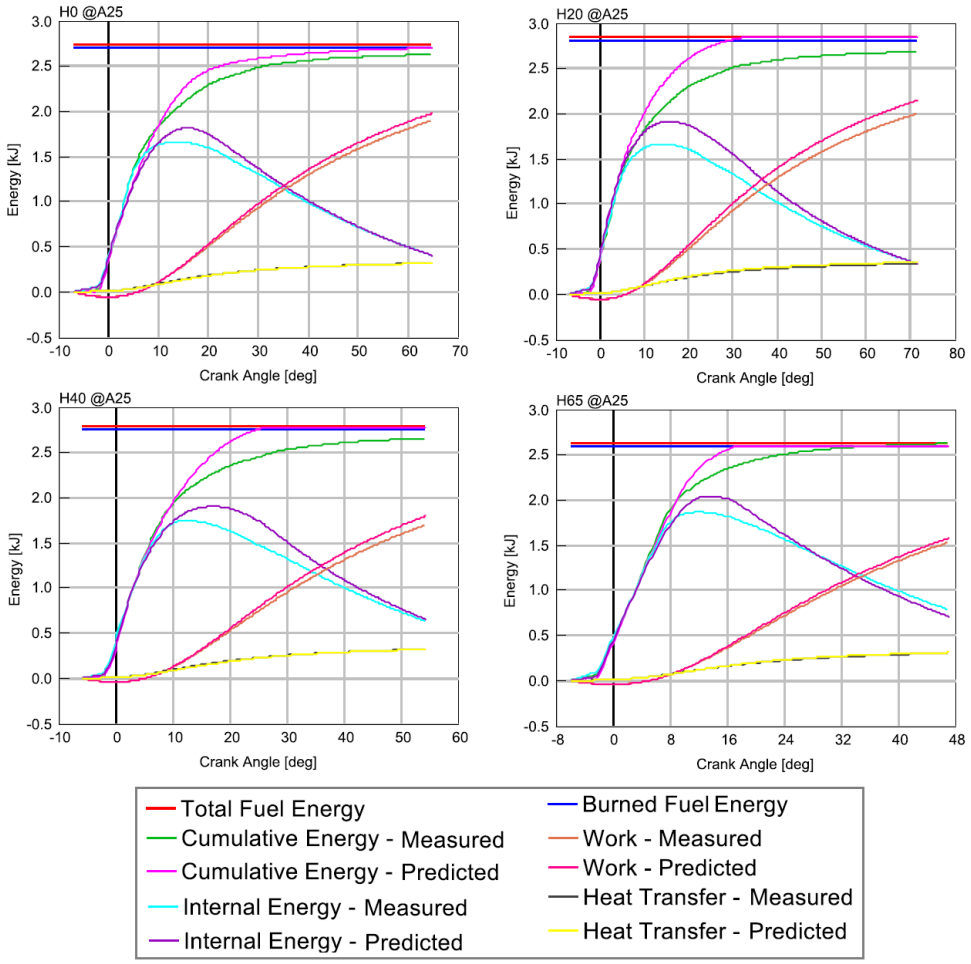


Figure 5.42: In-cylinder Energy balance evaluation at A25 – DualFuel model

5.5 Summary

By using GT-Power engine simulation code, a detailed calibration procedure was done based on the experimental results of hydrogen enrichment of the HD diesel test engine. TPA method was initially applied for exploiting the cylinder trapped conditions in addition to the measured burn rate. Two distinct phenomenological sub-models (DIPulse and SITurb) were characterised separately by an extensive sensitivity analysis of their influential factors. Applying these two sub-models in parallel within DualFuel model, allowed modelling of premixed and diffusion sections of dual-fuel combustion. Hence, the following points were resulted from the dual-fuel modelling study:

- Influential factors for dual-fuel burn rate prediction in order of importance are: (1) Diffusion, (2) Entrainment, (3) Turbulent flame speed and (4) Ignition delay (featured with SOI).
- Cylinder pressure calibration could be made perfectly via 'Dual-fuel' model.
- Predicted burn rate was in better agreement with measured result in lower H2 fraction cf. higher H2 fraction. Indeed, hydrogen pre-ignition within premixed charge prior to diesel diffusion flame is not well represented in GT dual-fuel model.
- Split injection makes ignition delay shorter in all H2 fractions. While this strategy expedites mixture entrainment in dual-fuel mode, it reduced entrainment in diesel-only mode. This is due to hydrogen's higher flame speed and diffusivity.
- Lower flammability limit plays as a turning point in dual-fuel combustion as the mechanism is affected depending on which side of LFL, the hydrogen concentration is.

Although, DIPulse and SITurb showed good capability of predicting the in-cylinder pressure and burn rate in each of their corresponding types of combustion, the DualFuel model suffers from insufficiencies in modelling of dual-fuel combustion particularly in high HFs. Admitted by senior engineers at Gamma Technologies and peer-researchers of dual-fuel modelling, there are no published works about the GT "DualFuel" combustion model. It was novel in the currently reported work, that this model was utilised for the first time to simulate H2-Diesel combustion. Despite its novelty, the current GT "DualFuel" combustion model may contain some pitfalls as follows:

- The model is in its infancy to be applied for dual-fuel modelling due to its oversimplified assumptions (e.g. single-zone homogeneous turbulence model with averagely-sized eddies).
- The model relies heavily on correlations to engine data (flame images, cylinder pressure and burn rate) to have an inclusive predictive performance.
- GT uses a proprietary equation of laminar burning velocity for hydrogen similar to Metgalchi and Keck correlations with slight modification. However, this correlation does not include the effects of flame instabilities which result in an apparent rise in u_L and hence pressure. Besides, the necessity of experimentally measuring the

burning velocity of hydrogen within the premixed diesel charge is greatly acknowledged to allow us to have better insight of dual-fuel combustion physics. Although, this dual-fuel flame speed measurement has been mostly overlooked by fellow researchers, this can be very beneficial as premixing diesel could typically extend the lean burn limit with enhancing combustion efficiency of duel-fuel engines.

- The interaction between DIPulse and SITurb within DualFuel model is not yet known exactly in detail. Indeed, those might be able to predict the “trend” of combustion process rather than prediction of corresponding variables accurately.

Chapter 6: Conclusions and Recommendations

6.1 Introduction

The main aim of the currently reported work was to improve understanding of diesel-hydrogen dual-fuel combustion with and without oxygen enrichment using advanced reverse mode thermodynamic analysis to gain additional insight. The topic is highly challenging due to attributes of the hydrogen combustion. In addition, current knowledge of dual-fuel combustion with diesel is not yet inclusive. Experimental testing on a single-cylinder HD engine proved essential to examine the practicality of high substitution rates with the aim of reducing the carbon-content emissions as much as possible. In addition, the GT-Power 1D simulation package did enable more insight into this combustion mechanism. Therefore, the conclusions extracted from currently reported work can be split into experimental and numerical study of H2-Diesel combustion.

6.2 Conclusions

6.2.1 Experimental tests conclusions

Comparing to the baseline diesel-only test results on our two targeted operating points (A25 and A50), it was aimed to achieve the best indicated efficiency-ISSoot trade-off. While the hydrogen substitution ratio (HF) was altered, the highest HF was restricted by the maximum flow rate of H2 mass flow controller. The following points were concluded:

- The pre-injection prior to the main diesel injection reduced the levels of PRRs during hydrogen fumigation.
- Cyclic variation was slightly affected by HF variation resulting in reasonable COV_IMEPn (< 5%) for both operating points.
- The LFL of hydrogen is considered as the threshold at which H2-Diesel combustion would be evolved. Exceeding this threshold leads to dismissing the ignition delay and enhancing the indicated efficiency. This change was more pronounced at mid load (A50) in comparison to low load (A25). For instance, the H30 case at A50, comprises a pre-ignition of hydrogen which has dominated in the premixed section

of the dual-fuel combustion with rapidly increasing burn rate leading to outstanding this test case from others.

- Highest hydrogen substitution ratios increased indicated efficiency by up to 4.6% at 6 bar IMEPn and 2.4% at 12 bar IMEPn.
- ISCO2, ISCO and ISsoot were reduced by 58%, 83% and 58% respectively at 6bar IMEPn. At 12 bar IMEPn, the reduction of these pollutants was 27%, 45% and 71% respectively compared to the diesel-only baseline.
- H2-Diesel dual-fuel combustion with fixed SOI resulted in an increase of NOx emissions (~26%) at 6 bar IMEPn. This increase was significant at 12 bar IMEPn, which exceeded 56%, but is an inherent feature of the elevated temperatures incurred. NOx emission could meet the 0.4 g/kWh limit of Euro VI with NOx after-treatment of 90% conversion efficiency.
- Highest hydrogen substitution ratios increased indicated efficiency by up to 4.6% at 6 bar IMEPn and 2.4% at 12 bar IMEPn.
- The oxygen enrichment strategy could curb the smoke and minimised CO emissions in expense of significant NOx increase.
- EGR dilution effect had decelerated the overall burn process while the ISNOx was restrained by applying EGR as might be expected.

6.2.2 Numerical study conclusions

Initially, an essential reverse-run calculation known as Three Pressure Analysis (TPA) was applied to account for the cylinder trapped conditions in addition to the measured burn rate. In the first step of dual-fuel modelling, the empirical Multi-Wiebe function was chosen for convenience. Later, two distinct phenomenological sub-models, DIPulse and SITurb were run in parallel in the form of a DualFuel model, which allowed modelling of premixed and diffusion sections of dual-fuel combustion. The optimisation solution was used for characterising the two sub-model calibration factors. Ultimately, the optimised calibration factors could allow predicting the burn rate and cylinder pressure with objective of minimising the RMS error between measured and predicted burn rate. The predictive model could be used for calculating the flame speeds (laminar and turbulent) in addition to other turbulent parameters for each test case.

The numerical study results can be concluded as follows:

- The correlations of Multi-Wiebe function show the contributions of each section of DI combustion in accordance with the conventional amounts suggested within the key literature. The premixed section is mostly altered by HF variation. While in the diesel-only (H0) case, premixed duration is shorter than that in H30. This reflects that higher HF leads to pre-ignition and hence faster premixed section. In addition, the main section got shortened by adding more H2 since less diesel fuel is burned in form of diffusion combustion. The tail duration was also decreasing by increasing H2 fraction, which led to the shorter overall combustion duration.
- In the DIPulse model, breakup time of spray into droplets ($\mathbf{t_b}$) plays as a turning point in the spray penetration length. Since $\mathbf{t_b}$ depends on the nozzle geometry, the discharge coefficient of nozzle can be used as a calibration factor. Indeed, by increasing this coefficient, the $\mathbf{t_b}$ and hence the ignition delay is shortened.
- The entrainment factor of DIPulse has a significant effect on the combustion process as the higher values result in higher burn rate in shorter duration.
- As the higher value of ignition delay multiplier in DIPulse allows more fuel to be agglomerated and then burns in premixed mode, the premixed phase peak was increased with slight effect on in-cylinder pressure. Entrainment and ignition multipliers have an inverse effect.
- The slope of premixed curve was slightly increased with higher values of the premixed rate multiplier in DIPulse model. However, this is so negligible which makes this factor have almost no effect on burn rate. Thus, it was set to “1” for all calibrations.
- The slope of the diffusion curve and its peak would be increased with higher values of diffusion rate multiplier of DIPulse model. Although, the cylinder pressure peak was also enhanced, the premixed section remained intact.
- Nevertheless, DIPulse is not a comprehensive predictive model as it needs several constants to fit (not predict) the burn rate. Furthermore, there is not only one single set of constants which give the best-fit.

- The burn rate RMS error minimisation done in the optimisation solution cannot solely guarantee the matching of burn rate for each stage of the combustion individually. This is because it returns the average error over the whole burn process.
- Since the swirl and tumble flow measurements (i.e. their corresponding measured torques) were not existed, the coefficients for these two parameters were ignored within intake valves. As these coefficients are required for TPA calculations (which its turbulence results are required for "EngCylFlow" and "SITurb" calibration), this makes an insufficiency in turbulence intensity (u') and length scale (L) calculation and subsequently in the turbulent flame speed estimation.
- In gasoline SITurb modelling, the turbulent flame speed multiplier is scaling the turbulent burning velocity. Its higher values will accelerate combustion and increase the heat release rate. In addition, the predicted cylinder pressure is hugely magnified by increasing this multiplier. Thus, selecting this multiplier should be carried out with extra care; i.e. it has the highest relative sensitivity. C_{TFS} has also significant effect on turbulent parameters. This effect has been mainly pronounced on turbulence intensity during combustion process. The integral length scale variance is reduced for the C_{TFS} values higher than unity. In addition, the higher values of C_{TFS} would accelerate the flame propagation as expected.
- The Taylor length scale multiplier is directly related to $\boldsymbol{\tau_b}$. It has a swinging effect with turbulent flame speed multiplier. However, the cylinder pressure and burn rate are less sensitive to this multiplier than C_{TFS}.
- The Dilution effect is the direct constant of proportionality within the laminar burning velocity equation. The effect of residual burnt gas on burn rate and cylinder pressure except in excessive values is not significant and it can only be applied for fine-tuning the predicted burn rate. It is observed that the values below unity for this multiplier are not too much effective and just higher values than unity are being influential. Since the EGR percentage was kept fixed during our testing, this multiplier can be set to "1" for all simulating cases.

- The flame kernel growth multiplier acts as the multiplier of integral length scale within the equation for turbulent burning velocity. It has no major effect neither on burn rate and cylinder pressure except in very low value (e.g. “0.1” which is not in our aim). Thus, it was set to “1” for all simulating cases.
- The accuracy of the turbulent entrainment model proposed in GT, depends on the precision of calculations for: (1) projected flame area, (2) laminar burning velocity and (3) turbulent burning velocity.
- The DualFuel model combines the two distinct combustion models of DIPuse and SITurb. DIPulse will handle the burning of the direct injected fuel and any premixed fuel that is entrained by the fuel spray and SITurb will model the resulting flame propagation for the premixed mixture. Although, the flame front area for SITurb initially uses the conical area of the spray from DIPulse but the flame will finally transit to a spherical flame. However, the exact interaction between these two models within the DualFuel model is still not very clear.
- The influential multipliers for ‘DualFuel’ burn rate prediction in order of importance are: diffusion, entrainment, turbulent flame speed and ignition delay multiplier.
- The DualFuel modelling of hydrogen enriched cases suffer from the same weaknesses as the SITurb modelling. Indeed, the rate of turbulent premixed combustion could not be predicted precisely. This is result of a source of error which appears mostly at the end of mass burning. The reasons for this source of error could include: first, de-developing turbulence is not taken into account in SITurb model. Second, the flame-wall interactions and associated physical phenomena are also not directly accounted for (i.e. quench). Third, considerable scatter is existing in the burning velocity correlations.
- The laminar flame speed is increasing by enriching more hydrogen in dual-fuel combustion mode. These changes are all explainable regarding the conceptual model proposed by Morgan et al.
- The burning speeds enhancement for both laminar and turbulent flames are more pronounced in H65, particularly in laminar regime which is related to its extra-ordinary rise of the in-cylinder temperature.

- The H65, has the fastest flame propagation. This is in accordance with MFB curve of this case which resulted in shortest combustion duration among all cases. Nevertheless, H65 has the lowest FSR comparing with other HFs emphasising that its combustion process was mostly affected by the chemical activities rather than turbulence.
- The highest FSR was obtained by H20 (lowest H2 fraction). Hence, hydrogen addition was mainly pronounced in expediting the early stage chemical reactions instead of turbulence level enhancement.
- As a proof for achieving the highest indicated efficiency by H65 at A25, the highest specific heat ratio was obtained by this test case over entire engine cycle.
- The predicted indicated work and heat transfer were estimated with excellent agreement with measured counterparts as presented in the in-cylinder energy balance evaluation. The only remained inconsistency relates to the predicted internal energy because of two main sources of errors: 1) estimation of T_u and T_b, 2) inaccuracies within cylinder flow prediction.

6.3 Recommendations

The hydrogen enrichment in internal combustion engines is challenging from various perspectives. While it needs to consider the safety measures from feasibility point of view, the complicated essence of dual-fuel combustion is the barrier for developing this approach within IC engines especially in HD diesel ones. On the other hand, one key required feature for a robust phenomenological model is its universality i.e. consistency of model constants towards various combustion chamber settings and operating conditions. Nonetheless, the current phenomenological models cannot handle the complexity of realistic dual-fuel combustion. Therefore, some recommendations are presented here in response to the insufficiencies of the current work:

- Other experimental testing points (engine speed and load) need to be studied for characterising the H2-Diesel combustion. Direct injection of hydrogen also allows to change the process of dual-fuel combustion depending on injection timing of hydrogen and diesel. Optical diagnostics can give a better insight into the dual-fuel

combustion phenomenon. In other word, the dual-fuel combustion which suffers the precise conceptualisation, needs to be under specific scrutiny as its physical and chemical aspects are not yet fully understood.

- Minimising the burn rate RMS error is not the sole perfect optimisation target. Gamma Technologies might fit in other parameters of interest such as: IMEP percentage error, CA50 or maximum cylinder pressure as the optimisation objectives. The multi-objective optimisation capabilities introduced in v2017, allows finding a better solution (e.g. burn rate RMS error and IMEP error).
- If the model is to ever be adopted as a useful diagnostic then Gamma Technologies should publish the exact details of interaction between DIPulse and SITurb taken place within the DualFuel model.
- The de-developing turbulence effect must be taken into account in the SITurb model. Also, more rigid empirical laminar burning velocity correlations are required for hydrogen to be included in this model.
- A large set of experimental data including the burn rate, cylinder pressure and flame images would be essential to derive a robust comprehensive predictive model. These data can be fed into the GT SITurb model in form of look-up tables.
- The main obstacles for further development in the turbulence prediction are poor understanding of turbulent flow and lack of laminar flame speeds measured at high pressures and temperatures considering its instability and cellularity. For dual-fuel modelling of H2-Diesel, it is necessary to include the experimental measurements of hydrogen burning velocity with premixed diesel.
- Finally, in order to precisely assess the accuracy of the model, flow visualisation or correlated CFD are required to precisely define the evolution of the in-cylinder flow and turbulence during the cycle.

Chapter 7: References

This list is sorted in order of appearance in the text:

1. Kyoto Protocol, https://en.wikipedia.org/wiki/Kyoto_Protocol (Retrieved Jun 2018)
2. Adoption of the Paris Agreement, United Nations, Framework Convention on Climate Change, UN Doc FCCC/CP/2015/L.9/Rev.1 (12 Dec 2015).
3. United Nations Framework Convention on Climate Change: Article 2, United Nations, 1992.
4. Final UK greenhouse gas emissions national statistics 1990-2014, https://assets.publishing.service.gov.uk/government/uploads/system/uploads/attachment_data/file/496946/2014_Final_Emissions_Statistical_Summary_Infographic.pdf (Retrieved Jun 2018)
5. Internal Combustion Engine, https://en.wikipedia.org/wiki/Internal_combustion_engine Retrieved Jun 2018
6. Diesel Cycle, https://en.wikipedia.org/wiki/Diesel_cycle Retrieved Jun 2018
7. Heywood, J. B., Internal combustion engine fundamentals, 1st Edittion, New York, NY: McGraw-Hill, 1988.
8. Ferguson, C. R. and Kirkpatrick, A. T., Internal Combustion Engines: Applied Thermosciences, 3rd Edition, Wiley, 2015.
9. Georgi, B., Hunkert, S., Liang, L. and Willmann, M., Realizing Future Trends in Diesel Engine Development, SAE Technical Paper 972686, 1997.
10. Compressed Natural Gas, https://en.wikipedia.org/wiki/Compressed_natural_gas Retrieved Jun 2018
11. Table 6. Carbon Intensity Lookup Table for Gasoline and Fuels that Substitute for Gasoline. (http://www.arb.ca.gov/fuels/lcfs/121409lcfs_lutables.pdf) (PDF). Arb.ca.gov. (Retrieved Jun 2018).
12. Financial Tribune, Iran Gas Vehicle Market Projections, http://financialtribune.com/articles/economy-auto/32408/iran-gas-vehicle-market-projections Released on 20 Dec 2015

13. May, I. A., An Experimental Investigation od Lean-burn Dual-fuel Combustion in a Heavy Duty Diesel Engine, PhD Thesis, Brunel University London, Sep 2017.
14. Biogas, http://en.wikipedia.org/wiki/Biogas Retrieved Jun 2018.
15. Biogas Map developed by NNFCC http://www.biogas-info.co.uk/resources/biogas-map/ Retrieved Jun 2018.
16. Biogas market data in Germany 2016/2017, German Biogas Association, Released on Oct 2017.
17. Wimmer, A., Wallner, T., Ringler, J. and Gerbig, F., H2-Direct Injection – A Highly Promising Combustion Concept, SAE Technical Paper, 2005-01-0108, 2005.
18. Karim, G. A., Dual-fuel Diesel Engines, CRC Press, 2015.
19. Morgan, R., Atkins, P., Atkins, A., Lenartowicz, C. and Heikal, M., Effect of Hydrogen Fumigation in a Dual Fueled Heavy Duty Engine, SAE Technical Paper 2015-24-2457, 2015.
20. Light Weight Hydrogen 'Tank' Could Fuel Hydrogen Economy, ScienceDaily, Released on Nov 2008.
21. "Alternative Fueling Station Counts by State, Alternative Fuels Data Center, US Dept. of Environment, https://www.afdc.energy.gov/fuels/stations_counts.html Retrieved Jun 2018.
22. BMW Hydrogen 7, http://en.wikipedia.org/wiki/BMW_Hydrogen_7 Retrieved Jun 2018
23. Szwabowski, S. J., Hashemi, S., Stockhausen, W. F., et al. Ford Hydrogen Engine Powered P2000 Vehicle, SAE Technical Paper 2002-01-0243, 2002.
24. Natkin, R. J., Denlinger, A. R., Younkins, M. A. , et al., Ford 6.8L Hydrogen IC Engine for the E-450 Shuttle Van, SAE Technical Paper 2007-01-4096, 2007.
25. Low Carbon Vehicle Partnership. Innovations in UK road transport: Driving the economy, cutting carbon. Reported on 9 March 2015.
26. Alset Global ‘‘Our Solutions’’, http://alset.at/our-solutions/ Retrieved Jun 2018
27. Monemian, E., Cairns, A., Gilmore, M., et al., Evaluation of intake charge hydrogen enrichment in a heavy-duty diesel engine, Procedding of IMechE Part D: Journal of Automobile Engineering, Nov 2017

28. Stenlåås, O., Christensen, M., Egnell, R., et al. "Hydrogen as Homogeneous Charge Compression Ignition Engine Fuel", SAE Technical Paper 2004-01-1976, 2004.
29. Rosati, M. F., Aleiferis, P. G., Hydrogen SI and HCCI Combustion in a Direct-Injection Optical Engine, SAE Technical Paper 2009-01-1921, 2009.
30. Andre Lanz et al., Hydrogen fuel cell engines and related technologies, College of the Desert, Dec 2001.
31. Cassidy, J. F., Emissions and total energy consumption of a multicylinder piston engine running on gasoline and a hydrogen-gasoline mixture, NASA Technical Note, May 1977.
32. Emission Standard, http://en.wikipedia.org/wiki/Emission_Standard Retrieved Jun 2018
33. Canis, B., Lattanzio, R. K., U.S. and EU Motor Vehicle Standards: Issues for Transatlantic Trade Negotiations, US Congressional Research Service, Reported on 18 February 2014.
34. Provisional New CV Registrations or Sales (2014), OICA statistics, http://www.oica.net/category/sales-statistics/ (Retrieved Apr 2017).
35. Greenhouse gas emission statistics - emission inventories, EU statistics, http://ec.europa.eu/eurostat/statistics-explained/index.php/Greenhouse_gas_emission_statistics (Retrieved Apr 2017).
36. Climate Change Act 2008, http://www.legislation.gov.uk/ukpga/2008/27/pdfs/ukpga_20080027_en.pdf (Retrieved Jun 2018)
37. EU: Heavy-Duty Truck and Bus Engines, DieselNet, https://www.dieselnet.com/standards/eu/hd.php (Retrieved Jun 2018)
38. European Stationary Cycle (ESC), DieselNet, http://www.dieselnet.com/standards/cycles/esc.php (Retrieved Jun 2018).
39. Espey, C. and Dec, J. E., "Diesel Engine Combustion Studies in a Newly Designed Optical-Access Engine Using High-Speed Visualization and 2-D Laser Imaging," SAE Transactions, Vol. 102, Sec. 4, pp. 703-723, paper no. 930971, 1993.
40. Dec, J. E. and Coy, E. B., "OH Radical Imaging in a DI Diesel Engine and the Structure of the Early Diffusion Flame," SAE paper no. 96083 1, 1996.

41. Espey, C. and Dec, J. E., "The Effect of TDC Temperature and Density on the Liquid-Phase Fuel Penetration in a D.I. Diesel Engine," SAE Transactions, Vol. 104, Sec. 4, pp. 1400-14 14, paper no. 952456, 1995.
42. Espey, C., Dec, J. E., Litzinger, T. A. and Santavicca, D. A., "Quantitative 2-D Fuel Vapor Concentration Imaging in a Firing D.I. Diesel Engine Using Planar Laser- Induced Rayleigh Scattering," SAE Transactions, Vol. 103, Sec. 3, pp. 1145-1 160, paper no. 940682, 1994.
43. Espey, C., Dec, J. E., Litzinger, T. A. and Santavicca, D. A., "Planar Laser Rayleigh Scattering for Quantitative Vapor-Fuel Imaging in a Diesel Jet," Combustion and Flame, in press 1997.
44. Dec, J. E. and Espey, C., "Soot and Fuel Distributions in a D.I. Diesel Engine via 2-D Imaging," SAE Transactions, Vol. 101, Sec. 4, pp. 1642-1651, paper no. 922307, 1992.
45. Dec, J. E., "Soot Distribution in a D.I. Diesel Engine Using 2-D Imaging of Laser-Induced Incandescence, Elastic Scattering, and Flame Luminosity," SAE Transactions, Vol. 101, Sec. 4, pp. 101-112, paper no. 920115, 1992.
46. Dec, J. E. and Espey, C., "Ignition and Early Soot Formation in a D.I. Diesel Engine Using Multiple 2-D Imaging Diagnostics," SAE Transactions, Vol. 104, Sec. 3, pp. 853-875, paper no. 950456, 1995.
47. Dec, J. E. and Espey, C. "Soot and Liquid-Phase Fuel Distributions in a Newly Designed Optically Accessible D.I. Diesel Engine," Proceedings of the 1993 Diesel Emission Reduction Workshop, La Jolla, CA, July 1993, and Sandia National Laboratories Report No. SAND93-8690C
48. Dec, J. E., A Conceptual Model of DI Diesel Combustion Based on Laser-Sheet Imaging, SAE Technical Paper 970873, 1997.
49. Flynn, P. F., Durrett, R. P., Hunter, G. L., et. al., Diesel Combustion: An Integrated View Combining Laser Diagnostics, Chemical Kinetics, And Empirical Validation, SAE Technical Paper 1999-01-0509, 1999.
50. Sitkei, G., Kraftstoffaufbereitung und Verbrennung bei Dieselmotoren, Berlin/Göttingen/Heidelberg: Springer-Verlag, 1964.
51. Kamimoto, T., Bae, M., High Combustion Temperature for the Reduction of Particulate in Diesel Engines, SAE Technical Paper 880423, 1988.

52. Zhao, H., Advanced direct injection combustion engine technologies and development Volume 2: Diesel engines, CRC Press, 2010.
53. European Commission. Road transport: reducing CO2 emissions from vehicles, https://ec.europa.eu/clima/policies/transport/vehicles_en (Retrieved Jul 2016).
54. Reitz, R. D. and Duraisamy, G., Review of high efficiency and clean reactivity controlled compression ignition (RCCI) combustion in internal combustion engines, Prog Energy Combust Sci 2015; 46: 12–71.
55. Morgan, R. E., Heikal, M. R., Atkins, A. F., et al., Results from the testing of a heavy duty diesel engine with hydrogen fumigation, IMechE ICEs conference, London, 2015.
56. Gardiner, M., Energy requirements for hydrogen gas compression and liquefaction as related to vehicle storage needs, 2009.
57. Wurster, W. Z. R., "Chapter 3: Production of Hydrogen. Part 4: Production from electricity by means of electrolysis".
58. Carbon, U.G.G.; https://www.gov.uk/government/uploads/system/uploads/attachment_data/file/69554/pb13773-ghg-conversion-factors-2012.pdf (Retrieved Jun 2018).
59. Strbac, G., et al., Strategic assessment of the role and value of energy storage systems in the UK low carbon energy future, Report for the Carbon Trust by Imperial College, London, Jun 2012. https://www.carbontrust.com/media/129310/energy-storage-systems-role-value-strategic-assessment.pdf (Retrieved Jun 2018).
60. Wiebe, I. I., Progress in engine cycle analysis: Combustion rate and cycle processes, Mashgiz, Ural-Siberia Branch, 1962, 271 pp (in Russian), 1962.
61. Stiesch, G., Modeling Engine Spray and Combustion Processes, Springer Berlin Heidelberg, 2003.
62. Yoshizaki, Y., Nishida, K. and Hiroyasu, H., Approach to Low NOx and Smoke Emission Engines by Using Phenomenological Simulation, SAE Technical Paper 930612, 1993.
63. Engine Performance Application Manual (v2018), Gamma Technologies, 2018.
64. Stone, R., Introduction to Internal Combustion Engines, 4th Edition, Palgrave Macmillan, 2012.

65. Tabaczynski, R. J., Ferguson, C. R., Radhakrishnan, K., A Turbulent Entrainment Model for Spark-Ignition Engine Combustion, SAE Technical Paper 770647, 1977.
66. Farr, S. S., Modelling of Burn Rate in a Spark Ignition Engine-Comparison of Laminar Burning Velocity Data and Turbulent Entrainment and Burning Velocity Models, MSc report, Leeds University, 1998.
67. Metghalchi, M and Keck, J.C.: "Burning Velocities of Mixtures of Air with Methanol, Iso-octane, and Indolene at High Pressure and Temperature", Combustion and Flame, 48, 191 (1982).
68. Ishikawa, S., Ohmori, Y., Fukushima, S., et al., Measurement of Rate of Multiple-Injection in CDI Diesel Engines, SAE Technical Paper 2000-01-1257, 2000.
69. Onboard Vehicle Electro Hydrogen Generation & Co-Firing, Fully Funded Via a Round 3 EIS Raise, VN-Automotive Ltd. http://www.vn-cp.co.uk/vn-cp-projects/vna-ltd/ (Retrieved June 2018).
70. Pellistor, http://en.wikipedia.org/wiki/Pellistor (Retrieved Jun 2018).
71. FMA 5400/FMA 5500 Mass Flow Controllers User's Manuals, OMEGA ENGINEERING INC., 2001.
72. Zhang, Y., Experimental Inverstigation of CAI Combustion in a Two-stroke Poppet Valve DI Engine, PhD Thesis, Brunel University London, Oct 2014.
73. Schwoerer, J., Kumar, K., Ruggiero, B., et al., Lost-Motion VVA Systems for Enabling Next Generation Diesel Engine Efficiency and After-Treatment Optimization, SAE Technical Paper 2010-01-1189, 2010.
74. Zhao, H., Ladommatos, N., Engine Combustion Instrumentation and Diagnostics, Society of Automotive Engineers, 2001.
75. Economic Commission for Europe of the United Nations (UN/ECE). Regulation No 49 – uniform provisions concerning the measures to be taken against the emission of gaseous and particulate pollutants from compression ignition engines and positive ignition engines for use in vehicles. Off J Eur Union 2013; L 171/1.
76. GT-SUITE Flow Theory Manual, Gamma Technologies, 2018

77. Morel, T., Keribar, R., A Model for Predicting Spatially and Time Resolved Convective Heat Transfer in Bowl-in-Piston Combustion Chambers, SAE Technical Paper 850204, 1985.
78. GTSUITE's Help Navigator (v2018), Gamma Technologies, 2018.
79. Keeler, B., Constraints on the operation of a DI diesel engine in partially-premixed combustion mode, PhD thesis, University of Nottingham, 2009.
80. Jung, D. and Assanis, D. N., Multi-Zone DI Diesel Spray Combustion Model for Cycle Simulation Studies of Engine Performance and Emissions, SAE Technical Paper 2001-01-1246, 2001.
81. Aggarwal, S. K., and F. Peng., A Review of Droplet Dynamics and Vaporization Modeling for Engineering Calculations, Journal of Engineering for Gas Turbines and Power, 117 (1995): 453-461, 1995.
82. Blizard, N.C and Keck, J.C., Experimental and Theoretical Investigation of a Turbulent Burning Model for Internal Combustion Engines, SAE Technical Paper 740191, 1974.
83. Hires, S. D., Tabaczynski, R. J. and Novak, J. M., The Prediction of Ignition Delay and Combustion Intervals for a Homogeneous Charge, Spark Ignition Engine, SAE Technical Paper 780232, 1978.
84. Walther, H., Schlatter, S., Wachtmeister, G., Boulouchos, K., Combustion Models for Lean-Burn Gas Engines with Pilot Injection, MTZ paper 02I2012 Volume 73, 2011.
85. Pedrozo, V. B., May, I., Dalla Nora, M., et al., Experimental analysis of ethanol dual-fuel combustion in a heavy-duty diesel engine: An optimisation at low load, Applied Energy 165 (2016) 166–182, 2016
http://dx.doi.org/10.1016/j.apenergy.2015.12.052
86. Dhole, A. E., Yarasu, R. B. and Lata D. B., Investigations on the combustion duration and ignition delay period of a dual fuel diesel engine with hydrogen and producer gas as secondary fuels, Appl Therm Eng 2016; 107: 524–532.
87. Verhelsta, S. and Wallnerb, T., Hydrogen-fueled internal combustion engines, Prog Energy Combust Sci 2009; 35: 490–527.
88. Monemian, E., Cairns, E., Pedrozo, V., Hydrogen and Oxygen Fuel Enrichment Effects on a HD Diesel Engine, The journal of engine research, Vol. 47 (Summer 2017), pp. 13-20.

89. GT-SUITE DOE-POST Reference Manual (v2018), Gamma Technologies, 2018.
90. GT-SUITE Optimization Manual (v2018), Gamma Technologies, 2018.
91. Sensitivity Analysis, http://en.wikipedia.org/wiki/Sensitivity Analysis (Retrieved Jun 2018).
92. Deb, K. et al., An Evolutionary Many-Objective Optimization Algorithm Using Reference-Point-Based Non-dominated Sorting Approach, Part I: Solving Problems With Box Constraints, IEEE Transactions on Evolutionary Computation, 18(4):577-601, 2014.
93. Martin, M. K. and Heywood, J. B., Approximate Relationships for the Thermodynamic Properties of Hydrocarbon-Air Combustion Products, To appear in Combustion Science and Technology.
94. Hires, S. D., Ekchian, A., Heywood, J. B., Tabaczynski, R. J. and Wall, J. C., Performance and NoxEmissions Modelingof a Jet Ignition PrechamberStratified Charge Engine, SAE Technical Paper 760161, 1976.

Appendix A: Technical specifications of measurement devices

Measured Variable	*Device*	*Manufacturer*	*Dynamic Range*	*Accuracy*
Engine speed	AG150 Dynamometer	Froude Hafmann	0–8000 rpm	± 1 rpm
Engine torque			0– 500 Nm	± 0.25% of full scale (FS)
Oil pressure	Pressure transducer UNIK 5000	GE	0-10 bar	< ± 0.2% of FS
Temperature	Thermocouple K Type (Class 2)	RS	233-1473 K	≤ ± 2.5 K or ± 0.75% of readings
Diesel flow rate (supply)	PROline promass 83A DN02	Endress+Hauser	0-20 kg/h	± 0.1% of reading
Diesel flow rate (return)	PROline promass 83A DN01		0-100 kg/h	
Intake air mass flow rate	Proline t-mass 65F	Endress+Hauser	0-910 kg/h	± 1.5% of reading (10 to 100% of FS)
Air/Fuel ratio	Lambda sensor	Bosch LSU4, Motec PLM	$0.65 - \infty$	± 0.7 to 3% of reading
H2 mass flow rate	FMA5542A-ST-H2-50/0 PSIG	OMEGA	0-100 SLM	± 1.5% of FS
O2 mass flow rate	O2 rotameter	RM&C	10-100 SLM	± 1.25% of FS
H2 concentration	Xgard (Type 5) detecting sensor	Crowcon	0-100% LEL	Response time < 15s
O2 concentration	Xgard (Type 1) detecting sensor			Response time < 10s
Intake & exhaust pressures	Piezoresistive pressure sensor Type 4049A Amplifier Type 2622A	Kistler	0-10 bar	≤ ± 0.5% of FS within 0-353 K
Intake valve lift	S-DVRT-24 Displacement Sensor DEMOD-DVRT_TC conditioner	LORD MicroStrain	0-24 mm	± 1% of reading using straight line
In-cylinder pressure	Piezoelectric pressure sensor Type 6125C	Kistler	0-300 bar	≤ ± 0.4% of FS
	Amplifier FI Piezo	AVL		≤ ± 0.01% of FS
Diesel injector current signal	Current probe PR30	LEM	0-20 A	± 1% of reading ± 2 mA
Clock signal	Encoder EB58	Encoder Technology	0-25000 rpm	0.25 degCA
Filter Smoke Number (FSN)	415SE	AVL	0-10 FSN	-
CO (low content)	AIA-721A	Horiba (MEXA 7170 DEGR)	0-2.5k ppm	≤ ± 1.0% FS or ± 2.0% of readings
CO (mid-high content)	AIA-722		0-12 vol%	
CO2	AIA-722		0-20 vol%	
NOx	CLA-720MA		0-500 ppm or 0-10k ppm	
O2	MPA-720		0-25 vol%	
Unburnt HC	FIA-725A		0-500ppm or 0-50k pppm	

Appendix B: Supplementary Simulation Results

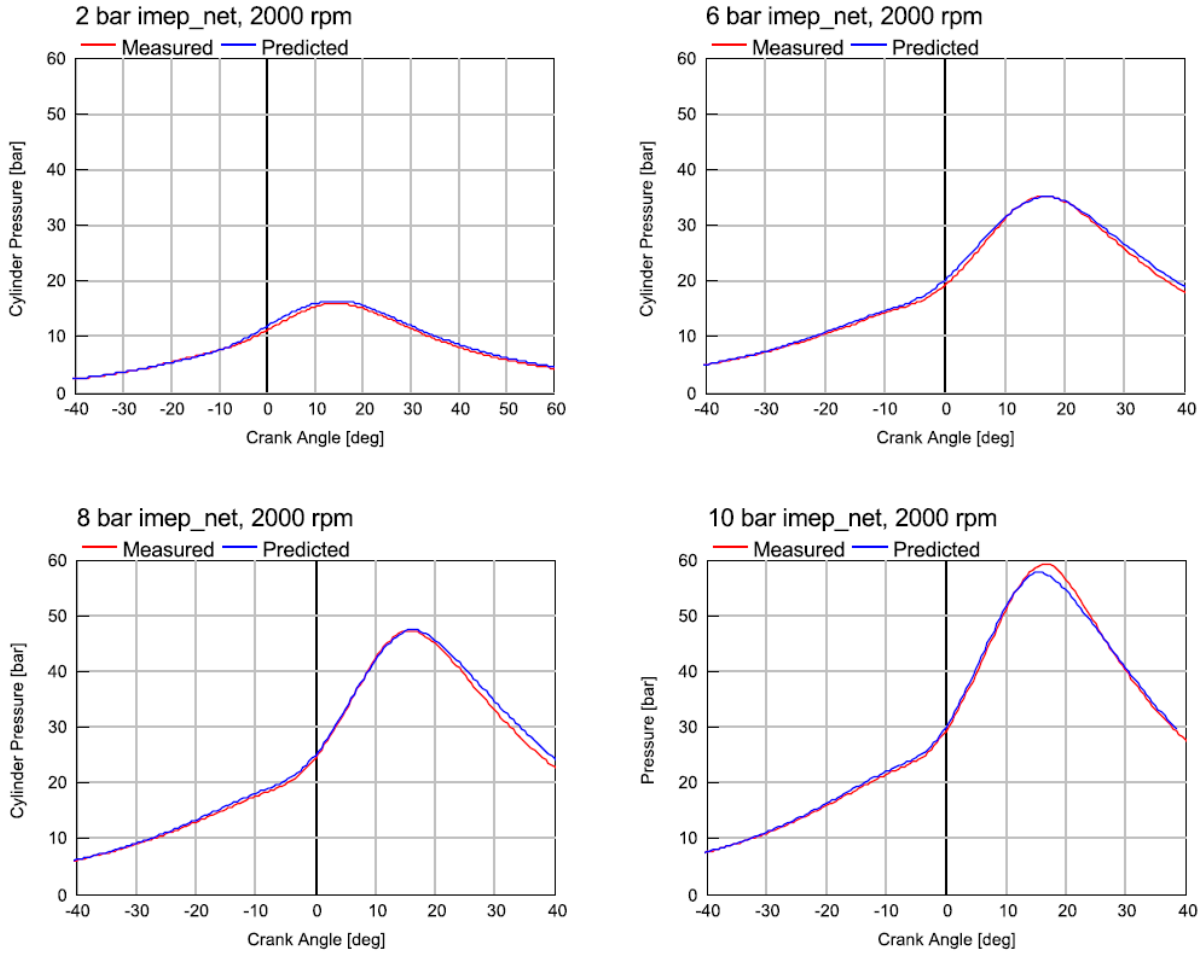


Figure B-1: Calibrated SITurb for 4 swept loads of gasoline engine: Cylinder pressure

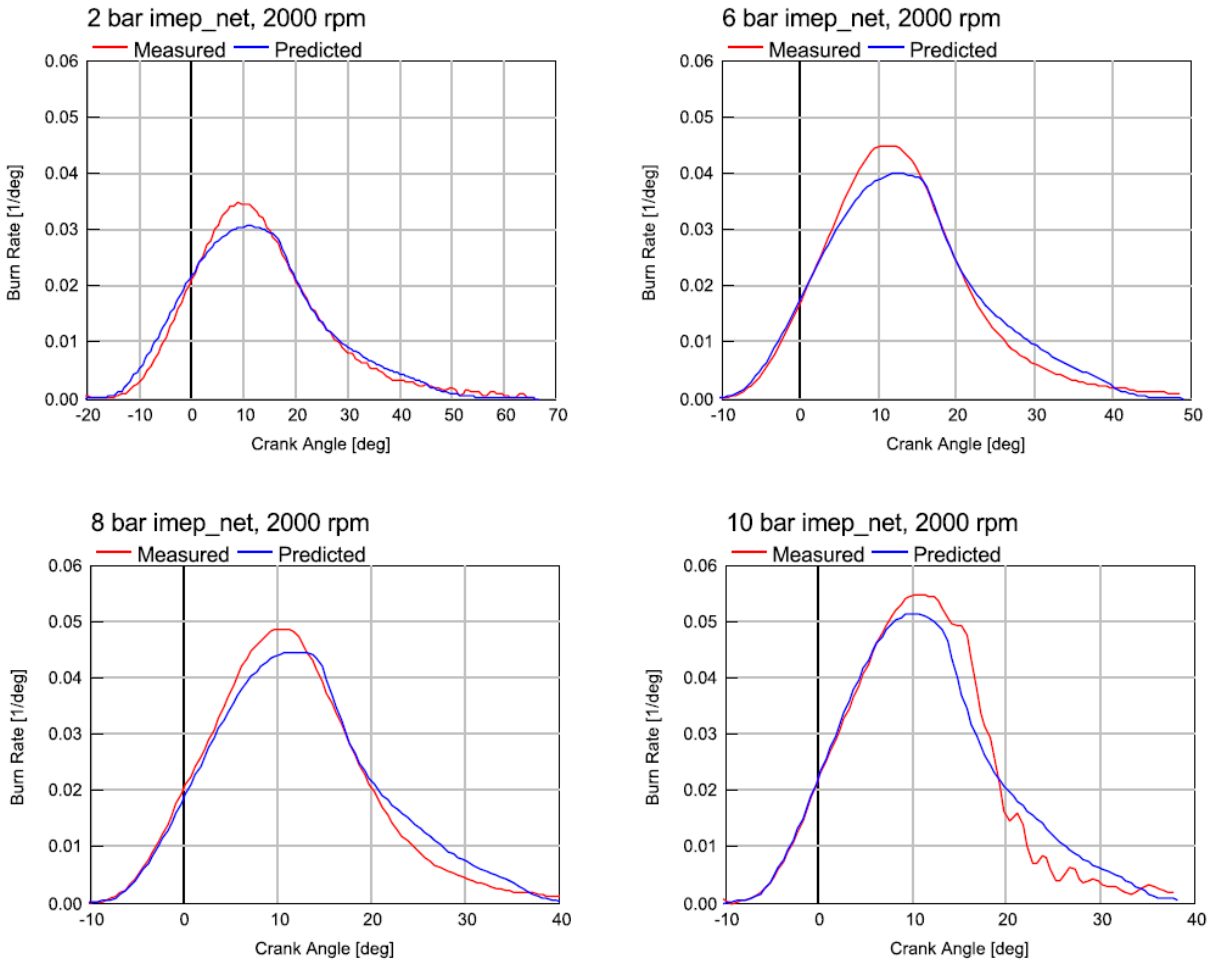


Figure B-2: Calibrated SITurb for 4 swept loads of gasoline engine: Burn rate